WAKE INDUCED
UNSTEADY BLADE FORCES
IN TURBO-MACHINES

MALCOLM D. LEFCORT

November 1962

WAKE INDUCED UNSTEADY BLADE FORCES

IN TURBO-MACHINES

by

Malcolm D. Lefcort

Under the Sponsorship of:

General Electric Company
Allison Division of General Motors Corporation
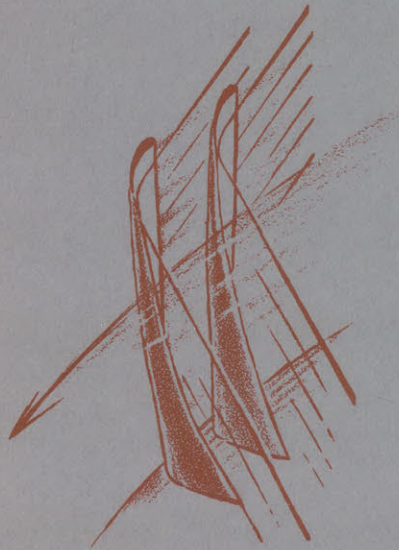
Gas Turbine Laboratory
Report Number 70

November 1962

Massachusetts Institute of Technology
Cambridge, Mass.

ABSTRACT

The wake interaction problem in a turbo-machine has been simulated in a water table. The pressure distribution over a compressor blade during the passage of a wake shed by an upstream wake generator has been determined experimentally using specially developed piezo-electric pressure transducers. The results indicate that the theory developed by R. X. Meyer for wakes that are very thin with respect to the blade chord is generally valid. The theory has been extended to cover the case of wakes of finite thickness. The peak unsteady force amounted to at least 23% of the steady lift force assuming a steady lift coefficient of 1.

ACKNOWLEDGEMENTS

WAKE INDUCED UNSTEADY BLADE FORCES

IN TURBO-MACHINES

by

Malcolm D. Lefcort

INDEX

1. INTRODUCTION

The fact that turbomachine blades are subjected to unsteady forces aris-
ing from the relative motion of adjacent blade rows has been known for some
time. Although the frequency of these forces is readily determined, the mag-
nitude is not. Thus, the engineer who is interested in predicting vibratory
stresses to prevent fatigue failures is forced to resort to some form of em-
pirical factor to take the unsteady force into account.

Actually, unsteady forces in turbo-machines are due to four main effects.
In this report they will be called the circulation effect, the blade thickness
effect, the wake effect and the wake distortion effect.

The circulation effect and the blade thickness effect are potential flow
effects. The wake effect and the wake distortion effect are rotational flow
effects. Although the wake distortion effect is really part of the wake ef-
fect it is considered as a separate effect to facilitate the mathematical
treatment.

The circulation effect arises because of the presence of circulation
about the blades of the moving adjacent blade rows. This effect can be vis-
ualized in the following manner. Consider the moving adjacent blades re-
placed by point potential vortices. These moving vortices induce fluctuating
velocities normal to the blade in question which give rise to unsteady forces.

The blade thickness effect arises because of the presence of potential
flow fields (other than circulation) about the blades of the adjacent blade
rows due to the finite thickness of the blades. (The boundary layer dis-
placement thickness may be included in the blade thickness.) These moving
flow fields induce fluctuating velocities normal to the blade in question
and hence result in unsteady blade forces.

If the adjacent blade had zero thickness the blade thickness effect
would be zero. Similarly, if there was no circulation about the adjacent

blades the circulation effect would be zero.

The wake effect refers to unsteady velocity fields induced at the blade in question by the wakes shed by upstream blades which are swept downstream with the free stream velocity. If the boundary layer were somehow removed from the upstream blades the wake effect would be zero. Once the wakes shed by the upstream blades reach the blade in question, the fourth effect, the wake distortion effect, arises. The lines of constant vorticity forming the wake are distorted in passing over the blade. This effect can be visualized by considering the wake as a moving jet approaching the blade. On reaching the leading edge the jet is cut in two and the two halves are distorted; one half of the jet contracts and the other spreads out on the blade surface.

The unsteady flow problem occurring in turbo-machines is extremely complicated. It must be attacked piecemeal and then only after making several broad assumptions. The usual assumptions are incompressible flow and two-dimensional lightly loaded airfoils. As a result, the solutions are more applicable to compressor rather than turbine blades.

Kemp and Sears have dealt with the circulation effect in Ref.(1) for the case of a stator-rotor combination. The same authors treated the wake effect for a stator-rotor combination in Ref.(2). In both cases they obtained over-all unsteady lifting forces and moments.

Meyer considered the wake effect for the case of an isolated airfoil in Ref. (3) in which he calculated the unsteady pressure gradient and velocity distributions over the airfoil. He also considered the wake distortion effect.

This report deals with the wake effect and draws freely upon the work of Meyer. It is, essentially, an experimental verification of the theory developed by Meyer (called in the body of this report "thin airfoil theory") for the pressure distribution over a lightly loaded single airfoil during the passage of a thin wake in a two-dimensional incompressible flow. The

thin airfoil theory is also extended to cover the case of a wake of finite thickness whose thickness is still small compared to the blade chord. The unsteady pressures were obtained using piezo-electric pressure transducers constructed according to techniques developed by Ruetenik, Ref. (4).

2. THE WAKE EFFECT

2.1 INTRODUCTION

Fig. 1 illustrates the flow pattern prevailing in a typical compressor. A rotor blade row is shown moving past a stationary blade row. The boundary layers formed on the rotor blades, by the action of viscosity, give rise to a region of retarded flow which, upon leaving the blade, forms the wake. The wake is swept downstream over the blade of the following blade row.

The wakes appear as regions of velocity defect with respect to the blades that shed them; however, to the blades of the adjacent downstream blade row they appear as jets. This phenomena becomes clear by referring to Fig. 2.

The narrow band of fluid flowing at right angles to the flat plate can be imagined as a wake shed by an upstream moving blade. In this idealized picture the moving blade is imagined to have moved sufficiently far from the stationary blade (the flat plate) so as to have passed on beyond the top of Fig. 2.

To an observer sitting on the pressure side of a compressor blade the wake appears as an oncoming jet in an otherwise uniform field of free stream velocity V. In the case of a turbine blade the wake appears as a jet when viewed from the suction side of the blade.

In general the wake is inclined to the blade and the velocity defect has components both perpendicular and parallel to the main stream. The parallel components are normally neglected since they are usually much smaller than the free stream velocity.

The effect of the wake is momentarily to change the angle of attack of the flow with respect to the blade and thereby momentarily to change the lift

acting on the blade: hence the unsteady blade force.*

The pressure and velocity distribution changes are calculated in Ref. (3) for the case of a narrow wake passing over a flat plate. The model Meyer used is shown in Fig. 2. It is instructive to review briefly the general unsteady pressure theory developed by Meyer. This is done in Appendix 1 and the results are quoted in the next Section.

2.2 THIN AIRFOIL THEORY

Briefly, Meyer considered the problem of a flat plate moving in an infinitely long sinusoidal gust, the amplitude of the gust being small compared with the free stream velocity, and determined the pressure and velocity perturbations over the flat plate using linearized theory. He deduced a result previously derived by Küssner, Ref. (5), by the solution of an integral equation. Meyer based his solution on results obtained by Von Karman and Sears in Ref. (6).

Meyer shows that the pressure gradient for the case of a single wake of infinitesimal width is given by

$$\frac{\partial p}{\partial x} = \pm \frac{2\rho V \overline{W}}{c} \frac{T(t')}{(1+x')(1-x'^2)^{1/2}} \tag{1}$$

where the upper and lower signs refer to the suction and pressure side respectively (Fig. 2), x' and t' represent the dimensionless distance and time respectively, $\overline{W}$ is the integrated wake velocity defect per blade chord and is defined by

$$\overline{W} = \frac{1}{c} \int_{-\infty}^{\infty} W(\xi) \, d\xi \tag{2}$$

and $T(t')$ is defined according to

$$T(t') = \frac{1}{\pi} \int_{-\infty}^{\infty} S(\omega) e^{i\omega t'} \, d\omega \tag{3}$$

where $S(\omega)$ is the Sears function and is tabulated in Ref. (7). $T(t')$ is tabulated in Ref. (8).

-----

* The wake effect is not unique in this respect; in fact, both the circulation effect and the blade thickness effect cause the angle of attack to change.

It can be shown that

$$k_2(t') = \int_{-1}^{t'} T(t') \, dt'$$ (4)

where k_2 is a function used by Küssner in Ref. (9).

Following usual practice in airfoil theory and setting $x' = \cos\Theta$

$$\frac{\partial p}{\partial x} = \pm \frac{2\rho V \overline{W}}{c} \frac{T(t)}{(1+\cos\Theta)\sin\Theta}$$

which, upon integration, gives

$$p(\Theta,t) = \mp \rho V \overline{W} \, T(t) \, \tan\frac{\Theta}{2}$$ (5)

Equation (5) is quite revealing. It shows that the pressure distribution is similar to that over a flat plate set at an angle of attack in a steady uniform flow regardless of the wake velocity defect. The "equivalent angle of attack" (a concept introduced by Yeh and Eisenhuth in Ref. (10)) decreases monotonically with time.

Furthermore, for the compressor blade of Fig. 2, the pressure decreases on the suction side and increases on the pressure side due to the wake effect. The reverse is true for a turbine blade since the wake approaches the latter from the suction side. Thus the unsteady force tends to increase the load on a compressor blade but decrease the load on a turbine blade.

The similarity of pressure distribution means that the lift force remains centered at the forward neutral point (1/4 chord) at all times as first proved by Von Karman and Sears in Ref. (6).

Yeh and Eisenhuth formulated the pressure distribution in Ref. (10) for a thin airfoil in an infinitely long sinusoidal gust in a similar fashion to equation (5).

i.e.

$$p(\Theta,t') = \rho V v_o e^{i\omega t'} S(\omega) \, \tan\frac{\Theta}{2}$$ (6)

where v_o is the maximum amplitude of the gust.

The unsteady lift force acting on the blade due to the passage of the wake can be obtained by integrating equation (5) over the blade.

Since

$$L = -\int_{-\frac{c}{2}}^{\frac{c}{2}} (p_U - p_L) \, dx$$ (7)

where U and L refer to the upper (suction) and lower (pressure) sides of the blade respectively.

$$\therefore \quad L = - c\rho V\overline{W}\, T(t') \int_{\pi}^{0} \tan\frac{\theta}{2} \sin\theta \, d\theta$$

i.e.

$$L = \pi c \rho V \overline{W}\, T(t') \tag{8}$$

Thus the unsteady lift force is a maximum the instant the center of the wake reaches the leading edge (t' = -1) and decreases monotonically thereafter.

Sears in Ref. (11) derived the equivalent expression for the lift force on an airfoil in an infinitely large sinusoidal gust and this was put in the form of equation (8) by Kemp in Ref. (12). Sears showed that

$$L = \pi c \rho V v_0 \, e^{i\omega t'} S(\omega) \tag{9}$$

Equation (9) bears the same relation to (8) as (6) does to (5). As the definition of the T function shows, (3), it represents the effects of all waves of all wave numbers.

A lift coefficient can be obtained from (9). Thus

$$C_L = \frac{L}{\frac{1}{2}\rho V^2 c} = \frac{2\pi \overline{W}\, T(t')}{V} \tag{10}$$

2.3 EXTENSION TO WIDER WAKES

The theory presented in Section 2.2 is valid for "thin" wakes. As a criteria $\lambda = \dfrac{2b}{c\sin\beta}$, where 2b is the total wake half-width, must be small i.e. $\lambda \to 0$.

Because of the linearity of the problem equation (5) can be extended to cover wakes for which λ is small, but does not approach zero. To do this the wake is considered to comprise many "thin" wakes and the effects of each are added, by the principle of superposition. The effect of each "thin" wake is considered to act from the instant its centerline crosses the blade's leading edge; i.e. the effect of each "thin" wake is reckoned according to its own t', the non-dimensional time being t' = -1 when its centerline reaches the leading edge. The individual (t')s are related to t'_0, where t'_0 is rec-

koned from the instant the centerline of the entire wake crosses the leading edge.

Thus, consider the configuration in the following sketch:
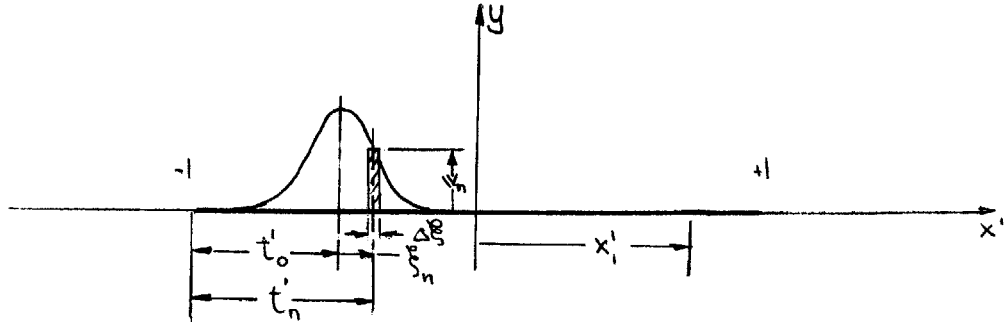
The wake is considered to be made up of a finite number of thin wakes each of integrated velocity defect $W_n = w_n \Delta \xi$. The total pressure perturbation on the suction side of the blade at $x' = x'_1$ is given by

$$P_{\substack{1 \\ x=x'_1}}(t') = -\rho V \left[\tan \frac{\Theta}{2} \right]_{x=x'_1} \sum_{-N}^{N} \overline{W}_n T(t'_n) \tag{11}$$

if the wake is divided into $2N$ thin wakes and $n = 0$ for the thin wake on the centerline of the whole wake.

The thin wake at ξ_n reaches the blade $\frac{\xi_n}{V}$ seconds before the centerline of the entire wake, i.e.

$$t'_n = t'_o + \frac{2V}{c} \frac{\xi_n}{V} = t'_o + \xi'_n$$

where

$$\xi'_n = n \cdot \frac{2 \Delta \xi}{c}$$

hence

$$P_{\substack{1 \\ x=x'_1}}(t'_o) = -\rho V \left[\tan \frac{\Theta}{2} \right]_{x=x'_1} \sum_{-N}^{N} \overline{W}_n T \left(t'_o + n \cdot \frac{2\Delta\xi}{c} \right) \tag{12}$$

but

$$\overline{W}_n = \frac{1}{c} w_n \Delta \xi$$

and in the limit as $N \to \infty$ (as $\Delta \xi \to d\xi$)

$$P_{\substack{1 \\ x=x'_1}}(t'_o) = -\rho \frac{V}{c} \left[\tan \frac{\Theta}{2} \right]_{x=x'_1} \int_{-\infty}^{\infty} w(\xi) T(t'_o + \xi') d\xi \tag{13}$$

defining

$$\Lambda(t'_o) = \int_{-\infty}^{\infty} w(\xi) T(t'_o + \xi') \, d\xi \tag{14}$$

this may be written

$$P(x'_1, t'_o) = \mp \rho \frac{V \Lambda(t'_o)}{c} \tan \frac{\Theta}{2} \tag{15}$$

In calculating $\Lambda(t_o')$ it is useful to put it in the form

$$\Lambda(t_o') = \frac{c}{2}\int_{-\infty}^{\infty} w(\xi')\, T(t_o'+\xi')\, d\xi' \qquad (16)$$

At a given t_o' , each function depends only on ξ '. Because T is tabulated as a function of t' and $d\xi' = dt'$, the origin of ξ ' being only displaced from the origin of t' , the integral of equation (16) can be examined for convergence purposes in the following form, assuming t_o' finite,

$$\int_{-\infty}^{\infty} w(t')\, T(t')\, dt'$$

This represents the integration of two functions, one of which goes to infinity, i.e. $T(t') = \infty$ at $t' = -1$. However, because of the relation of Meyer's $T(t')$ to Küssner's $k_2(t')$, equation (4),

i.e.

$$k_2(t') = \int_{-1}^{t'} T(t')\, dt'$$

and because $k_2(t') = 0$ for $t' \leqslant -1$ and is finite for $t' > -1$ the above integral exists. In fact, by integration by parts, it can be put in the form

$$w(t')\, k_2(t')\Big]_{-\infty}^{\infty} - \int_{-\infty}^{\infty} k_2(t')\, \frac{dw(t')}{dt'}\, dt'$$

Hence, equation (16) can be rewritten in the form

$$\Lambda(t_o') = \frac{c}{2}\left\{\left[w(\xi')\, k_2(t_o'+\xi')\right]_{-\infty}^{\infty} - \int_{\infty}^{\infty} k_2(t_o'+\xi')\, \frac{dw(\xi')}{d\xi'}\, d\xi'\right\} \qquad (17)$$

Although the limits in equation (16) are $\pm\infty$, the actual integration is only carried out over the thickness of the wake and then it can be terminated before the end of the wake (upstream side) if $t_o' + \xi$ ' < -1 since $T(t')$ = 0 for $t' < -1$. This can better be understood by referring to the following sketch.
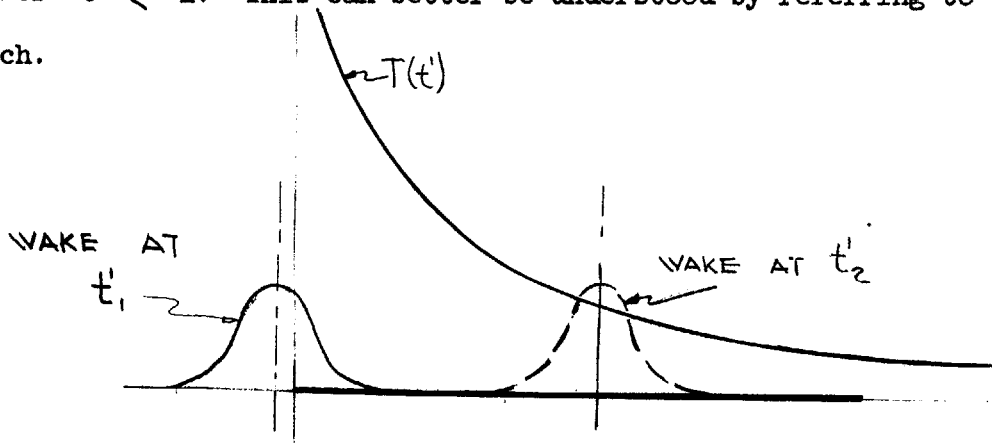
The same limits apply to equation (17). In fact, the non-integral term vanishes because, while the wake is still coming on to the blade k_i is zero and, at the upper limit, w is zero. When all the wake is on the blade, the lower limit is zero since w is zero.

$$\therefore \; \Lambda(t_o') = -\frac{c}{2} \int_{-\infty}^{\infty} k_2(t_o' + \xi') \; \frac{dw(\xi')}{d\xi'} \; d\xi' \tag{17a}$$

Equations (16) and (17) must be integrated numerically. To do this, tables of $T(t')$ and $k_2(t')$ in the vicinity of $t' = -1$ were drawn up and are included in Appendix 2 along with Meyer's and Küssner's complete tables for $T(t')$ and $k_2(t')$ respectively.

To calculate k_2, the series given in equation (42) of Ref. (9) was used, it being noted that Küssner's "s" corresponds to t'. Values of $T(t')$ were calculated by numerical differentiation using central differences as far as the fifth difference, Ref. (13).

3. WAKE DISTORTION EFFECT

The theory of Section 2 is derived from linearized equations of motion with the additional "thin" wake assumption. This amounts to assuming the lines of constant vorticity, which form the wake, are transported with the undisturbed free stream velocity V. However, when the wake is on the blade this cannot be true; in fact, the lines of constant vorticity are splayed outwards from the wake centerline along the pressure side of a compressor blade (suction side on a turbine blade) and nipped inwards along the suction side (pressure side). This phenomena is illustrated in Fig. 3 which shows the distorted wake on the blade at a particular instant of time during the wake's passage over the blade.

Meyer showed that the distortion of the lines of vorticity is of the same order of magnitude as the width of the wake and hence this effect, the wake distortion effect, cannot be neglected. A parameter which can be used to

describe the distortion is the relative distortion parameter D where D

is proportional to the ratio of the wake distortion* to the wake width and

is defined by

$$D = \left(\frac{c}{2b}\right)^2 \frac{\overline{W}}{V} \qquad (18)$$

Meyer estimated the effect of the wake distortion by considering the

wake as a two-dimensional jet suddenly cut by an infinite flat plate and

calculated the pressure change on either side of the plate. The model can

be regarded as a jet passing through a narrow slit in an infinite plate

with the slit being suddenly closed.

The case Meyer calculated was for λ = -.15, β = 90° and D = 1.08.

The result for the suction side of a compressor blade is shown in Fig. 4

for $\frac{\rho V W}{c}$ = .217" H_2O. This value and the time scale were chosen because of

the relation to the experimental part of this report.

Thus the pressure is seen to rise on the suction side of the blade

above the value it would have from the theory of Section 2.2.

A qualitative explanation of this phenomena is as follows. If the wake

is assumed to be flat of width b_0 (see Fig. 22), and of average velocity

defect $W_{avg} = \frac{1}{b} \int_{-\infty}^{\infty} W(\zeta)\, d\zeta$ then it can be replaced by two parallel in-

finitely long vortex sheets each of vorticity $\gamma = W_{avg}$. Furthermore, if

the flow in the vicinity of the jet can be assumed to be steady, i.e. if the

distorted jet boundaries are assumed to be fixed in a form which can be con-

sidered as a mean of the boundaries at the leading and trailing edges, then

the velocities induced at the blade surface dan be determined, as shown be-

low, using the method of images. The average pressure in the vicinity of

the wake on the suction and pressure surfaces can then be found by integ-

ration assuming no loss in total pressure from the stagnation points on both

sides of the blade.

- - - - - - - - - -

* A measure of the wake distortion is the amount of contraction experienced
by the jet on the suction side of the blade as shown in Fig. 3.

(a)

(b)

Suction Side

(c)
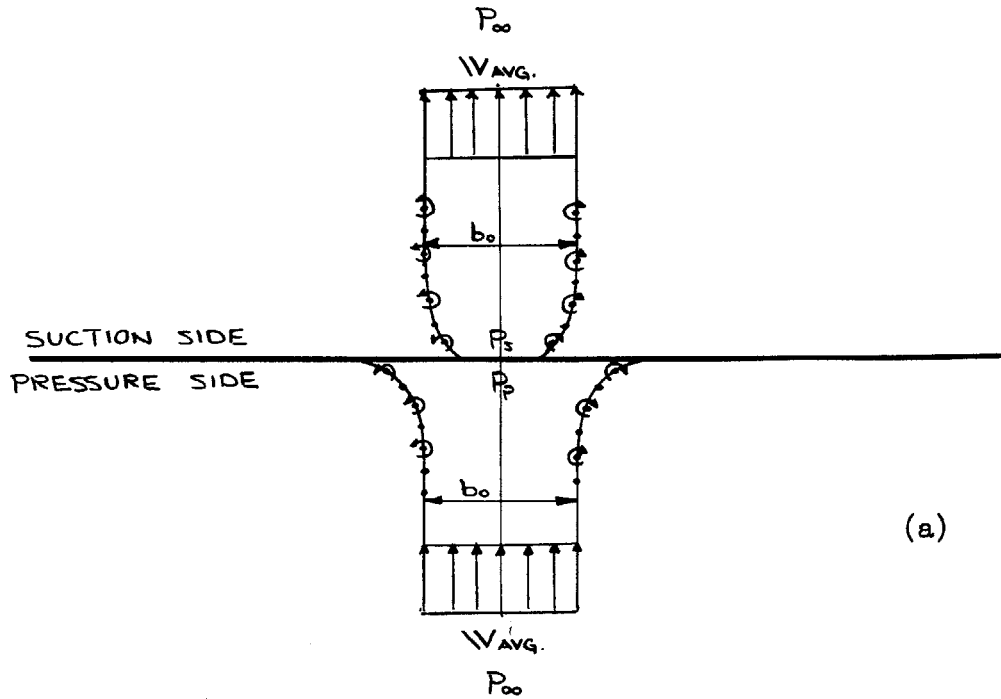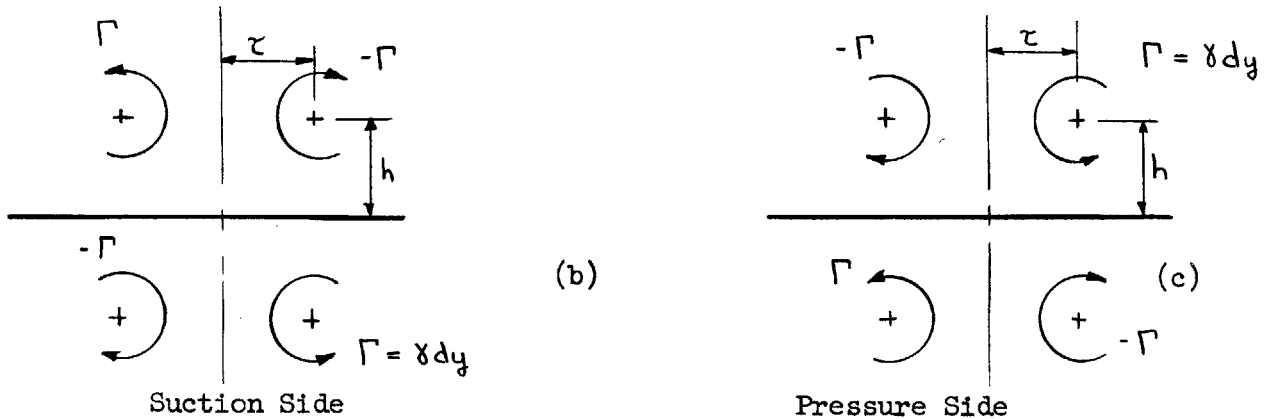
Pressure Side

The sketch at (a) shows the model. The sketches at (b) and (c) show the "equivalent" potential flow fields to be analyzed. From basic potential flow theory

$$\varphi_{\substack{\text{SUC}^N \\ \text{SIDE}}} = \frac{\Gamma}{2\pi}\left\{\text{Tan}^{-1}\left(\frac{y+h}{x-\tau}\right) + \text{Tan}^{-1}\left(\frac{y-h}{x+\tau}\right) - \text{Tan}^{-1}\left(\frac{y-h}{x-\tau}\right) - \tan^{-1}\left(\frac{y+h}{x+\tau}\right)\right\}$$

$$\varphi_{\substack{\text{PRESS} \\ \text{SIDE}}} = \frac{\Gamma}{2\pi}\left\{\text{Tan}^{-1}\left(\frac{y-h}{x-\tau}\right) + \text{Tan}^{-1}\left(\frac{y+h}{x+\tau}\right) - \text{Tan}^{-1}\left(\frac{y-h}{x+\tau}\right) - \text{Tan}^{-1}\left(\frac{y+h}{x-\tau}\right)\right\} = -\varphi_S$$

It follows that

$$\varphi_S = \frac{\Gamma}{2\pi}\tan^{-1}\left[\frac{4h\tau\left\{(x^2-\tau^2)-(y^2-h^2)\right\}}{\left\{(x^2-\tau^2)-(y^2-h^2)\right\}^2 + 4(x^2y^2-\tau^2h^2)}\right] = -\varphi_P$$

and

$$U_P = \frac{\partial \varphi_P}{\partial x} = \frac{4\Gamma}{\pi}\frac{h\tau x\left[\left\{(x^2-\tau^2)-(y^2-h^2)\right\}^2 - 4(y^2-h^2)(y^2+\tau^2)\right]}{\left[\left\{(x^2-\tau^2)-(y^2-h^2)\right\}^2 + 4(x^2y^2-h^2\tau^2)\right]^2 + 16h^2\tau^2\left[(x^2-\tau^2)-(y^2-h^2)\right]^2} = -U_S$$

on the blade surface where $y = 0$

$$U_p = \frac{4}{\pi} \Gamma \frac{h\tau x}{[(x^2 - \tau^2 + h^2)^2 + 4h^2\tau^2]} = -U_s$$

replacing Γ by $\gamma \, dy$ and integrating

$$U_p(x)\Big]_{y=0} = \frac{4 W_{AVG}}{\pi} x \int_0^\infty \frac{\tau(y) \, y \, dy}{[(x^2 - \tau^2 + h^2)^2 + 4\tau^2 y^2]} = -U_s(x)\Big]_{y=0}$$

The integral was evaluated for the experimental set up using a parabolically shaped lower jet boundary of total distorted width $3b_0$ at the blade surface. It was found to be independent of x over the width b_0. Hence $u_p(x)_{y=0} = k_p W_{avg}x$, where k_p is a constant, so that the average pressures are given by

$$P_{PS} = \frac{1}{b_0} \int_{-b_0/2}^{b_0/2} \left[P_\infty + \frac{1}{2} \rho W_{AVG}^2 - k_{PS} \cdot \frac{1}{2} \rho W_{AVG}^2 \, x^2 \right] dx$$

$$= P_\infty + \frac{1}{2} \rho W_{AVG}^2 \left[1 - k_{PS}^2 \cdot \frac{1}{3} \left(\frac{b_0}{2} \right)^2 \right]$$

On the suction side, it is easy to show that the bracket is very close to unity and hence the average pressure $p_s > p_\infty$. The difference in pressure is

$$P_s - P_\infty = \frac{1}{2} \rho W_{AVG}^2 = \frac{1}{2} \rho V^2 \left(\frac{W_{AVG}}{V} \right)^2$$

of the same order of magnitude as measured in the experimental part of this report.

On the pressure side, because the wake is spread out, it is very plausible that the terms in parenthesis could be negative, in which case $p_p < p_\infty$. This in fact was found to be true experimentally but using the experimental value for b_0, this could not be shown conclusively.

Thus the effect of wake distortion is to decrease the unsteady force on a compressor blade. For a turbine blade it acts in the reverse manner. However, as the turbine blade unsteady force opposes the steady turbine lifting force, the wake distortion effect has the effect of cancelling some of the opposing unsteady force.

opposing unsteady force.

The distortion of the wake also has an effect on the location of the neutral point. While the wake is upstream of $x' = -.5$, the neutral point is downstream of $x' = -.5$. The neutral point is shifted upstream of $x' = -.5$ when the wake has passed the point $x' = -.5$.

4. BLADE THICKNESS EFFECT

4.1 INTRODUCTION

This section deals with the effect of velocities induced at the blade in question by the potential flow about an upstream blade. The effect of the circulation about upstream blades is distinct from the thickness effect, as mentioned in Section 1, and is discussed fully in Ref. (1).

This effect is not expected to be very large; once the wake reaches the blade, it is expected to be imperceptible. Hence several simplifying assumptions are made subject to later verification.

The blade in question is regarded as semi-infinite, and the upstream blade is represented by two well-known potential bodies: namely a source in a free stream and a doublet in a free stream. The former represents a solid body with some resemblance to a blade and its wake while the latter represents a cylinder. Regarding the blade as semi-infinite means that attention must be restricted to the front part of the blade.

The flow is regarded as being unsteady and yet is treated as quasi-steady, i.e. the source and doublet are considered as moving, with respect to the semi-infinite blade, along some prescribed path but at each instant their effects are calculated as though they had always occupied their instantaneous position. This approach is justified since the flow is incompressible and is consistent with the linearized approach used throughout.

The linearized unsteady equation of motion for small perturbations is

$$\frac{p}{\rho} = -\left(\frac{\partial \varphi}{\partial t} + Uu \right)$$
(19)

as shown in texts on aerodynamics (see, for example, Ref. (14)).

where φ is the free stream velocity potential

U is the free stream velocity

u is the perturbation in the free stream velocity

and $\dfrac{\partial \varphi}{\partial t}$ at the blade is determined by calculating the change in

φ at a given position on the blade between one instantaneous flow pattern and the next.

Now $u = \dfrac{\partial \varphi}{\partial x}$
(20)

and using the well-known result (Ref. (14)) u is also given by

$$u = \pm \frac{\gamma}{2}$$
(21)

where γ is the vorticity distribution replacing the blade.

γ is calculated from the Söhngen inversion formula, Ref. (14), which yields the vorticity distribution required to cancel the perpendicular velocities at the blade surface; for a semi-infinite blade γ is given by (see Appendix 3)

$$\gamma(x) = \frac{2}{\pi} \frac{1}{x^{\frac{1}{2}}} \oint_0^\infty \frac{\xi^{\frac{1}{2}} v(\xi)\, d\xi}{(x-\xi)}$$
(22)

where the integration sign denotes the Cauchy principal value of the integral, and $v(\xi)$ is the negative of the perpendicular velocity induced at the blade by the adjacent blades.

Hence, from (20), (21) and (22)

$$\frac{\partial \varphi}{\partial x} = \pm \frac{1}{\pi} \frac{1}{x^{\frac{1}{2}}} \oint_0^\infty \frac{\xi^{\frac{1}{2}} v(\xi)}{(x-\xi)}\, d\xi$$
(23)

where the upper and lower signs refer to the upper (suction side for compressor blade) and lower (pressure side for compressor blade) sides respectively. Integration of (23) yields φ which is then differentiated to give $\dfrac{\partial \varphi}{\partial t}$. $\dfrac{\partial \varphi}{\partial t}$ and $u = \dfrac{\partial \varphi}{\partial x}$ are substituted in (19) to yield the pressure on the blade.

4.2 SOURCE SOLUTION

Consider the configuration of Fig. 5. The source at x_0, y_0, moves along some prescribed path with velocity V in a flow of velocity U parallel to the semi-infinite flat plate. The origin is fixed at the blade leading edge.

Now, from standard formulae,

$$\varphi_{\text{source}} = \frac{Q}{2\pi} \ln \left\{ (x-x_0)^2 + (y-y_0)^2 \right\}^{\frac{1}{2}} \tag{24}$$

where Q is the strength of the source.

$$\therefore \; v = \frac{\partial \varphi}{\partial y} = \frac{Q}{2\pi} \frac{y-y_0}{(x-x_0)^2 + (y-y_0)^2}$$

Hence, at the blade where $y = 0$,

$$v = -\frac{Q}{2\pi} \frac{y_0}{(x-x_0)^2 + y_0^2} \tag{25}$$

$$\therefore \; v(\xi) = \frac{Q}{2\pi} \frac{y_0}{(\xi-x_0)^2 + y_0^2} \tag{26}$$

Substituting (26) in (23)

$$\frac{\partial \varphi}{\partial x} = \pm \frac{Q}{2\pi^2} \frac{y_0}{x^{\frac{1}{2}}} \oint_0^\infty \frac{\xi^{\frac{1}{2}} \, d\xi}{(\xi^2 + b\xi + c)(x-\xi)} \tag{27}$$

where $\qquad b = -2x_0$

$$c = x_0^2 + y_0^2 \tag{27a}$$

The simplest method of solution is via the Calculus of Residues (see e. g. Ref. (15)). The integral in (27) will be solved by contour integration in the ζ plane where $\qquad \zeta = \xi + i\eta$

$$\therefore \; I = \oint_0^\infty \frac{\zeta^{\frac{1}{2}}}{(\zeta^2 + b\zeta + c)(x-\zeta)} \, d\zeta \tag{28}$$

and I is to be evaluated along the following contour, (see next page) where, because of the presence of $\zeta^{\frac{1}{2}}$ a branch point exists at the origin, in addition to the singularity at $\xi = x$. Therefore a cut is made along the real axis from $\xi = 0$ to $\xi = \infty$ to keep ζ single-valued and hence analytic

ζ PLANE
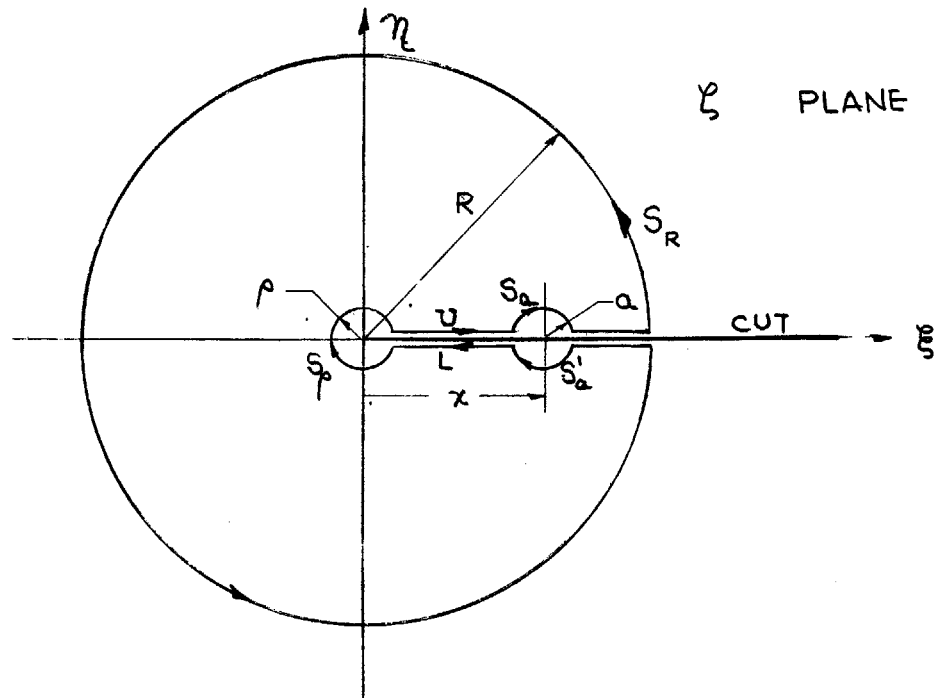
within the contour.

$$\therefore I = \lim \left\{ \int_{\rho}^{x-a} U + \int_{S_a} U + \int_{x+a}^{R} U + \int_{S_R} + \int_{R}^{x+a} L + \int_{S_a'} L + \int_{x-a}^{\rho} L + \int_{S_\rho} \right\} \frac{\zeta^{\frac{1}{2}} d\zeta}{(\zeta^2 + b\zeta + c)(x-\zeta)} = 2\pi i \sum \text{Residues} \tag{29}$$

$$R \longrightarrow \infty$$

$$a \longrightarrow o$$

$$\rho \longrightarrow o$$

Evaluating each integral separately:

$$\int_{S_R} f(\zeta) d\zeta = \int_0^{2\pi} \frac{iR^{\frac{3}{2}} e^{\frac{3i\theta}{2}} d\theta}{(R^2 e^{2i\theta} + bRe^{i\theta} + c)(x - Re^{i\theta})}$$

Hence as $R \longrightarrow \infty$ $\int_{S_R} f(\zeta) d\zeta$ behaves as $\dfrac{R^{\frac{3}{2}}}{R^3}$ which approaches zero.

$$\int_{S_\rho} f(\zeta) d\zeta = \int_0^{2\pi} \frac{i\rho^{\frac{3}{2}} e^{\frac{3i\theta}{2}} d\theta}{(\rho^2 e^{2i\theta} + b\rho e^{i\theta} + c)(x - \rho e^{i\theta})}$$

hence as $\rho \to 0$, $\int_{S_\rho} f(\zeta) d\zeta$ behaves as $\dfrac{\rho^{\frac{3}{2}}}{\text{constant}}$ which approaches zero.
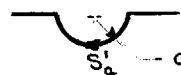
On S_a $\qquad \zeta = x + ae^{i\theta}$

$$\therefore \int_{S_a} f(\zeta) d\zeta = \int_\pi^0 \frac{(x + ae^{i\theta})^{\frac{1}{2}} iae^{i\theta} d\theta}{\left\{(x + ae^{i\theta})^2 + b(x + ae^{i\theta}) + c\right\}(x - x - ae^{i\theta})}$$

$$= -i \int_\pi^0 \frac{(x + ae^{i\theta})^{\frac{1}{2}} d\theta}{(x + ae^{i\theta})^2 + b(x + ae^{i\theta}) + c}$$

and as $a \to 0$

$$\int_{S_a} f(\zeta) \, d\zeta = -i \int_{\pi}^{0} \frac{x^{\frac{1}{2}}}{x^2 + bx + c} \, d\theta = \frac{i\pi x^{\frac{1}{2}}}{x^2 + bx + c}$$

On S_a'

$$\zeta = x e^{i2\pi} + a e^{i\theta}$$

$$\therefore \int_{S_a'} f(\zeta) \, d\zeta = -i \int_{2\pi}^{\pi} \frac{x^{\frac{1}{2}} e^{i\pi}}{x^2 + bx + c} \, d\theta = -\frac{i\pi x^{\frac{1}{2}}}{x^2 + bx + c}$$

$$\therefore \left\{ \int_{S_a} + \int_{S_a'} \right\} f(\zeta) \, d\zeta = 0$$

Collecting terms

$$\left\{ \oint_{0}^{\infty} U + \oint_{\infty}^{0} L \right\} f(\zeta) \, d\zeta = 2\pi i \sum \text{Residues}$$

Now, along the upper bank of the cut $\quad \zeta = \xi$

$$\therefore \oint_{U} f(\zeta) \, d\zeta = \int_{0}^{\infty} \frac{\xi^{\frac{1}{2}} \, d\xi}{(\xi^2 + b\xi + c)(x - \xi)}$$

And, along the lower bank

$$\zeta = \xi e^{i2\pi} = \xi$$
$$\therefore \quad \zeta^{\frac{1}{2}} = \xi^{\frac{1}{2}} e^{i\pi} = -\xi^{\frac{1}{2}}$$

$$\therefore \oint_{\infty}^{0} L f(\zeta) \, d\zeta = \int_{\infty}^{0} \frac{-\xi^{\frac{1}{2}} \, d\xi}{(\xi^2 + b\xi + c)(x - \xi)} = \int_{0}^{\infty} \frac{\xi^{\frac{1}{2}} \, d\xi}{(\xi^2 + b\xi + c)(x - \xi)}$$

$$\therefore \oint_{0}^{\infty} \frac{\xi^{\frac{1}{2}} \, d\xi}{(\xi^2 + b\xi + c)(x - \xi)} = \pi i \sum \text{Residues} \qquad (30)$$

Two simple poles arise at ζ_1 and ζ_2

$$\zeta_{1,2} = \frac{-b \pm \sqrt{b^2 - 4c}}{2}$$

$$\therefore \quad \zeta_1 = x_0 + i y_0 \quad ; \quad \zeta_2 = x_0 - i y_0$$

The residue at $\zeta = \zeta_1$ is found to be $\dfrac{\zeta_1^{\frac{1}{2}}}{(\zeta_1 - \zeta_2)(x - \zeta_1)}$ while that at $\zeta = \zeta_2$ is $\dfrac{-\zeta_2^{\frac{1}{2}}}{(\zeta_1 - \zeta_2)(x - \zeta_2)}$. Hence the sum of the residues is

$$\sum \text{Residues} = \frac{1}{(\zeta_1 - \zeta_2)} \left\{ \frac{\zeta_1^{\frac{1}{2}}}{(x - \zeta_1)} - \frac{\zeta_2^{\frac{1}{2}}}{(x - \zeta_2)} \right\}$$

Noting that

$$\zeta_1 = x_0 + i y_0 = r_0 e^{i\theta_0}$$
$$\zeta_2 = x_0 - i y_0 = r_0 e^{i(2\pi - \theta_0)}$$

and hence

$$\zeta_1^{\frac{1}{2}} = \gamma_0^{\frac{1}{2}} \left\{ \cos \frac{\theta_0}{2} + i \sin \frac{\theta_0}{2} \right\}$$

$$\zeta_2^{\frac{1}{2}} = \gamma_0^{\frac{1}{2}} \left\{ -\cos \frac{\theta_0}{2} + i \sin \frac{\theta_0}{2} \right\}$$

it is straight forward to evaluate the sum of the residues. Finally,

$$\int_0^\infty \frac{\xi^{\frac{1}{2}} d\xi}{(\xi^2 + b\xi + c)(x - \xi)} = \frac{\pi \gamma_0^{\frac{1}{2}}}{y_0} \left\{ \frac{(x - x_0)\cos \frac{\theta_0}{2} - y_0 \sin \frac{\theta_0}{2}}{(x - x_0)^2 + y_0^2} \right\} \tag{31}$$

Substituting (31) in (27).

$$u = \frac{\partial \varphi}{\partial x} = \pm \frac{Q}{2\pi} \frac{\gamma_0^{\frac{1}{2}}}{x^{\frac{1}{2}}} \left\{ \frac{(x - x_0)\cos \frac{\theta_0}{2} - y_0 \sin \frac{\theta_0}{2}}{(x - x_0)^2 + y_0^2} \right\} \tag{32}$$

Integration with respect to x and differentiation with respect to t followed by substitution in (19) yields the pressure. This will be done in Section 6. Selection of the source strength will also be discussed in Section 7.4.

4.3 DOUBLET SOLUTION

The configuration is the same as in Fig. 5. The source is replaced by a doublet whose axis is in the y direction.

Again, from standard formulae

$$\varphi_{\text{Doublet}} = - \frac{\mu(y - y_0)}{\left\{ (x - x_0)^2 + (y - y_0)^2 \right\}} \tag{33}$$

where μ is the strength of the doublet

$$\therefore v = \frac{\partial \varphi}{\partial y} = -\mu \frac{\left\{ (x - x_0)^2 - (y - y_0)^2 \right\}}{\left\{ (x - x_0)^2 + (y - y_0)^2 \right\}}$$

so that, on the blade, where y = 0

$$v = -\mu \frac{\left\{ (x - x_0)^2 - y_0^2 \right\}}{\left\{ (x - x_0)^2 + y_0^2 \right\}} \tag{34}$$

This can be rewritten in the following form

$$v = -\mu \left\{ \frac{1}{x^2 + bx + c} - \frac{2y_0^2}{(x^2 + bx + c)^2} \right\}$$

where b and c are defined in equation (27a)

$$\therefore v(\xi) = \mu \left\{ \frac{1}{\xi^2 + b\xi + c} - \frac{2y_0^2}{(\xi^2 + b\xi + c)^2} \right\} \tag{35}$$

Hence, substituting (35) in (23)

$$\frac{\partial \varphi}{\partial x} = \pm \frac{\mu}{\pi} \frac{1}{x^{\frac{1}{2}}} \left\{ \oint_0^\infty \frac{\xi^{\frac{1}{2}} d\xi}{(\xi^2 + b\xi + c)(x-\xi)} - 2y_0^2 \oint_0^\infty \frac{\xi^{\frac{1}{2}} d\xi}{(\xi^2 + b\xi + c)^2 (x-\xi)} \right\} \quad (36)$$

Now, the first integral has already been evaluated. Using the same contour for the second integral it can readily be shown that

$$\oint_0^\infty \frac{\xi^{\frac{1}{2}} d\xi}{(\xi^2 + b\xi + c)^2 (x-\xi)} = i\pi \sum \text{Residues} \quad (37)$$

Two double poles arise at

$$\ell_1 = x_0 + iy_0$$
$$\ell_2 = x_0 - iy_0$$

The sum of the residues is found to be

$$\sum \text{Residues} = \frac{1}{2} \frac{1}{(\ell_1 - \ell_2)^2} \left\{ \frac{1}{\ell_1^{\frac{1}{2}} (x - \ell_1)} + \frac{1}{\ell_2^{\frac{1}{2}} (x - \ell_2)} \right\}$$
$$- \frac{2}{(\ell_1 - \ell_2)^3} \left\{ \frac{\ell_1^{\frac{1}{2}}}{(x - \ell_1)} - \frac{\ell_2^{\frac{1}{2}}}{(x - \ell_2)} \right\}$$
$$+ \frac{1}{(\ell_1 - \ell_2)^2} \left\{ \frac{\ell_1^{\frac{1}{2}}}{(x - \ell_1)^2} + \frac{\ell_2^{\frac{1}{2}}}{(x - \ell_2)^2} \right\}$$

After a rather lengthy evaluation it can be shown that

$$\oint_0^\infty \frac{\xi^{\frac{1}{2}} d\xi}{(\xi^2 + b\xi + c)^2 (x-\xi)} = -\frac{\pi}{4y_0^2 r_0^{\frac{1}{2}}} \frac{\left\{ (x - x_0) \sin \frac{\theta_0}{2} - y_0 \cos \frac{\theta_0}{2} \right\}}{(x - x_0)^2 + y_0^2}$$
$$+ \frac{\pi r_0^{\frac{1}{2}}}{2 y_0^3} \frac{\left\{ (x - x_0) \cos \frac{\theta_0}{2} \right\}}{(x - x_0)^2 + y_0^2}$$
$$+ \frac{\pi r_0^{\frac{1}{2}}}{y_0} \frac{\left\{ (x - x_0) \cos \frac{\theta_0}{2} - y_0 \sin \frac{\theta_0}{2} \right\}}{\left\{ (x - x_0)^2 + y_0^2 \right\}^2} \quad (38)$$

This result could have been obtained directly from (31) for

$$\oint_0^\infty \frac{\xi^{\frac{1}{2}} d\xi}{(\xi^2 + b\xi + c)^2 (x-\xi)} = -\frac{d}{dc} \oint_0^\infty \frac{\xi^{\frac{1}{2}} d\xi}{(\xi^2 + b\xi + c)(x-\xi)}$$

To obtain the same form as (38) it is necessary to use the relation

$$r_0 \sin \frac{\theta_0}{2} = y_0 \cos \frac{\theta_0}{2} + x_0 \sin \frac{\theta_0}{2} \quad (39)$$

Finally, substituting (38) and (31) into (36)

$$u = \frac{\partial \varphi}{\partial x} = \pm \mu \left\{ \frac{1}{2 r_0^{\frac{1}{2}} x^{\frac{1}{2}}} \frac{\left\{ (x - x_0) \sin \frac{\theta_0}{2} - y_0 \cos \frac{\theta_0}{2} \right\}}{(x - x_0)^2 + y_0^2} - \right.$$

$$-\frac{\gamma_0^{\frac{1}{2}}}{\chi^{\frac{1}{2}}}\left\{\frac{\left[(\chi-\chi_0)^2-y_0^2\right]\sin\frac{\Theta_0}{2}+2(\chi-\chi_0)y_0\cos\frac{\Theta_0}{2}}{\left[(\chi-\chi_0)^2+y_0^2\right]^2}\right\}$$
18.

(40)

Equation (40) will be used in Section 6.

5. EXPERIMENTAL SET UP

5.1 THE APPARATUS

Basically, the apparatus consisted of an airfoil immersed in a two-dimensional water flow and a cylindrical wake generator which traversed the flow upstream of the airfoil. A schematic of the apparatus is shown in Fig. 6. Fig. 7 shows an overall view of the apparatus and Fig. 8 shows a detailed view of the test section.

The airfoil was a NACA 65 series uncambered blade on a 12" chord and with a 10% thickness ratio made out of aluminum. Its span was 5 1/2" and the aluminum surface was anodized. The airfoil was mounted in a Lucite test section, Fig. 9, and placed in the 24" tilting flume of the M.I.T. Hydrodynamic Laboratory on the flume centerline so that its plane of symmetry was parallel to the flume walls.

The top and bottom of the test section were made of 3/8" thick Lucite while the sides were 3/16" thick. Angle iron was used to brace the top both upstream and downstream of the airfoil.

Nine pressure transducers, described in Section 5.2 were positioned along the mid-span line of the blade at alternate 1" intervals: five on one side and four on the other. Those numbered 1, 3, 5, 7 and 9 were on the suction side of the blade and numbers 2, 4, 6 and 8 were on the pressure side. The stems of the transducers passed through the Lucite top and extended about 1" above the top. Electrical connectors were mounted on the end of the stems as described in Section 5.2.

A box of 3/16" Lucite sheet was placed around the stems on the top of the test section. The purpose of the box was to protect the connectors from splashing water during movement of the wake generator. The box can be seen

in Figs. 8 and 9.

The electrical signal from the pressure transducers was fed through an electrometer circuit and amplifiers to a Sanborn chart type recorder. The large black box housing two electrometer tubes can be seen mounted above the test section in Fig. 8 on an aluminum carriage which could slide along the rails of the flume.

The wake generator consisted of a hollow cylinder formed from 4 x 4 wire mesh (4 wires per inch by 4 wires per inch) .030" diameter mounted at the end of a 1/2" diameter stainless steel threaded rod. The end of the rod was borne on a Lucite carriage. The carriage rode on a 3/4" diameter stainless steel rod and was steadied by a 1" x 1/2" rectangular aluminum bar, both rod and bar being supported on a 1 1/8" thick timblend platform as shown in Fig. 8. Friction-free linear motion was attained by using a ball bushing.

Three narrow strips of wire screening of various mesh were placed one on top of the other at one point along the periphery of the hollow screen cylinder and ran the length of the cylinder. The strips decreased in width as they increased in mesh. The meshes used were 14 x 14 - .011"diameter, 20 x 20 - .016"diameter and 40 x 40 -.0085"diameter. Fig. 10 shows one of the wake generators.

Five screen cylinders were built using a 1 1/8" diameter 4 x 4 mesh hollow cylinder and one was made using a 1 3/4" diameter hollow cylinder. In addition, solid 1/2" diameter and 1" diameter cylinders were also used. The screen cylinders were used for reasons discussed below.

The wake generator was traversed obliquely across the flume at an angle of 60° to the flow. To minimize free surface effects it travelled in a box similar to the box holding the blade. A 1/2" wide slot was made in the top of the box to permit passage of the wake generator stem. The top was reinforced by vertical pieces of Lucite on either side of the slot and later by

6" channel iron as can be seen from Fig. 8. The top surface of the box was extended with respect to the bottom and a "nozzle" piece of Lucite was fitted to it so as to guide the flow gently during the transition from free surface to two-dimensional flow.

It was found necessary to damp out pressure waves associated with the starting of the wake generator as mentioned in Section 6. For this purpose screens were placed on the surface of the water immediately upstream of the blade. A three-sided 6" spacer was placed between the blade box and the slotted box. The top side was formed from a form of porous aluminum plate. Eight 40 x 40 mesh screens nestled in the cavity so formed.

The cylinder was driven by a 30 in. lb. constant torque Zero Max infinitely variable speed AC motor (Revco, Inc. - Minneapolis, Minn.) which drove a 1/8" ladder chain belt around two pulleys mounted at the ends of the platform as shown. The length of time the motor was operated was controlled by a General Electric electronic timer. The timer was triggered by a solenoid device which also triggered a marking needle on the Sanborn recorder used for pressure records.

A small DC tachometer generator was mounted on one of the pulleys. This enabled records of the cylinder velocity to be made on the Sanborn.

Eight 40 x 40 -.0085" diameter screens were placed in the nozzle box upstream of the flume adjustable nozzle. The screens were mounted on 3" wide 3/16" Lucite frames. The screens served to dampen turbulence in the flow and to smooth out the flow. Ref. (16) was used as a guide in selecting the screens.

Dye traces of the streamline pattern during the passage of the wake were obtained by injecting a solution of potassium permanganate. The dye was injected upstream of the blade box at the depth corresponding to the span centerline by means of a rake with eight hypodermic tubing needles. The header feeding the needles can be seen in Fig. 8 gripped by two small C clamps to

the upstream blade box angle iron. Hydroxylamine hydrochloride was found to be very effective in reducing the tendency of the water to turn brown due to the potassium permanganate. A pound of hydroxylamine hydrochloride restored about 30,000 gallons of tea colored water (due to 1/2 pound of potassium permanganate) to its initial colorless state. Of course, upon completion of the experiment the entire system was drained and flushed.

5.2 THE PRESSURE TRANSDUCER

The pressure transducers used in this study were built in the Gas Turbine laboratory and were a modified version of the type developed by Perkins (Ref. (17)) based on a design of Ruetenik, Ref. (4). The transducer operates on the piezo-electric principle, a charge being developed between the two faces of a pre-polarized ceramic disc upon the application of a change in pressure. The corresponding voltage difference is a measure of the pressure change. Because of the very high resistance across the ceramic an electrometer* must be used to convert the high impedance signal to an impedance level that can be handled by standard recording devices.

The transducer is shown in Fig. 11. The sensing element consists of a 0.300" diameter x 0.100" thick disc of US 500 ceramic produced by US Sonics Corporation of Cambridge. Both Ruetenik and Perkins used barium titanate. US 500 is one of a number of recently developed ceramics using lead zirconate titanate with suitable additives. In addition to being three times as sensitive as barium titanate it can also be used up to temperatures of 300°C

----

* An electrometer is basically a vacuum tube operated as a cathode follower and designed to draw extremely low grid currents (10^{-14} to 10^{-15} amps.). Such low currents are achieved by operating the electrodes at low potentials to minimize residual gas ionization, by using specially developed low temperature filaments to minimize photoelectric emission of electrons and by specially treating the glass to minimize leakage currents between the grid lead and other leads.

compared to 100°C for barium titanate. Beyond these temperatures the ceramic depolarizes.

The ceramic disc is sandwiched between a silver disc and silver diaphragm and mounted in a water tight cylindrical housing on a Lucite cup. A Teflon insulated lead from the silver disc is led through the side of the housing up a hollow tube to a connector. The tube wall and housing act as the lead from the diaphragm. Both the silver disc (.300" diameter x .020" thick) and the silver diaphragm (.001" thick) are cold soldered (Eccobond silver solder 56C. Emerson and Cummings, Canton, Mass.) to the positive and negative faces, respectively, of the ceramic. The housing consists of a hollow brass cylinder 7/16" O.D., 3/8" I.D., and 1/4" long with a 1/32" thick inner lip located 1/32" below the upper edge and projecting 1/32" into the interior of the cylinder. The silver diaphragm is hot soldered to the upper rim. The purpose of the inner lip is to add strength to the housing near the diaphragm during an accidental movement of the end of the stem with respect to the housing.

The Lucite cup is press fitted into the housing. A 0 - 80NF x 1/8" set screw is threaded into the Lucite. The set screw forces the ceramic disc up against the silver diaphragm. Eccobond epoxy 45 binds the silver disc to the Lucite cup. The same epoxy is also used to seal the set screw to the Lucite cup and the latter to the bottom of the housing.

The stem consists of a hollow stainless steel tube brazed to the side of the brass cylinder. The lead soldered to the silver disc is Teflon coated wire (stripped Amphenol cable No. 421-111 or Amphenol Teflon wire No. 414-106). It runs the length of the stem and projects about 1/2" beyond the end of the stem. The end is tipped with a center conductor tip from a BNC connector and the Teflon is epoxied to the stainless steel after the former has been etched with Tetre-Etch (W. L. Gore and Associates, Newark, Del.). The ceramic disc is thus completely sealed from moisture.

A modified BNC Teflon connector (UG 88/U) is slipped over the stainless steel tube end until the tip is flush with the lip of the connector and is secured by means of a set screw against the stainless steel. Fig. 12 is a photograph of one of the complete transducers.

The guiding principle in the construction of the transducer was to maintain the very high impedance across the ceramic disc and to minimize the lead capacitance. The reason for this will soon be apparent. Any moisture which might seep into the chamber housing the ceramic disc drastically affects the resistance between the faces and must be avoided at all costs; hence the strict attention to sealing. The use of Teflon coated wire and connector ensures that the resistance between the leads is at least as great as that across the ceramic disc; in addition the capacitance is quite low. Keeping the stem as short as possible also lowers the lead capacitance.

The method of assembling the transducer is as follows. The stainless steel tube is brazed to the brass cylinder and a hole drilled into the side of the brass. The diaphragm is then soldered to the upper rim of the housing. Following this the Teflon insulated wire is forced down the tube and the silver disc attached to its inner end. The other end is then etched. The disc is drawn out of the housing to permit the ceramic disc, coated with a thin film of cold solder on both faces, to be dropped in place against the diaphragm. The silver disc is swung back against the ceramic disc and the Lucite cup is press fitted into place. A small amount of epoxy is dropped into the threaded hole (enough to fill the space between the bottom of the silver disc and the Lucite) and the set screw, coated with epoxy, is screwed into the Lucite to push the ceramic up against the diaphragm. Epoxy is then applied to the joint at the bottom of the housing and to the projecting piece of Teflon wire. The setting of the epoxy and cold solder is hastened by placing the transducer in an oven at about 150 to 200°F for 1/2 hour.

During the entire assembly great care must be taken to ensure that the sides of the ceramic disc are completely free from moisture or perspiration. Keeping the discs in an acetone bath and handling them with metal tweezers was found worthwhile. In addition the diaphragm and housing assembly was also carefully washed in acetone prior to assembly.

The nine transducers were mounted in 1/2 " diameter holes on the mid-span line of the blade. 1/4" slots were milled from the holes to the top of the blade for the stems. In positioning the transducer in the blade the hole and slot were first packed with modelling clay and the transducer was pressed down into the modelling clay until the diaphragm was flush with the blade surface. The modelling clay was then scraped from around the stem and epoxy poured in to seal the stem to the blade.

It must be recognized that mounting the ceramic disc on epoxy in a Lucite cup and then epoxying the stem into the blade results in a transducer natural frequency that is low. The natural frequency of the ceramic disc in the Lucite cup was estimated to be about 30,000 cps. Thus the present transducer is limited in frequency range. However, as the present study was concerned with frequencies less than 20 cps the limitation does not apply. This was borne out by the results. Mounting the ceramic disc on glass instead of Lucite, or using a pedestal type mounting similar to Ruetenik would be necessary for studies of higher frequency phenomena.

5.3 Choice of Ceramic Dimensions

Following Ruetnik and Perkins it was decided to use a disc shaped sensing element. Actually, one of the major advantages of a prepolarized ceramic piezo-electric element is the fact that it can be obtained in any number of different shapes. However, the disc, because of its convenient and simple shape has many virtues.

The equivalent circuit for the ceramic is given in the following

diagram.
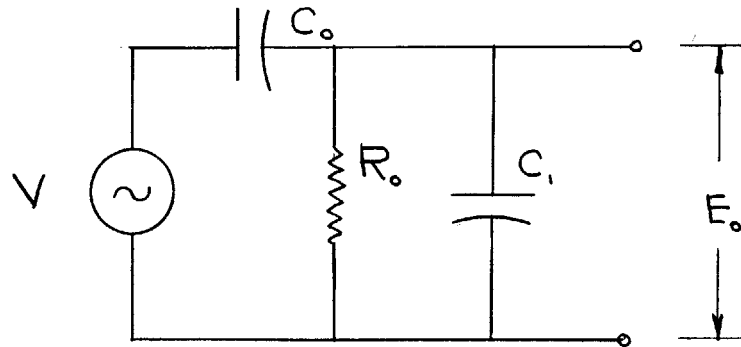
where V = voltage developed across the ceramic

E$_o$ = voltage read at the output of the complete transducer

C$_o$ = capacitance across the ceramic faces

R$_o$ = resistance of the disc

C$_1$ = capacitance of the leads

It can be shown (see Appendix 4) that

$$\frac{E_o}{V} = \frac{C_o}{C_1+C_o} \cdot \frac{2\pi f (C_1+C_o) R_o}{\sqrt{1 + \left[2\pi f(C_1+C_o)R_o \right]^2}} = \frac{C_o}{C_1+C_o} \cdot F(f)$$

It is obvious that it is most desirable to have the right hand side approach unity. The first term is a capacitance voltage dividing term. Clearly C$_1$ should be small compared to C$_o$. Hence the reason for the short leads. F (f) approaches unity for large values of f and/or R$_o$. Therefore, for optimum low frequency response R$_o$ should be as large as possible.

A more compelling reason for requiring a large R$_o$ can be found when we examine the behavior of the decay of a voltage applied to a capacitance. This decays as $e^{\frac{-t}{RC}}$. In this case the RC product is formed by the resistance and capacitance that the signal "sees" and hence includes the electrometer and what follows. It is obvious that RC should be as large as possible to secure minimum decay in the time period under consideration, i.e. R$_o$ $\doteq$ R must be as large as possible. A measure of the required value of RC can be obtained from the desired accuracy of the measurement as follows:

$$E = E_o e^{-\frac{t}{RC}} \doteq E_o \left(1 - \frac{t}{RC}\right)$$

Hence if the time period under investigation is 1 second RC should be at least 20 seconds for a 5% accuracy.

It may seem strange to require a large time constant. In most capacitance devices a short time constant is desirable thereby ensuring rapid response. However, in this case, the buildup of charge across the face of the ceramic disc is only a function of the speed of a pressure wave within the ceramic itself.

Now the capacitance between two parallel plates ℓ meters apart is given by

$$C_o = \frac{K \epsilon_o A}{\ell}$$

where ϵ_o = absolute dielectric constant of free space = 10.6×10^{-12} farads/meter

K = relative dielectric constant of medium between plates

= 1200 for US 500 (vs. 1000 for barium titanate)

A = area of the parallel plates

$$\therefore \quad C_o = \frac{1200 \times 10.6 \times 10^{-12}}{\ell} \cdot \frac{\pi d^2}{4}$$

Also, as shown in Ref. (4) and Ref. (17)

$$V = g_{33} \times \ell$$

where V = voltage generated across the disc faces

$$g_{33} = 38 \times 10^{-3} \frac{\text{VOLT / METER}}{\text{NEWTON / METER}^2} \quad \text{FOR US 500}$$

g_{33} is a measure of the sensitivity. The subscript 33 distinguishes this constant from others in directions other than parallel to the axis of the disc.

Thus, it is clear that for maximum capacitance C_o, d should be large and ℓ should be small. But for maximum signal ℓ should be large.

A further restriction on the dimensions of the ceramic arises when ℓ is of the order of d. The quoted value of g_{33} must be reduced somewhat if the two dimensions are about the same because the constant was determined for $\ell \ll$ d. The reduction cannot be calculated.

F(f), the frequency dependent function is plotted in Figs. 13a and 13b for disc sizes 0.250" diameter and 0.300" diameter as a function of thickness ℓ . It is seen that the smaller ℓ the better the low frequency response. However, it is clear that for these diameters, no reduction in signal occurs beyond 1 c.p.s.

$\dfrac{E_0}{V}$ and E_0 are plotted in Figs. 14a and 14b for the two diameters selected as a function of the thickness for different values of frequency. As ℓ increases $\dfrac{E_0}{V}$ decreases, but since V increases with ℓ , E_0 increases. The non linear correction for $\dfrac{d}{\ell} < 2$ would reduce E_0 for $\ell > .125"$ for the .250" diameter disc and for $\ell > .150"$ diameter disc for the .300" diameter.

5.4 The Electrometer Circuit

As indicated above, it is necessary to use an electrometer to transform the impedance level of the signal from the transducer. Commercial electrometers are available for this purpose. Most of these have additional amplifying stages built in. Amplification is necessary since the gain of any cathode follower is always less than unity. However, in the present study a single Raytheon CK 5886 electrometer tube was found to be adequate. This tube is several times less expensive than other commercially available electrometer tubes with no sacrifice in performance.

The circuit is shown in Fig. 15. The gain of the circuit is between .45 and .5. This is the same circuit used by Perkins and Ruetenik. The signal from the transducer is applied to the grid and the output is read across the cathode resistor.

An advantage of this simple circuit is that the tube can be mounted in a separate box and can be brought within close proximity to the transducer thereby reducing lead capacitance. All resistors and batteries can be assembled in separate resistance and battery boxes. The leads to the electrometer box can be as long as desired since they carry low impedance signals and stray capacitance effects are of little importance.

An electrometer box is shown in Fig. 16. The tube is mounted on rubber bands on insulated posts as shown in Fig. 17. The tubes actually used in obtaining the data contained in this report had their surfaces coated with Aquadag, a suspension of carbon in water (produced by Acheson Colloids Co., Port Huron, Mich.) and the graphite envelope was grounded. In assembling the tube in the box great care was taken to avoid actually touching the tube so as to minimize any leakage paths on the surface of the uncoated portion of the glass between grid and adjacent leads.

The tube specification sheet quotes maximum grid currents of about 10^{-15} amps. However, the manufacturer's tests were performed under controlled low humidity conditions. To achieve comparable grid currents it was necessary to assemble the electrometer tube box under low humidity conditions and seal it.

The resistance box is shown in Fig. 18 and a schematic is shown in Fig. 19. As the Sanborn recorder had two channels, two completely separate circuits were constructed. This is evident in Fig. 19. Each circuit had its own batteries.

Regular dry cells were used for batteries because of their availability. However, because of the extremely low currents in the plate and screen circuits ($< 10 \mu a$) mercury batteries could have been used in all circuits except the filament circuit. The current in the filament circuit is 10 ma and a regular 1.5^V battery is required.

Two electrometer boxes were liberally encased in foam rubber and placed

in a specially constructed sealed Lucite box. Leads to the Lucite box were cemented in place with connectors extending into the box to the two electrometer boxes. This was done to ensure that moisture could not seep into the electrometer boxes to affect leakage currents. The Lucite box was then placed into a black box to further minimize light induced photoelectric emission. This black box is visible in Fig. 8, in which can also be seen the high impedance leads carrying the signal from two of the nine transducers. The short length of connecting cable was an Amphenol noise free cable, no. 21-541 (made noise free by the application of a semi-conductive coating to the dielectric which prevents the buildup of static charge on the high impedance signal carrying cable). The thinner cable shown is that carrying the leads from the resistance box, one of which is the low impedance output lead from the electrometer.

5.5 Measurement of Pressure

The Sanborn recording unit used in this report comprised two DC preamplifiers, two DC amplifiers and a two channel mechanical chart recorder. Initially the pressure signal was fed from the transducer via the electrometer to the DC pre-amplifier from which it went via the DC amplifier to the recorder. The combined gain was 50. The input impedance to the grid of the DC pre-amplifier is about $10^7 \Omega$. As the output impedance of the signal from the electrometer is about $1.5 \times 10^5 \Omega$ the Sanborn did not attenuate the signal.

However, it was found that an additional gain of 2 to 5 was necessary. A Kin-tel DC amplifier, supplied by the Hydrodynamics Laboratory, was used for this purpose. The electrometer output was fed into the Kin-tel and then to the DC pre-amplifier. The Kin-tel had an input impedance of $5 \times 10^4 \Omega$ with the result that the signal suffered a further attenuation by about two thirds. This was compensated by increasing the gain on the Kin-tel. However, the input capacitance was much larger than that of the Sanborn DC pre-amplifier. This

resulted in a reduced time constant. Calibration traces (discussed in section 5.6) show time constants of about 7 seconds compared to greater than 1 minute in the absence of the Kin-tel. The use of an additional shunt capacitor was avoided because of noise/signal problems.

The procedure used in recording pressures was as follows. The Sanborn was balanced. The electrometer grid was grounded and the cathode voltage was adjusted by means of the screen grid potentiometer to $2^\vee$ above ground. This meant that the grid was at $-2^\vee$ which, from the tube characteristic, corresponds to minimum grid current. The electrometer output lead was then plugged into the Sanborn and the Sanborn balanced by means of the 100 K Ω output potentiometer. The transducer was connected to the electrometer and the Sanborn was rebalanced using the screen grid resistor. After about 5 minutes, equilibrium between electrometer and Sanborn prevailed and the screen grid resistor was given a final adjustment. The VTVM was removed from the cathode circuit. The pressure change was then initiated and recorded. Subsequent pressure changes could be recorded within about 1 minute. All balancing was done with the screen grid potentiometer.

When not connected to the electrometer each transducer was shorted at ground potential. When in running water, a simple shorting was sufficient since the diaphragm was at ground potential. In between runs, ground leads were connected to the shorting plugs.

The electrometer batteries were left on when the electrometer was not in use. This caused very little battery drain (except in the filament circuit) because of the minute currents drawn, and allowed the electrometer tube to maintain a stable equilibrium condition.

Switches were included in all circuits, except the filament circuit, so that the electrode potentials could be removed if necessary. In such a case 24 hours was allowed for the tube to reach equilibrium after being dis-

connected for a few days. No switch was included in the filament circuit because it was found that should the other voltages be applied before the filament voltage the cathode voltage never attained its value of $+ 2^{\vee}$. Thus the filament voltage was always applied before the others following a shut down and removed after the others before a shut down.

The filament batteries were found to last about a month when in continuous operation.

It is worthwhile mentioning, at this point, that the cathode voltage showed a tendency to drift away from $+ 2^{\vee}$ except under certain conditions, and that should the grid be left open, reached a value of $-12^{\vee}$. This meant that the tube was cut off and no current could flow past the grid; ie. electrons flowing to the grid make the grid more and more negative until all further electrons are repelled and current ceases to flow.

The tendency for the grid to go increasingly negative was particularly evident during calibration. It was also observed to occur in the running water should the ceramic be placed in the transducer with the negative face to the grid. However, with the positive face to the grid the cathode remained at $+ 2^{\vee}$ when the transducer was immersed in running water. The explanation for this is thought to lie in the turbulent pressure fluctuations of the flow. The pressure fluctuations have the effect of knocking the arrested electrons off the grid and hence the flow of plate current is unimpeded. When the ceramic is connected with its negative face to the grid the grid appears to become progressively negative in spite of the fluctuations. Why this is so is not known. Nevertheless small fluctuations are definitely needed because cut off occurs even when the ceramic is assembled as in Fig. 8 during calibration.

It was found that grounding was critical. Care was taken to avoid ground loops. The only grounding point in each complete circuit was the diaphragm. The chassis of the Sanborn was also grounded.

5.6 CALIBRATION

The transducers were calibrated while in place in the blade. The blade was placed in a Lucite box (14" x 7 1/4" x 3"). The blade was suspended from the top of the box which was fastened to the body of the box by means of 22 screws. A rubber gasket ensured proper sealing of the top to the box. The calibration box is shown in Fig. 20.

Nine holes were drilled in the top of the box to accommodate the transducer stems. Sealing of the stems to the top was affected by means of O rings compressed by stuffing box nuts.

Once the stems were sealed the modified BNC connectors were placed back on the stem.

A hole was drilled in the side of the calibrating box and a piece of tygon tubing was led to a small thistle shaped funnel which acted as a reservoir. The funnel was secured to a water height gauge. The top of the reservoir was open to atmosphere. The box and reservoir were filled with water and after all air bubbles were removed, calibration was achieved by suddenly dropping the reservoir a known amount (1", 1/2", etc.) and recording the pressure signal on the Sanborn. A sample calibration trace is shown in Fig. 21. The time constant can readily be determined from the trace by measuring the time taken for the signal to decay to 63% of its initial value. The initial value is determined by extending the straight part of the trace back to the beginning of the step change by a straight line. This is permissible in view of the large time constants. The fluctuations at the beginning of the trace are caused by pressure waves set up by the sudden pressure change. However, the final pressure change can only be the difference in reservoir height since no flow of water is involved.

During calibration the stem was grounded since the water at the diaphragm was not at ground potential. Drift of the cathode was encountered as mentioned above.

The procedure during calibration was as follows: The transducer and electrometer were both shorted at ground potential. The cathode voltage was adjusted to 2^V. The electrometer output was connected into the measuring circuit. The Sanborn was balanced by means of the output potentiometer. The transducer was connected to the grid, the Sanborn was quickly balanced by means of the screen grid potentiometer and the reservoir was dropped. The reservoir could be raised several times and the transducer calibrated five or six times before balancing the Sanborn with the screen resistor probed ineffective.

Calibration values of 10 mv/"H_2O were usual. This corresponds to a gain in the electrometer of 0.47.

Should moisture somehow seep into the transducer (generally through a minute hole in the diaphragm) it could always be detected by observing the time constant. Moisture reduced R_O and hence RC fell off drastically. In such a case the transducer had to be removed, taken apart and reassembled.

In removing and repositioning the stem connectors for calibrating purposes, care was taken to avoid touching the Teflon near the tip. Also the connectors were bathed in acetone to remove any oil or moisture. If the stems were suspected of being contaminated they too were washed with acetone.

6. EXPERIMENTAL RESULTS

6.1 INTRODUCTION

The initial experiments were carried out in a specially designed water table at the Gas Turbine Laboratory. The special feature of this table was a wire screen belt which traversed the table at right angles to the flow. A sudden on-off movement of the belt imparted a velocity component perpendicular to the main stream for a brief instant thereby creating a jet of narrow thickness perpendicular to the main stream. The jet simulated the wake of Fig. 2.

However, it was discovered that the noise level in the table was of the same order as the small signal generated by the wake. Subsequent experiments

were carried out in the 24" tilting flume of the Hydrodynamics Laboratory made available with the cooperation of Professor J. W. Daily. The means of wake generation was altered to that described in Section 5.

At first, solid cylinders were used as wake generators. Pressure wave effects, due to the acceleration and subsequent deceleration of the solid cylinders, were observed. In an effort to minimize these effects the blade box was positioned an additional 6" downstream of the slotted box and a spacer, with a top of a nest of wire mesh screens to act as a pressure wave damper, was inserted between the two boxes. This proved to be partially successful.

The use of screen cylinders as wake generators, as described in Section 5, in addition to the pressure wave damper, proved to be a solution to the problem of pressure wave effects.

The results discussed in Section 6.2, represent the average of ten or so pressure records of the same event. This was done in an effort to average out random signals: in particular, those due to turbulence. The resulting pressure traces would have been smoother if, say, one hundred or one thousand records had been averaged, but ten was chosen as the maximum number which could be handled conveniently.

The transducers were calibrated periodically before the pressure results included in this report were obtained. The calibration values were found to be constant to within 2 or 3%, which is within the accuracy of the pressures obtained in Section 6.2. The actual calibration values used were those obtained upon the completion of the reported experiments.

6.2 RESULTS

Fig. 22 shows velocity profiles in the wake of screen cylinders numbers 1 and 5. The profiles were obtained behind the stationary cylinders in a two-dimensional free stream of velocity 4.75 ft/sec at a distance of 25.85". The velocity corresponds to the relative velocity to the cylinder during its travel

across the flume; the velocity was selected to make the wake centerline in-
tersect the chord line at 90°. 25.85" is the distance that the wake which
reaches the leading edge, assuming it was swept by the free stream along the
flume centerline, would be behind the cylinder when the cylinder travel is
hypothetically extended beyond the flume wall. All the tests were conducted
with a free stream velocity of 2.77 ft/sec.

Fig. 23 shows a sequence from a movie taken of the wake generated by cy-
linder number 1 as it passes over the blade. The wake is made visible by po-
tassium permanganate traces.

Fig. 24 shows a typical pressure trace. The origin of the time scale is
the instant the motion of the cylinder was initiated. This particular trace
is of transducer No. 1 and shows a record of the pulse generated by No. 5 cy-
linder. The pressure trace is the lower record. The pressure increases in
the downward direction. The upper trace is a record of the cylinder velocity.
Peak cylinder velocity is 5.5 ft/sec.

Figs. 25a and 25b show pressure records for the entire blade due to the
wake generated by cylinder No. 1, Fig. 25a showing the suction side of the
blade and Fig. 25b the pressure side. Superimposed on both figures are the
predicted pressure variation before the arrival of the wake as calculated by
the theory of Section 4.2.

Figs. 26a and 26b show similar records for the wake generated by cylinder
No. 5. Superimposed predicted curves calculated by the theory of Section 2.2
are also shown.

Figs. 27a, 27b and 27c show pressure records for transducer No. 1 due to
8 different wakes generated by the 8 different wake generators travelling at
the maximum velocity of the apparatus, the relative velocity to the cylinder
being 6.83 ft/sec. Predicted curves are also shown.

Fig. 28 shows the results of the source solution calculated by feeding the time varying coordiantes of the cylinder of the cylinder as the path of the source and using as source strength that strength which would yield a body whose thickness was equal to the displacement thickness of the wake in a free stream of velocity equal to the relative velocity of the flow to the cylinder.

Fig. 29 shows the results of a similar calculation for the doublet solution, using the same path as the source solution and as doublet strength that strength which would yield a cylinder of the diameter of the screen cylinder in a free stream of velocity equal to the relative velocity.

Fig. 30 shows the result of integrating the pressures over the blade to form lift coefficients for cylinders No. 1 and No. 5. The results are compared with those predicted: No. 1 with the extended theory and No. 5 with the unmodified theory.

Fig. 31 is a plot of C_W, the wake coefficient, versus time for the two cases of Fig. 30, where C_W is defined by

$$C_W = \frac{L}{c\rho V \bar{W}}$$

L being the unsteady lift force per unit span and $c\rho V\bar{W}$ being a measure of wake perturbation dynamic head per unit wake width.

7. DISCUSSION

7.1 INTRODUCTION

This Section compares the experimental results of Section 6.2 with the theory of Sections 2, 3 and 4. The result which generated the most surprise during the course of this study was the appearance of a pressure signal at the blade in advance of the arrival of the wake at the blade's leading edge. This is discussed in Section 7.4. To lend some form of orderliness to the discussion, the effects mentioned in Sections 2, 3 and 4 will be discussed in that order in Sections 7.2, 7.3 and 7.4 Section 7.5 deals with a discus-

sion of the overall force on the blade and mentions the results of Kemp and Sears calculation of the circulation effect.

7.2 WAKE EFFECT

At the onset it must be pointed out that a velocity defect of 1 ft/sec in a free stream of about 3 ft/sec cannot be considered as a small perturbation; in particular, the angle of attack at the leading edge is about 20°. It was recognized that boundary layer separation could occur at large angles of attack. However, to obtain measurable pressure signals it was found necessary to resort to the large velocity defects used. In an actual compressor operating at its design point the velocity defect is much closer to 1/10th. of the free stream velocity. Nevertheless, several qualitative conclusions can be made which have a direct bearing on the compressor problem.

From t_0' of +.6 onwards the thin airfoil theory of Section 2.2 and the extended theory of Section 2.3 yield virtually identical results. This means that from .95 seconds on in Figs. 25 and 26, and from .72 seconds on in Fig. 27 the theoretical predictions are, for all practical purposes, the same.

Once the wake has left the blade the pressures follow the trend predicted. Figs. 25b and 26a reveal quite good agreement for transducers No. 1 and No. 2 respectively. The agreement for transducers No. 4 and No. 8 of Fig. 25b and of No. 2 and No. 4 in Fig. 26b is fairly good. The discrepancies in the other traces can be ascribed to the high noise level. Agreement prevails almost to 2.4 seconds in Figs. 27a and 27b; this can be linked to the larger signal to noise ratio.

The predicted instant the centerline of the wake reaches the blade seems to be later than actually observed in Figs. 25 and 26 and earlier than observed in Fig. 27. The procedure for calculating the instant of centerline arrival is outlined in Appendix 5.

From the time the wake leaves the trailing edge until it has travelled a chord length or so there seems to be a recovery of suction pressure on the suction side. Why this is so is not known at the present time.

The extended theory of Section 2.3 predicts the peak pressure in Fig. 25 to within 32% at best. The agreement, while poor, is still an improvement over the theory of Section 2.2. The explanation is thought to lie in the comparatively large angle of attack of the flow at the leading edge. The general trend of the early part of the predicted pressure trace agrees fairly well with the experimental trace.

7.3 WAKE DISTORTION EFFECT

The divergence of the predicted and the actual pressure traces while the wake is on the blade is quite striking. The general shape of the divergence is as predicted by Meyer (as shown in Fig. 4). The relative distortion parameter of No. 1 cylinder's wake is 1.8 hence the distortion is even more marked than for the case Meyer calculated ($D = 1.08$). In addition, the wake is wider ($\lambda_{*1} = .20$, compared to $\lambda = .15$). The effects of viscosity appear to enter the picture and cause the distortion effect to act over a larger interval, particularly beyond the first few stations.

Thus the results show that there is a distortion effect as predicted by Meyer; in an actual machine D is about 1 and therefore its effects need to be considered.

7.4 BLADE THICKNESS EFFECT

7.4.1 Justification of Simplifying Assumptions

As pointed out earlier in this Section the appearance of a pressure signal well before the wake reached the blade was quite surprising. After careful investigation both electrical effects and pressure wave effects were ruled out. The signal could only come from the wake generator.

In an effort to obtain an engineering solution the cylinder was regarded as a moving source and the blade as a semi-infinite flat plate. Regarding the blade as semi-infinite meant that unsteady circulation effects did not have to be taken into account. This simplification is not as drastic as it might seem for the effects of shed vortices would not be apparent in the initial instance when the solution is to apply. Also, the semi-infinite length does not affect the pressure near the front of the blade. To show this qualitatively use was made of equation (6), valid for a finite blade in a sinusoidal gust.

Consider the point a distance m from the leading edge of the blade in the following sketch
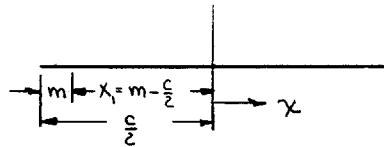
$$\cos\theta\Big]_{x=x_1} = \frac{2m}{c} - 1$$

Then

$$\frac{P_{x=x_1}\Big]_{c=1}}{P_{x=x_1}\Big]_{c=1000}} = \frac{\big[\,S(\omega)\tan\frac{\theta}{2}\,\big]_{c=1}}{\big[\,S(\omega)\tan\frac{\theta}{2}\,\big]_{c=1000}}$$

compares the pressures at the same point near the leading edge for blades of chord 1 and 1000 feet, respectively. Assuming a disturbance of 1 cycle per second in a free stream of velocity 3 ft/sec the reduced frequencies for the two cases are approximately 1 and 1000, respectively. Hence the Sears functions are approximately .35 and .009, respectively. The two tangents are 3 and 100, respectively, for m = .1 ft. Hence the pressures are in the same ratio 1.05 : 0.9. This shows that the effect of the semi-infinite blade length simplification is minor for stations near the leading edge of the blade.

7.4.2 Source Solution

From standard texts on potential flow theory (see, for example, Ref. (18)) the strength of a source required to yield a body of thickness h far from the source in a stream of velocity U is $Q = Uh$ ft^2/sec

In the calculation of Fig. 28, h was chosen to be the total displacement thickness δ_T^* across the wake defined as

$$\delta_T^* = \int_{-\infty}^{\infty} \left(1 - \frac{u}{U}\right) d\xi$$

δ_T^* for the wake of Fig. 25 was .530" while for the wake of Fig. 26, it was .598".

In the integration of equation (32) (and, for that matter, of equation (40)) where integrals of the form $\int \frac{f(x)}{\sqrt{x}} dx$ had to be evaluated, use was made of the following manipulation

$$\int_0^x \frac{f(x)}{\sqrt{x}} dx = \int_0^x \frac{f(x)-f(0)}{\sqrt{x}} dx + \int_0^x \frac{f(0)}{\sqrt{x}} dx = \int_0^x \frac{f(x)-f(0)}{\sqrt{x}} dx + 2\sqrt{x}\, f(0)$$

and the resulting integral was evaluated graphically. Subsequent differentiations with respect to time was also done graphically.

Fig. 28 is the result of the solution of equation (19) using (32) with $\gamma_0(t)$ being the path of the cylinder as determined by the integration of the cylinder velocity record, (upper part of Fig. 24). The pressure is seen to rise on the suction side and fall on the pressure side, reaching a peak around .45 seconds. The values of $x_0(t)$ and $y_0(t)$ beyond $t = .485$ sec. (when the cylinder is actually brought to a stop) were obtained by extrapolating the integrated cylinder velocity curve in time. Thus, this part of the solution is largely hypothetical.

The actual curves should really start from zero pressure for the source at time $t = 0$ actually has zero strength. The cylinder has completed its acceleration by time $t = .20$ secs.

The curve for $x = .1$ ft and $x = .2$ ft are shown superimposed on Figs. 25a and 25b, respectively. These positions were chosen for ease of calculation; transducers Nos. 1 and 2 are located at .0833 ft and .1667 ft from the leading edge, respectively. The agreement with experiment is only fair but the predicted curves do give pressures of the same order of magnitude as those

measured and at about the same time. The agreement is sufficient to show that the early part of the pressure trace is due to induced effects arising from the potential effect described in Section 4.

There is no reason to expect this effect to be restricted to the present experiment, i.e. there is every reason to expect a similar effect to occur in an actual compressor. For that reason it has been called a blade thickness effect and has been listed separately from the effects of Sections 1, 2 and 3 as a cause of unsteady blade forces.

7.4.3 Doublet Solution

From Ref. (18) the strength of the doublet to give a cylinder of radius "a" in a stream of velocity U is

$$\mu = a^2 U \quad ft^3/sec$$

Fig. 29 is the result of the calculations using the same path for $\Upsilon_0(t)$ as in Section 7.4.2 and the above formula for μ where a is the radius of the cylinder. The predicted pressures are too low by a factor of close to 5. However, the shape of the predicted curves are remarkably similar to those of Figs. 27 and 26a.

7.5 UNSTEADY FORCE

For engineering purposes one is primarily interested in the overall force rather than a detailed pressure distribution. Accordingly the pressures of Figs. 25 and 26 were integrated across the blade to obtain the unsteady force. Fig. 30 shows the result of the integration. The unsteady force is plotted as an unsteady lift coefficient calculated by the theory of Sections 2.2 and 2.3.

The three effects are readily apparent, the blade thickness effect resulting in a negative force before the wake reaches the blade, the wake effect and the wake distortion effect. The unsteady force due to the blade thickness effect amounts to between 12 and 25% of the peak unsteady force.

Agreement between the peak predicted values of Section 2.3 and the exper-imental values is not as good as with the pressures of Fig. 25. This, however, can be explained. The maximum pressure perturbations occur close to the lead-ing edge. Transducer No. 1 is 1" back and transducer No. 2 is 2" back of the leading edge on the other side of the blade. In plotting up chord-wise pres-sures for the different times and joining them by a smooth curve to pass through the leading edge a large part of the total force due to the large pressure perturbations at the leading edge is missed.

Thus, the maximum lift coefficient determined by smooth curve integration is .23. However, it is reasonable to expect the integrated pressure curves to give as close, if not closer, agreement to the predicted curves as the in-dividual pressure curves. Now the pressures were found to be about 35% too low. Hence, assuming the lift coefficient to be 35% too low, this brings the corrected peak of the curve up to about .33.

In fact, the whole unsteady lift coefficient curve should probably be increased by 50% from the time the wake reaches the leading edge to about the time it is a chord length past the blade. After that time the effect of the blade very close to the leading edge is not too different from that which the smooth curve integration yields.

No attempt has been made to predict exactly the modifying influence of the wake distortion effect; Fig. 4, obtained from Meyer's corrected solution merely shows that it can be predicted. The reason for this is that its ef-fect is to decrease the unsteady force on a compressor blade. Hence, for engineering purposes a design based on the theory of Section 2.3 would be con-servative in predicting the load while the wake is on the blade.

Fig. 31 shows the variation of C_W with time. Its variation is much the same as C_L in Fig. 30. Fig. 31 is included because, from equation (8), C_W should be independent of the wake shape for narrow wakes and hence one should be able to draw a single curve.

7.6 CIRCULATION EFFECT

To complete the discussion it is perhaps appropriate to mention the results of Kemp's and Sears' calculations, Ref. (1), and to compare them with the results of this report. They found that the unsteady lift on a stator blade in a cascade due to the relative motion of an adjacent downstream rotor cascade could be as high as 18% of the steady lift depending on the axial distance between rows and chord-wise distribution of bound vorticity on the rotor blades.

Assuming a steady lift coefficient of 1 (which is probably a bit high) the peak measured unsteady force due to the wake effect amounts to 23% of the steady lift and, most likely, is as high as 33%. Hence, the unsteady force due to the wake effect, which can be predicted by the methods outlined in Section 2.3, is the major contribution to the total unsteady force.

8. CONCLUSIONS

The results of the present series of experiments reveal that the basic theory devised by Meyer is generally valid in describing the unsteady pressure distribution over a thin airfoil during the passage of a wake. The theory has been extended to cover the case of typical wakes which are narrow but not thin in the mathematical sense. The modified theory has been found to give pressure peaks which are about 35% too high. The discrepancy is thought to be due to the large angle of attack and the concommitant separation. At low angles of attack, as actually occur in turbomachines running at design conditions, the possibility of boundary layer separation would not arise and the modified theory should predict the pressures very closely.

The effects of wake distortion while the wake is on the blade, are to decrease the blade unsteady force.

The peak unsteady force due to the velocity defect in the wake amounted to at least 23% and probably 33% of the steady lift, assuming a steady state

lift coefficient of 1. The actual value in a given case can be determined by the methods of Section 2.3.

The effect of velocities induced at the blade before the arrival of the wake by the body generating the wake has been found to result in an unsteady force whose maximum value is between 3 and 5% of the steady force; it acts to oppose the steady force.

9. BIBLIOGRAPHY

1. Kemp, N. H. and W. R. Sears - "Aerodynamic Interference Between Moving Blade Rows" - Journal of the Aeronautical Sciences, Vol. 20, 1953, pp. 585 - 598

2. Kemp, N. H. and W. R. Sears - "The Unsteady Forces Due to Viscous Wakes in Turbomachines" - Journal of the Aeronautical Sciences, Vol. 22, 1955, pp. 478 - 483

3. Meyer, R. X. - "The Effect of Wakes on the Transient Pressure and Velocity Distributions in Turbomachines" - Transactions of ASME, Vol. 80, 1958, p. 1544

4. Ruetenik, J. R. - "Development of a Miniature Pressure Transducer for Application to Airfoil Studies in the Shock Tube" - WADC Technical Report 58-629, ASTIA Document No. 206259, December 1958

5. Küssner, H. G. - "Zusammenfassender Bericht über den instationären Auftrieb von Flügeln" - Luftfahrt-Forschung, Vol. 13, 1936, pp. 410 - 424

6. von Karman, T. and W. R. Sears - "Airfoil Theory for Non-Uniform Motion" Journal of the Aeronautical Sciences, Vol. 5, 1938, pp. 585 - 597

7. Yeh, H. - "Sears Function in Unsteady Flows" - Reader's Forum - Journal of the Aeronautical Sciences, Vol. 24, 1957, pp. 546 - 547

8. Meyer, R. X. - "Interference Due to Viscous Wakes Between Stationary and Rotating Blades in Turbomachines" - Dr. of Eng. Thesis - Johns Hopkins University, 1955

9. Küssner, H. G. - "Das zweidimensionale Problem der beliebig bewegten Tragfläche unter Berücksichtigung von Partialbewegungen der Flüssigkeit" Luftfarht-Forschung, Vol. 17, 1940, pp. 355 - 361 - Translation:Ministry of Aircraft Production, RTP. Translation 1541

10. Yeh, H. and J. J. Eisenhuth - "The Unsteady Wake Interaction in Turbomachinery and Its Effect on Cavitation" - Transactions of ASME - Journal of Basic Engineering, Series, D, Vol. 81, 1959, pp. 181 - 189

11. Sears, W. H. - "Some Aspects of Non-Stationary Airfoil Theory and Its Practical Application" - Journal of the Aeronautical Sciences, Vol. 8, 1941, pp. 104 - 108

12. Kemp, N. H. - "On the Lift and Circulation of Airfoils in Some Unsteady Flow Problems" - Reader's Forum - Journal of the Aeronautical Sciences, Vol. 19, 1952, pp. 713 - 714

13. Interpolation and Allied Tables" - H. M. Nautical Almanac Office - H. M. Stationery Office - London - 1956

14. Bisplinghoff, R. L., H. Ashley and R. L. Halfman - "Aeroelasticity" - Addison-Wesley Publishing Co., Inc. - Reading, Mass. - 1955 - Chapter 5

15. Hildebrand, F. B. - "Advanced Calculus for Engineers" - Prentice-Hall, Inc. - Englewood Cliffs, N. J. - 1949

16. Schubauer, G. B., Spangenberg and P. S. Klebanoff - "Aerodynamic Characteristics of Damping Screens" - NACA TN 2001 - 1950

17. Perkins, F. E. and P. S. Eagleson - "The Development of a Total Head Tube for High Frequency Pressure Fluctuations in Water" - M. I. T. Hydrodynamics Laboratory - Technical Note No. 5 (see also Technical Report No. 46)

18. Rauscher, M. - "Introduction to Aeronautical Dyanmics" - John Wiley and Sons, Inc. - New York - 1953, Chapter 6

10. NOMENCLATURE

A = area

a = radius of cylinder

b = 1/2 of the total wake half width

b = constant

C = capacitance

C_L = lift coefficient

C_W = wake coefficient

c = blade chord

c = constant

D = relative wake distortion parameter

d = diameter of transducer ceramic disc

E = voltage input to electrometer

F = frequency parameter

f = frequency

g_{33} = ceramic piezo-electric constant

h = thickness of body generated by source in free stream

K = relative dielectric constant

k_2 = function used by Küssner in Ref. (9)

L = lift force per unit span

ℓ = thickness of transducer ceramic disc

m = distance from leading edge of blade

p = pressure perturbation

Q = source strength

R = resistance

S = Sears function tabulated in Ref. (7)

T = function used by Meyer in Ref. (3)

$t' = \dfrac{t}{c/2 \over V} = \dfrac{Vt}{c}$ = non-dimensional time reckoned from instant wake centerline reaches blade mid-chord

U   = free stream velocity

U   = peripheral wheel velocity

u   = perturbation to free stream velocity

V   = free stream velocity

V   = voltage generated by ceramic transducer

V_{r_T} = relative velocity of through flow

V_{r_W} = relative velocity of wake flow

V_T = absolute velocity of through flow

V_W = absolute velocity perpendicular to free stream velocity

v   = perturbation velocity perpendicular to free stream velocity

$W = \int_{-\infty}^{\infty} w(\xi)\,d\xi$ = integrated wake velocity defect

$\overline{W} = \dfrac{1}{c} \int_{-\infty}^{\infty} w(\xi)\,d\xi$ = integrated wake velocity defect per unit chord

w   = wake velocity defect

β = angle between wake centerline and blade chord line

γ = vorticity distribution

γ^*_T = total wake displacement thickness

ϵ_o = absolute dielectric constant of free space vector in

ζ = vector in complex plane

η = y coordinate in complex plane

θ = angle defined by x' = cos θ

Λ = wake function defined in equation (16)

λ = wake thickness parameter

μ = doublet strength

ν = circular frequency of oscillation

ξ = distance within wake from centerline of wake axis

ξ = x coordinate in complex plane

$\xi' = \dfrac{\xi}{c/2}$ = non-dimensional wake coordinate

ρ = density

φ = perturbation velocity potential

$\omega = \dfrac{\nu}{\dfrac{V}{c/2}} = \dfrac{\nu c}{2V}$ = reduced frequency

11. APPENDICIES

APPENDIX 1 OUTLINE OF THIN AIRFOIL THEORY

Consider the model of Fig. 2. The $w(\zeta)$ velocity defect is considered to extend to infinity in both directions.

As a first step in the solution consider the case of a flat plate advancing with velocity V into an inclined sinusoidal gust of amplitude v_o, $(v_o << V)$, inclined at angle β to the plate.

$$\therefore \quad v_g = v_o e^{-i(x'-t')\omega}$$

and

$$u_g = -v_o \cot \beta \, e^{-i(x'-t')\omega}$$

where u_g and v_g are the perturbation velocities in the absence of the plate.

The blade is replaced by a vorticity distribution $\gamma(x, t)$ consisting of two parts: γ_o, the quasi-steady vorticity and an additional vorticity γ_1 described below. γ_o gives rise to a vertical component of velocity v_α which just cancels v_g.

Meyer shows that

$$\gamma_o = 2 v_o e^{i\omega t'} \left[J_o(\omega) \frac{1 - \cos\theta}{\sin\theta} + 2 \sum_{l=1}^{\infty} (-i)^l J_l(\omega) \sin l\theta \right]$$

where J_o, J_1, etc. are Bessel functions of the first kind.

The sinusoidal perturbation causes the circulation about the blade to change and thus must result in a shedding of trailing vorticies to conserve circulation. The strength of the trailing vorticity at a given point must be sinusoidal in time, because of the linearity of the problem, and must occur at the same frequency as the disturbance. v_g and the shedding of vorticity are not in phase. Using a result of von Karman and Sears, Ref. (6), Meyer shows the trailing vorticity ϵ to be

$$\epsilon(s') = -2\pi v_o e^{i\omega(t'-x')} \frac{J_o(\omega) - iJ_1(\omega)}{K_o(i\omega) + K_1(i\omega)}$$

where s' is the distance from the blade trailing edge

K_o and K_1 are modified Bessel functions of the second kind

Now the trailing vorticity, in turn, gives rise to a component of velocity perpendicular to the plate. This is cancelled by placing additional vorticity γ_1 , along the chord line. Using another relation from Ref. (6), Meyer deduced that the above trailing vorticity results in a vorticity distribution of

$$\gamma_1 = -2v_0 e^{i\omega\tau'} \frac{J_0(\omega)-iJ_1(\omega)}{K_0(i\omega)+K_1(i\omega)} \sqrt{\frac{1-x'}{1+x'}} \int^{\infty} \frac{1}{s'-x'} \sqrt{\frac{s'+1}{s'-1}} e^{i\omega s'} ds'$$

Hence the total vorticity required to replace the blade and satisfy the boundary conditions is

$$\gamma = \gamma_0 + \gamma_1$$

This results in an induced velocity $u_\propto$ given by

$$u_\propto = \pm \frac{\gamma}{2}$$

Hence the total induced velocity is

$$u = u_g \pm \frac{\gamma}{2}$$

The unsteady Euler equation in linearized form may be written

$$\frac{\partial p}{\partial x} = \mp \frac{\rho}{2} \left(\frac{\partial \gamma}{\partial t} + V\frac{\partial \gamma}{\partial x} \right)$$

from which one may solve for $\frac{\partial p}{\partial x}$ by substituting $\gamma = \gamma_0 + \gamma_1$ and thus obtain

$$\frac{\partial p}{\partial x} = \pm \frac{2\rho v_0 V}{c} e^{i\omega\tau'} \frac{S(\omega)}{(1+x')(1-x'^2)^{1/2}}$$

Integration of this gives equation (6). Meyer then applied the above result to the case of a single wake of finite width. To do this he set

$$v_0 = 2 \frac{W}{c} f(\lambda\omega) d\omega$$

where $f(\lambda\omega)$ is a function whose Fourier transform is given by $g(\xi/b)$ wher $g(\xi/b)$ describes the wake profile according to

$$u_g = -\frac{W}{b} \cos \beta \cdot g(\xi/b)$$

and $$v_g = \frac{W}{b} \sin \beta \cdot g(\xi/b)$$

with $2b = \frac{W}{W_{max}}$, $2b$ being a measure of the total wake half width, and

$\lambda = \dfrac{2b}{c\sin\beta}$, λ being a measure of the ratio of the wake to chord width.

Upon substituting the expression for v_o into the pressure gradient equation

$$\frac{\partial p}{\partial x} = \pm \frac{4\rho V W}{c^2} \cdot \frac{1}{(1+x')(1-x'^2)^{\frac{1}{2}}} \int_{-\infty}^{\infty} f(\lambda\omega) S(\omega) e^{i\omega t'} d\omega$$

Meyer shows that if the wake profile can be represented by a Gaussian distribution, i. e. if

$$g(\xi/b) = \frac{1}{\sqrt{2\pi}} e^{-\frac{1}{2}\left(\frac{\xi}{b}\right)^2}$$

and if

$$\lambda \rightarrow 0$$

then

$$\frac{\partial p}{\partial x} = \pm \frac{2\rho V W}{\pi c^2} \cdot \frac{1}{(1+x')(1-x'^2)^{\frac{1}{2}}} \int_{-\infty}^{\infty} S(\omega) e^{i\omega t'} d\omega$$

which is equation (1).

Meyer also shows that by setting $g(\xi/b) = \delta(\xi/b)$

where $\delta(\xi/b)$ is Dirac's δ function,

i. e. $\qquad\qquad \delta(\xi/b) = 0 \qquad$ for $\qquad \xi/b \neq 0$

and $\qquad\qquad \displaystyle\int_{-\infty}^{\infty} \delta(\xi/b)\, d(\xi/b) = 1$

then $\quad f = \dfrac{1}{2\pi}$ and the same result ensues.

APPENDIX 2   CALCULATION FOR WAKES OF FINITE THICKNESS

Two methods can be used, both of which involve graphical integration for $\Lambda(t_0')$ which is required since

$$p(\theta,t_0') = \mp \frac{\rho V}{c} \Lambda(t_0') \tan\frac{\theta_0}{2} \tag{15}$$

where

$$\Lambda(t_0') = \frac{c}{2}\int_{-\infty}^{\infty} w(\xi)\, T(t_0'+\xi)\, d\xi' \tag{16}$$

or

$$\Lambda(t_0') = -\frac{c}{2}\int_{-\infty}^{\infty} k_2(t_0'+\xi)\frac{dw}{d\xi'}\, d\xi' \tag{17a}$$

Both methods have been used and have given equivalent results. The singularity at $t' = -1$ has been found to be slight. Whenever the singularity was present, (while the wake was coming onto the blade) the function was calculated from $t' = -.999$ and the graphical integration was carried out from $t' = -1$. This was checked against a graphical integration from $t' = -.999$ and analytical integration from $t' = -1$ to $t' = -.999$. The results were found to be identical. The analytical integration was done as follows.

From Küssner, Ref. (9)

$$k_2(t') = k_2(2\sigma-1) = \sigma\sum_n h_n(-\sigma)^n$$

where

$$\sigma = \frac{t'+1}{2}$$

and the first 3 coefficients in the series are

$$h_0 = 1.2732395$$

$$h_1 = 0.2122066$$

$$h_2 = 0.0530516$$

Thus $T(t') = \dfrac{dk_2(t')}{dt'} = \dfrac{1}{4}\left\{\dfrac{h_0}{\sqrt{\sigma}} - 3h_1\sqrt{\sigma} + 5h_2(\sigma)^{\frac{3}{2}} - \cdots\right\}$

and $\displaystyle\int_{-1}^{-.999} w(t')T(t')\,dt' = \frac{h_0}{4}\int_{-1}^{-.999}\frac{w(t')\,dt'}{\left(\frac{t'+1}{2}\right)^{\frac{1}{2}}} - \frac{3h_1}{4}\int_{-1}^{-.999}w(t')\left(\frac{t'+1}{2}\right)^{\frac{1}{2}}dt' + \frac{5h_2}{4}\int_{-1}^{-.999}w(t')\left(\frac{t'+1}{2}\right)^{\frac{3}{2}}dt'$

now $w(t')$ can be considered constant over the interval -1 to $-.999$

$$\therefore \int_{-1}^{-.999} w(t')T(t')\,dt' = h_0 w\left(\frac{t'+1}{2}\right)^{\frac{1}{2}}\Bigg]_{-1}^{-.999} - h_1 w\left(\frac{t'+1}{2}\right)^{\frac{3}{2}}\Bigg]_{-1}^{-.999}$$
$$+ h_2 w\left(\frac{t'+1}{2}\right)^{\frac{5}{2}}\Bigg]_{-1}^{-.999} - \cdots$$

$$= W(-1) \left\{ \frac{5^{\frac{1}{2}} h_0}{10^2} - \frac{5^{\frac{3}{2}} h_1}{10^6} + \frac{5^{\frac{5}{2}} h_2}{10^{10}} - \cdots \right\}$$

$$\doteq .02846 \; W(-1)$$

The use of (17a) involves calculation of $\frac{dw}{d\xi}$, but avoids integration near a singularity. The minus sign before the integral is balanced by the negative slope of the velocity defect.

TABLE OF FUNCTIONS $k_2(t')$ and $T(t')$

t'	$k_2(t')$	$T(t')$	t'	$k_2(t')$	$T(t')$
-1	0	∞			
-.9999	.009003	-	-.962	.174950	2.289
-.9998	.012732	-	-.961	.177220	2.257
-.9997	.015593	26.54	-.960	.179464	2.232
-.9996	.018006	22.52	-.959	.181683	2.200
-.9995	.020130	20.11	-.958	.183863	2.174
-.9994	.022051	18.37	-.957	.186030	2.148
-.9993	.023818	17.02	-.956	.188158	2.122
-.9992	.025463	15.91	-.955	.190274	2.103
-.9991	.027007	15.00	-.954	.192364	2.077
-.9990	.028468	14.23	-.953	.194428	2.051
-.9989	.029857	13.57	-.952	.196466	2.026
-.9988	.031185	12.99	-.951	.198479	2.006
-.9987	.032458	12.48	-.950	.200478	1.993
-.9986	.033683	12.03	-.94	.21943	1.809
-.9985	.034864	11.62	-.93	.23682	1.673
-.9984	.036008	11.26	-.92	.25297	1.561
-.9983	.037116	10.92	-.91	.26809	1.468
-.9982	.038191	10.61	-.90	.28236	1.388
-.9981	.039238	10.33	-.89	.29590	1.320
-.9980	.040257	10.06	-.88	.30879	1.261
-.997	.049300	8.204	-.87	.32115	1.209
-.996	.056920	7.115	-.86	.33300	1.163
-.995	.063635	6.358	-.85	.34441	1.121
-.994	.069700	5.801	-.84	.35542	1.082
-.993	.075280	5.368	-.83	.36606	1.048
-.992	.080466	5.022	-.82	.37637	1.016
-.991	.085345	4.739	-.81	.38637	.986
-.990	.089956	4.496	-.80	.39608	.9582
-.989	.094337	4.286	-.6	.55132	.6458
-.988	.098527	4.100	-.4	.66490	.5036
-.987	.102538	3.940	-.2	.75635	.4167
-.986	.106408	3.794	0	.83339	.3567
-.985	.110125	3.660	.2	.90007	.3118
-.984	.113727	3.551	.4	.95884	.2769
-.983	.117227	3.442	.6	1.01131	.2487
-.982	.120611	3.340	.8	1.05862	.2252
-.981	.123907	3.250	1.0	1.10162	.2053
-.980	.127112	3.167	1.5	1.1942	.1668
-.979	.130241	3.090	2.0	1.2703	.1390
-.978	.133293	3.020	2.5	1.3344	.1180
-.977	.136281	2.950	3.0	1.3891	.1014
-.976	.139192	2.886	3.5	1.4364	.0882
-.975	.142052	2.834	4.0	1.4777	.0773
-.974	.144861	2.777	4.5	1.5140	.0684
-.973	.147606	2.719	5.0	1.5463	.0608
-.972	.150299	2.674	7.5	1.6642	.0366
-.971	.152954	2.623	10	1.7382	.0239
-.970	.155545	2.578	20	1.8698	.0069
-.969	.158110	2.540	30	1.9167	.0029
-.968	.160624	2.495	40	1.9397	---
-.967	.163100	2.456	50	1.9530	---
-.966	.165537	2.424	100	1.97800	---
-.965	.167948	2.386	500	1.995898	---
-.964	.170308	2.347	1000	1.997972	---
-.963	.172642	2.321	∞	2.000000	0

APPENDIX 3   SÖHNGEN'S INVERSION FORMULA FOR SEMI-INFINITE PLATE

Söhngen's inversion formula for a blade of chord $2a$ (Ref. (14)) is

$$\gamma(x) = \frac{2}{\pi} \sqrt{\frac{a-x}{a+x}} \oint_{-a}^{a} \sqrt{\frac{a+\xi}{a-\xi}} \; \frac{v(\xi)}{(x-\xi)} \, d\xi$$

Shifting the origin to the leading edge

$$\bar{x} = x + a \quad ; \quad \bar{\xi} = \xi + a$$

$$\gamma(\bar{x}) = \frac{2}{\pi} \sqrt{\frac{2a-\bar{x}}{\bar{x}}} \oint_{0}^{2a} \sqrt{\frac{\bar{\xi}}{2a-\bar{\xi}}} \; \frac{v(\bar{\xi})}{(\bar{x}-\bar{\xi})} \, d\bar{\xi}$$

$$= \frac{2}{\pi} \sqrt{\frac{1-\frac{\bar{x}}{2a}}{\bar{x}}} \oint_{0}^{2a} \sqrt{\frac{\bar{\xi}}{1-\frac{\bar{\xi}}{2a}}} \; \frac{v(\bar{\xi})}{\bar{x}-\bar{\xi}} \, d\bar{\xi}$$

and as $2a \longrightarrow \infty$

$$\gamma(\bar{x}) = \frac{2}{\pi} \frac{1}{\bar{x}^{\frac{1}{2}}} \oint_{0}^{\infty} \bar{\xi}^{\frac{1}{2}} \; \frac{v(\bar{\xi})}{(\bar{x}-\bar{\xi})} \, d\bar{\xi}$$

The integral does exist for as $2a \rightarrow \infty$, $v(\xi) \rightarrow 0$ since $v(\xi)$ is the velocity disturbance produced by the source or doublet and hence must vanish

as $\xi \longrightarrow \infty$

Thus dropping the "bar" notation

$$\gamma(x) = \frac{2}{\pi} \frac{1}{x^{\frac{1}{2}}} \oint_{0}^{\infty} \frac{\xi^{\frac{1}{2}} v(\xi)}{(x-\xi)} \, d\xi$$

APPENDIX 4   VOLTAGE ATTENUATION IN TRANSDUCER EQUIVALENT CIRCUIT

Consider the equivalent circuit of the transducer in the following sketch
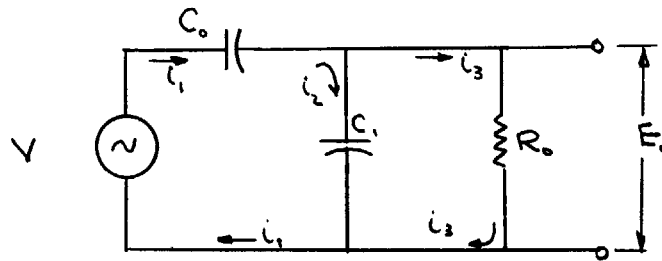
Applying Kirchoff's law:

$$E_0 = i_3 R_0 \tag{i}$$

$$i_1 = i_2 + i_3 \tag{ii}$$

$$V - E_0 = i_1 X_{c_0} \quad \text{where } X_{c_0} = \frac{1}{j\omega c_0} \tag{iii}$$

$$i_2 X_{c_1} = i_3 R_0 \tag{iv}$$

substituting (iii) and (iv) into (ii)

$$i_3 = \frac{(V - E_0)}{X_{c_0}} \; \frac{X_{c_1}}{R_0 + X_{c_1}} \tag{v}$$

substituting (v) into (i)

$$\frac{E_0}{V} = \frac{R_0 X_{c_1}}{R_0 X_{c_0} + X_{c_1} X_{c_0} + R_0 X_{c_1}}$$

ie.

$$\frac{E_0}{V} = \frac{\dfrac{R_0}{j\omega c_1}}{\dfrac{R_0}{j\omega c_0} + \dfrac{1}{j\omega c_0 j\omega c_1} + \dfrac{R_0}{j\omega c_1}}$$

which eventually comes down to

$$\frac{E_0}{V} = \frac{R_0 \omega c_0 \left\{ j + R_0 \omega (c_1 + c_0) \right\}}{1 + \left\{ R_0 \omega (c_1 + c_0) \right\}^2}$$

whence

$$\frac{E_0}{V} = \frac{R_0 \omega c_0 \sqrt{1 + \left(R_0 \omega (c_1 + c_0) \right)^2}}{1 + \left[R_0 \omega (c_1 + c_0) \right]^2}$$

rearranging and substituting $\omega = 2\pi f$

$$\frac{E_0}{V} = \frac{c_0}{c_1 + c_0} \cdot \frac{2\pi f (c_1 + c_0) R_0}{\sqrt{1 + \left\{ 2\pi f (c_1 + c_0) R_0 \right\}^2}}$$

APPENDIX 5   CALCULATION OF WAKE ARRIVAL TIME
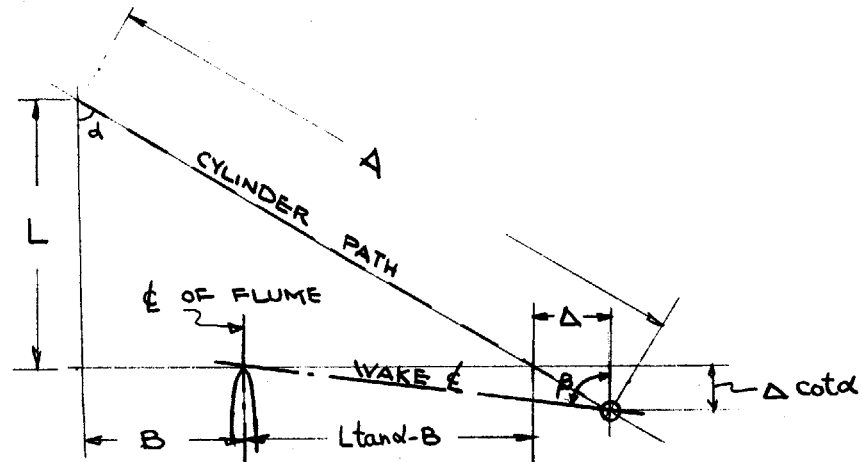
Assume that the wake reaches the blade leading edge when the cylinder has travelled a distance A.

$$A \sin \alpha = L \tan \alpha + \Delta$$

$$\therefore \quad A = \frac{L}{\cos \alpha} + \frac{\Delta}{\sin \alpha}$$

where Δ is found as follows

$$\frac{L \tan \alpha - B + \Delta}{\Delta \cot \alpha} = \tan \beta$$

$$\therefore \quad \Delta = \frac{L \tan \alpha - B}{(\tan \beta / \tan \alpha) - 1}$$

$\left(\text{note that for } \beta = 90°, \quad \Delta = 0 \text{ and for } \beta > 90°, \quad \Delta \text{ is } < 0\right)$

β was determined from

$$\tan \beta = \frac{V \sin \alpha}{U - V \cos \alpha}$$

where U is the free stream velocity

and V is the actual cylinder velocity

Measured values for L, B and α were

$$L = 21.25''$$

$$B = 11.31''$$

$$\alpha = 60°$$

It can also be shown that the wake reaching the blade is a distance z behind the cylinder where

$$z = \frac{L \tan \alpha - B}{\sin \beta - \cos \beta \tan \alpha}$$
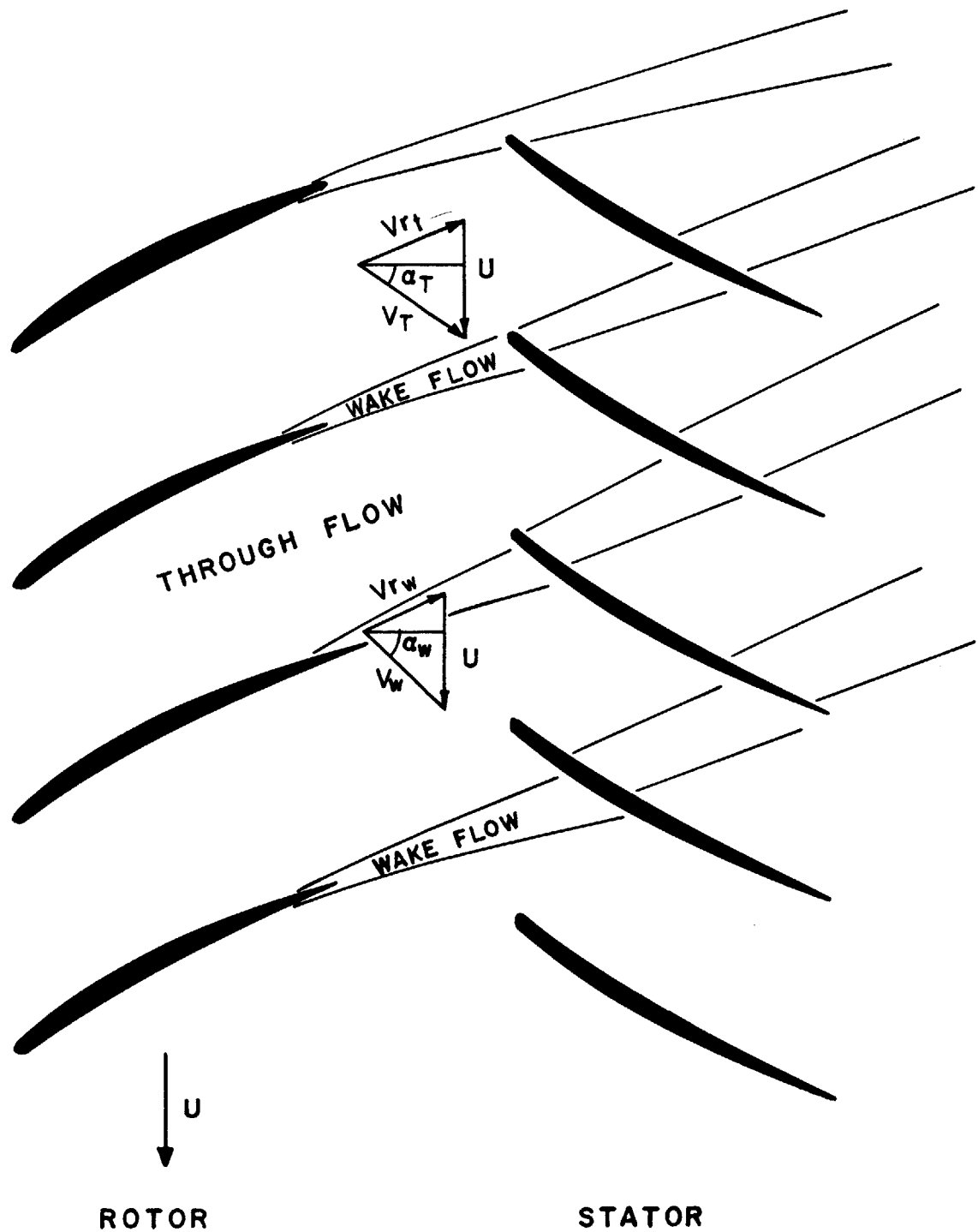
STATOR BLADES EXPERIENCING UNSTEADY FLOW
DUE TO MOTION OF ROTOR RELATIVE TO STATOR

FIG. I

MODEL OF WAKE AS A JET
APPROACHING FLAT PLATE
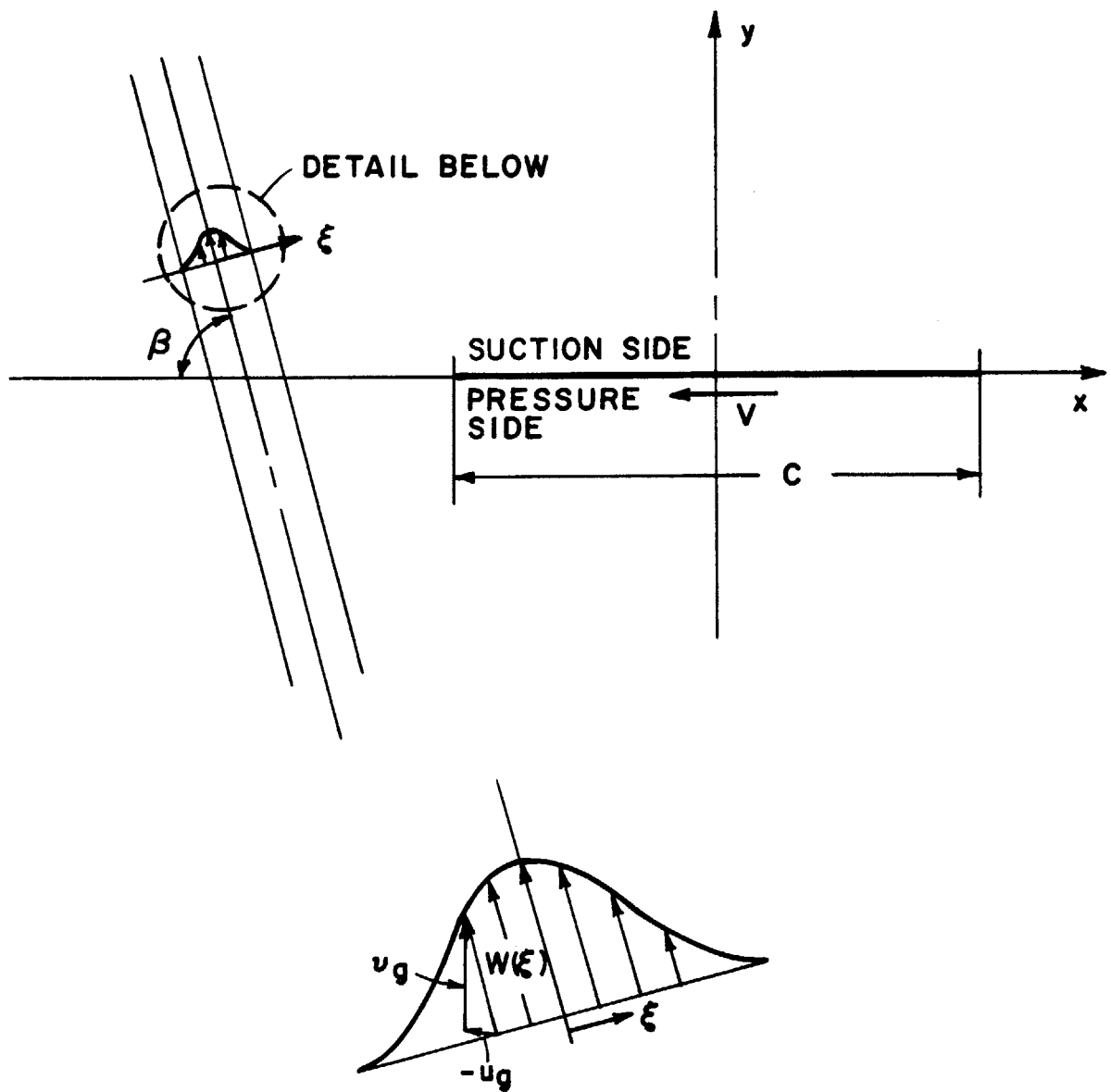
DETAIL OF VELOCITY DEFECT

FIG. 2

$P > P_{THIN\ AIRFOIL}$

COMPRESSOR: $\dfrac{\text{SUCTION SIDE}}{\begin{array}{l}\text{PRESSURE}\\ \text{SIDE}\end{array}}$ $\dfrac{\text{PRESSURE SIDE}}{\text{SUCTION SIDE}}$:TURBINE
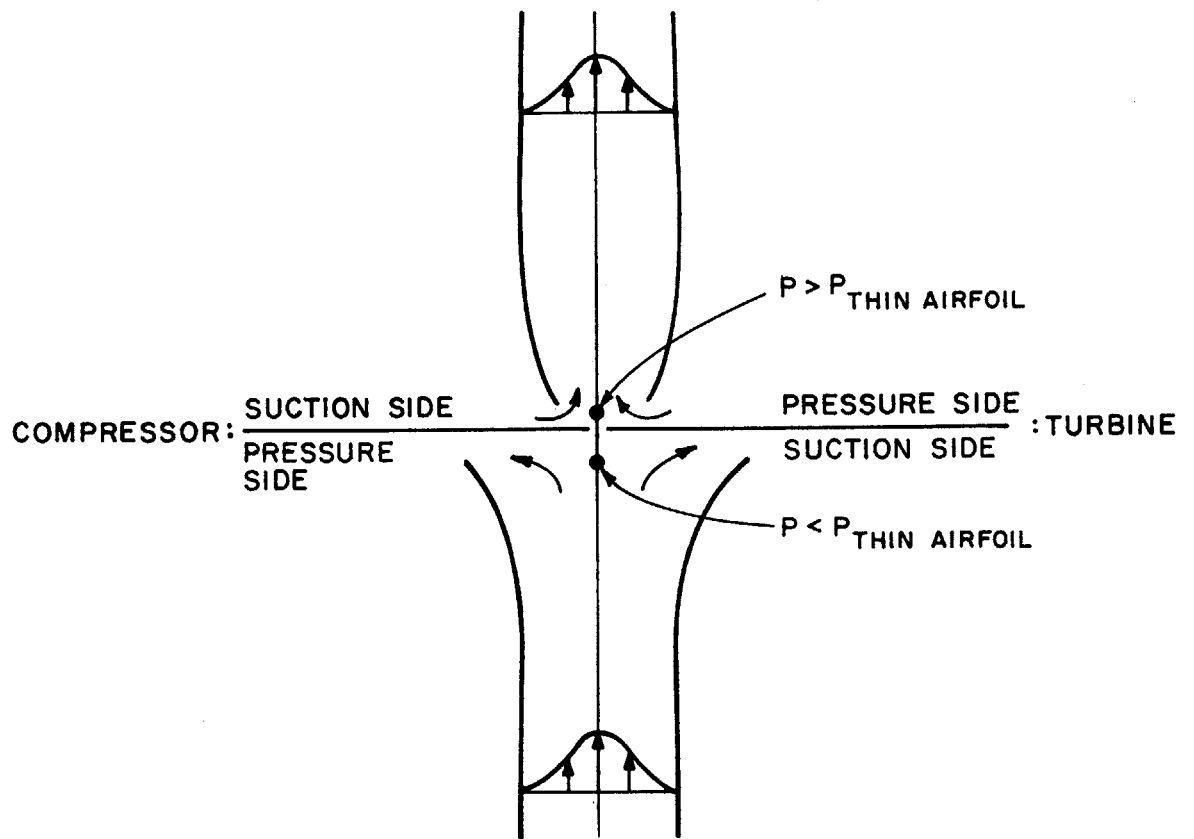
$P < P_{THIN\ AIRFOIL}$

FIG. 3   DISTORTED   WAKE   ON   BLADE
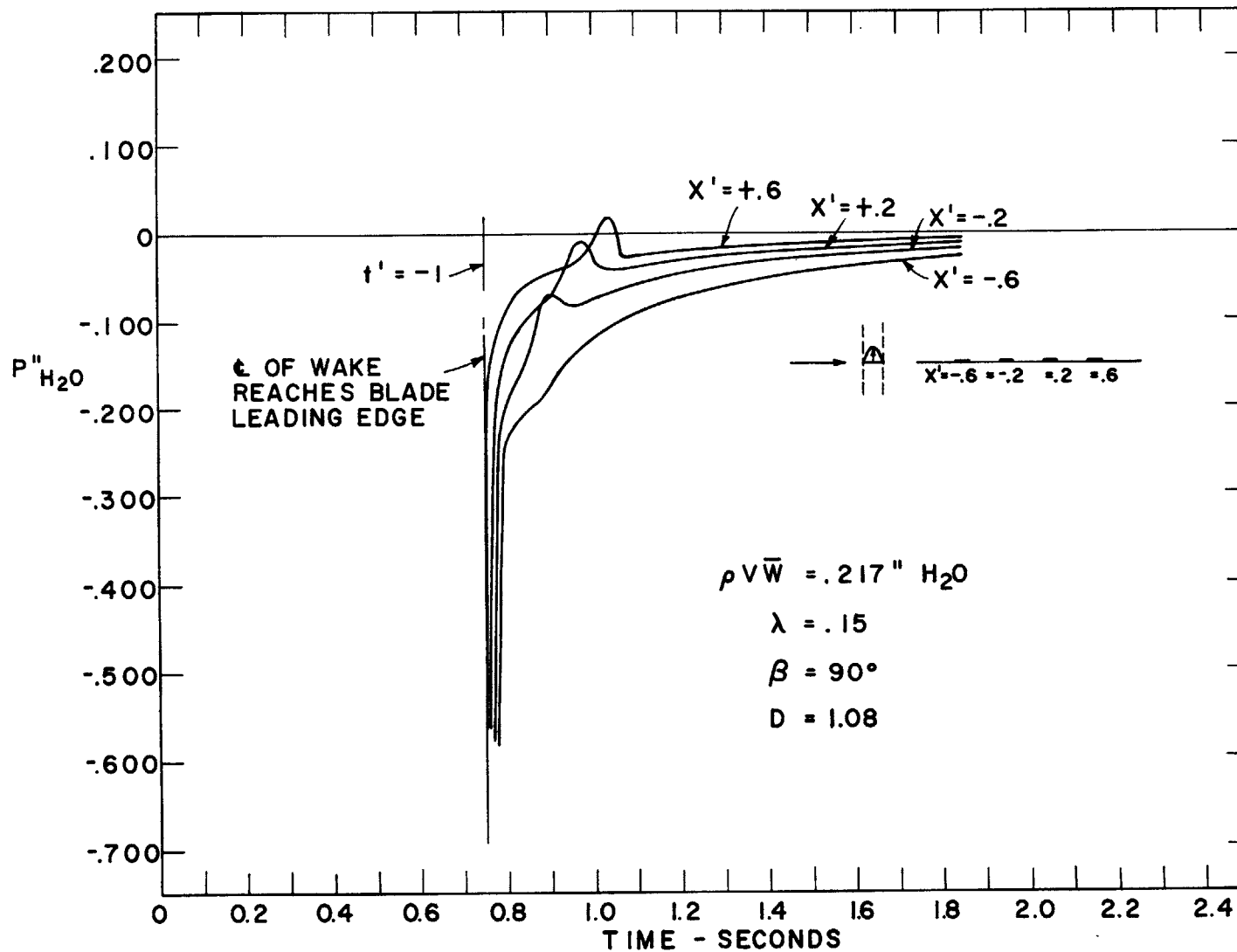
FIG. 4 THIN AIRFOIL SOLUTION INCORPORATING WAKE DISTORTION EFFECT. [Ref. (8)]
SUCTION SIDE.

FIG. 5

MOTOR

STEM PROTECTING
BOX

U →

PLATFORM →

BLADE BOX

PRESSURE WAVE DAMPER

SLOTTED BOX

CYLINDER CARRIAGE
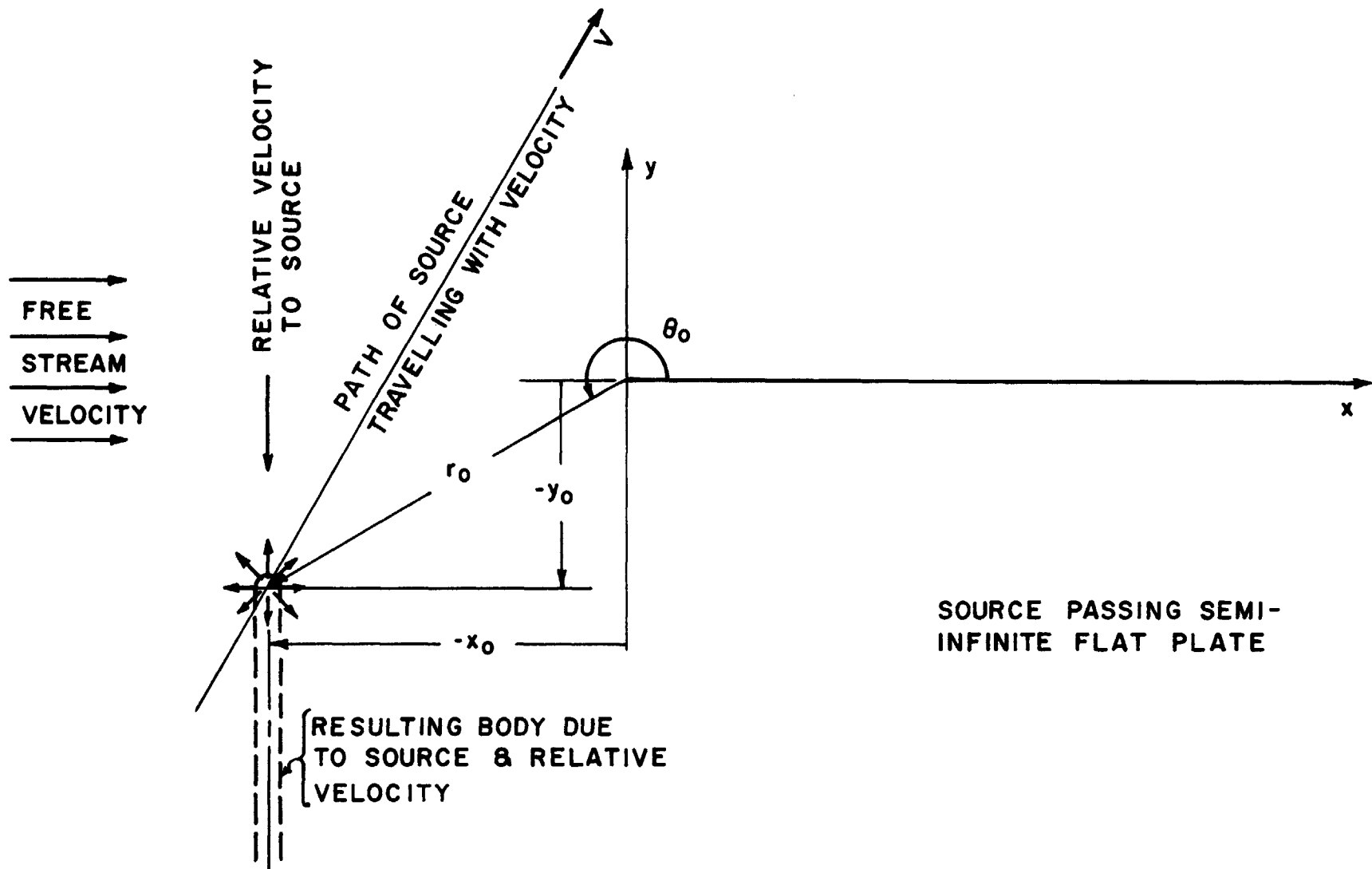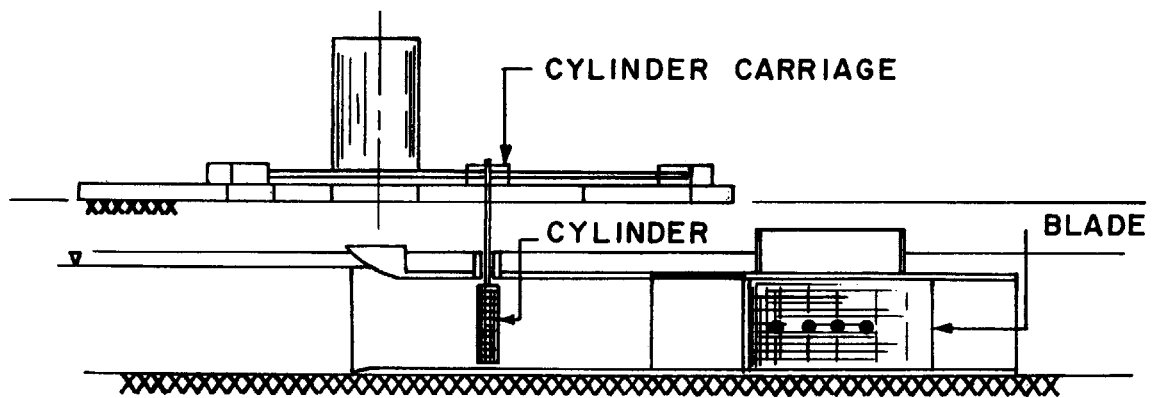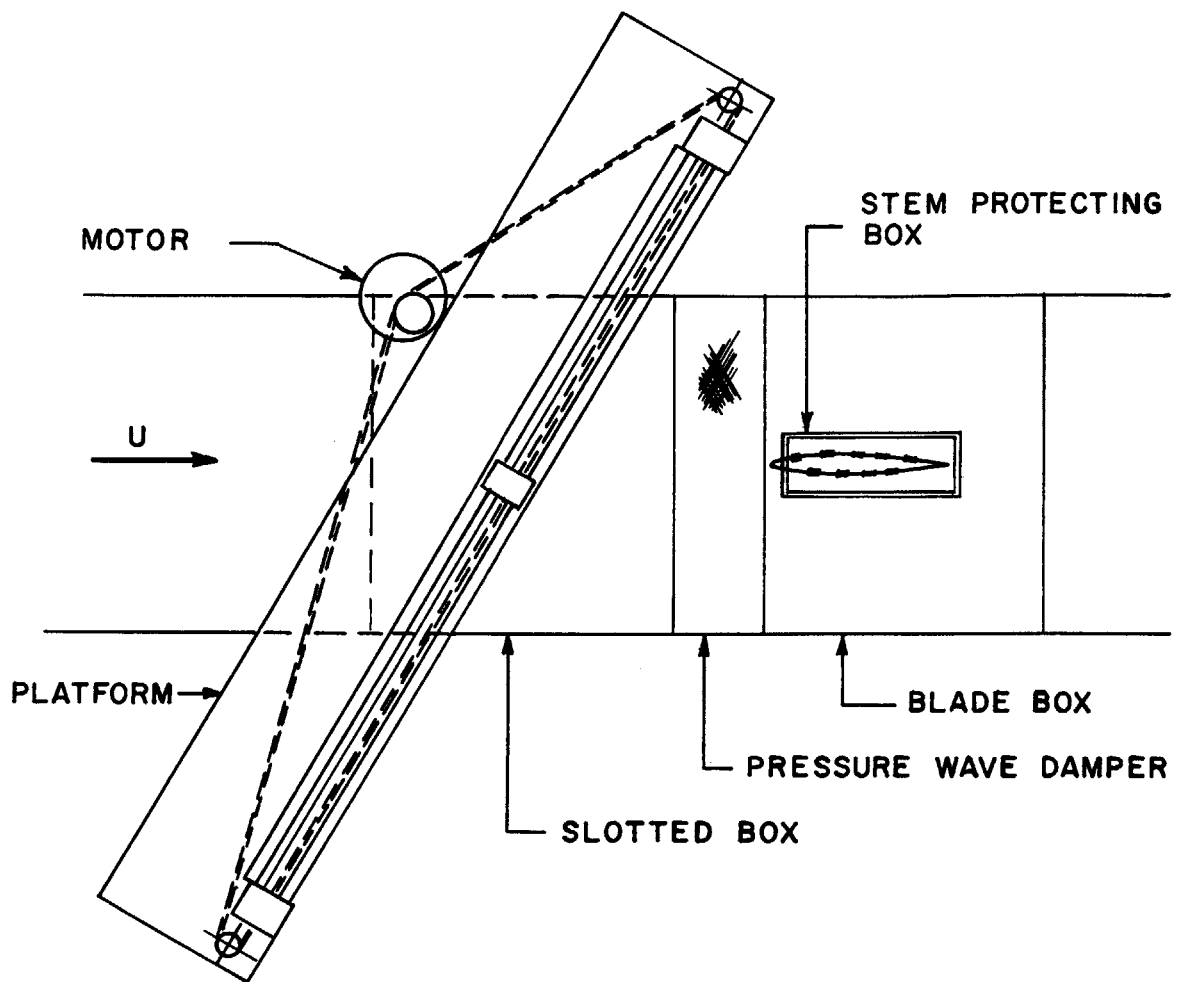
CYLINDER

BLADE

SCHEMATIC OF APPARATUS

FIG. 6
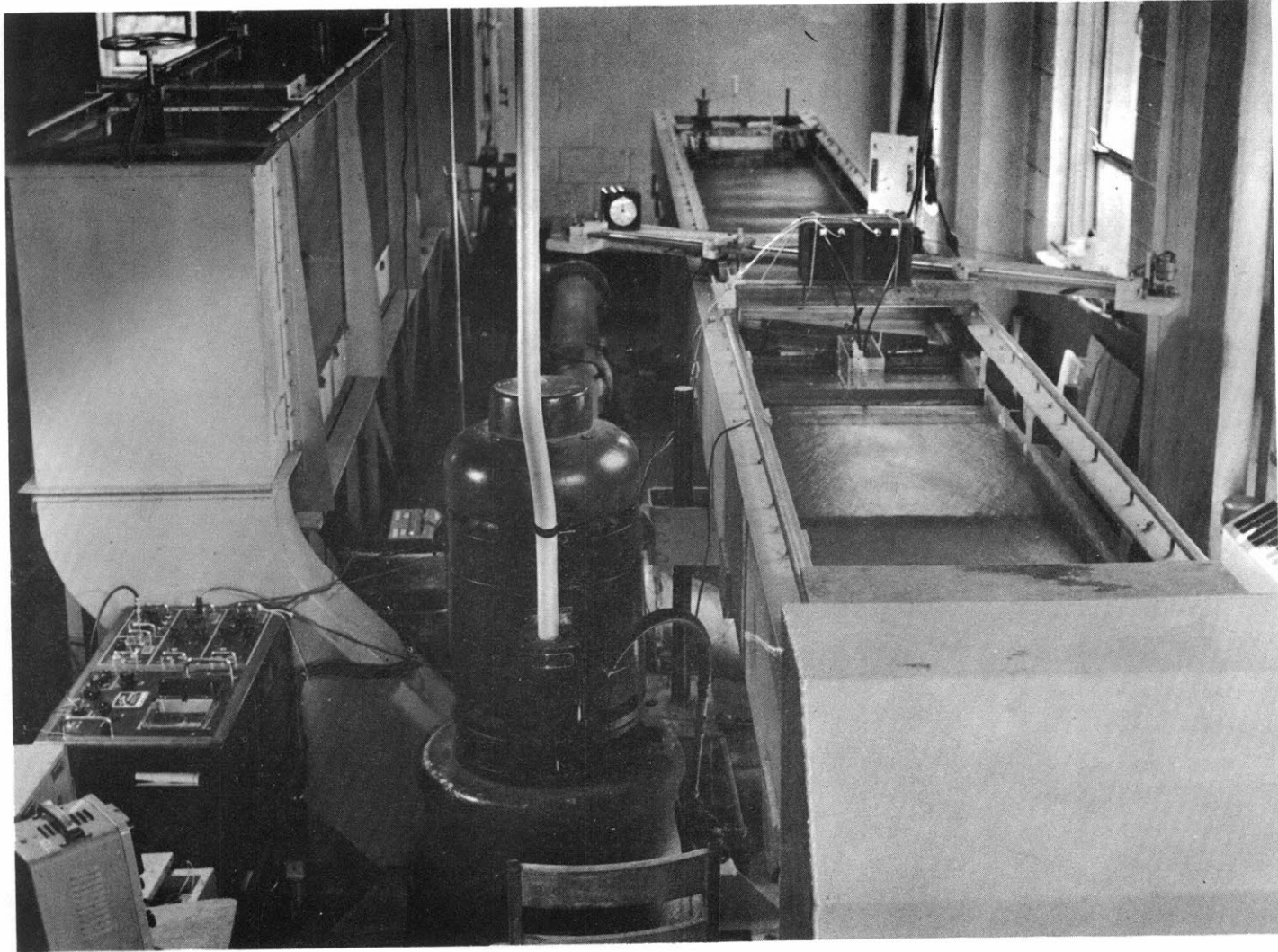
FIGURE 7. OVERALL VIEW OF APPARATUS
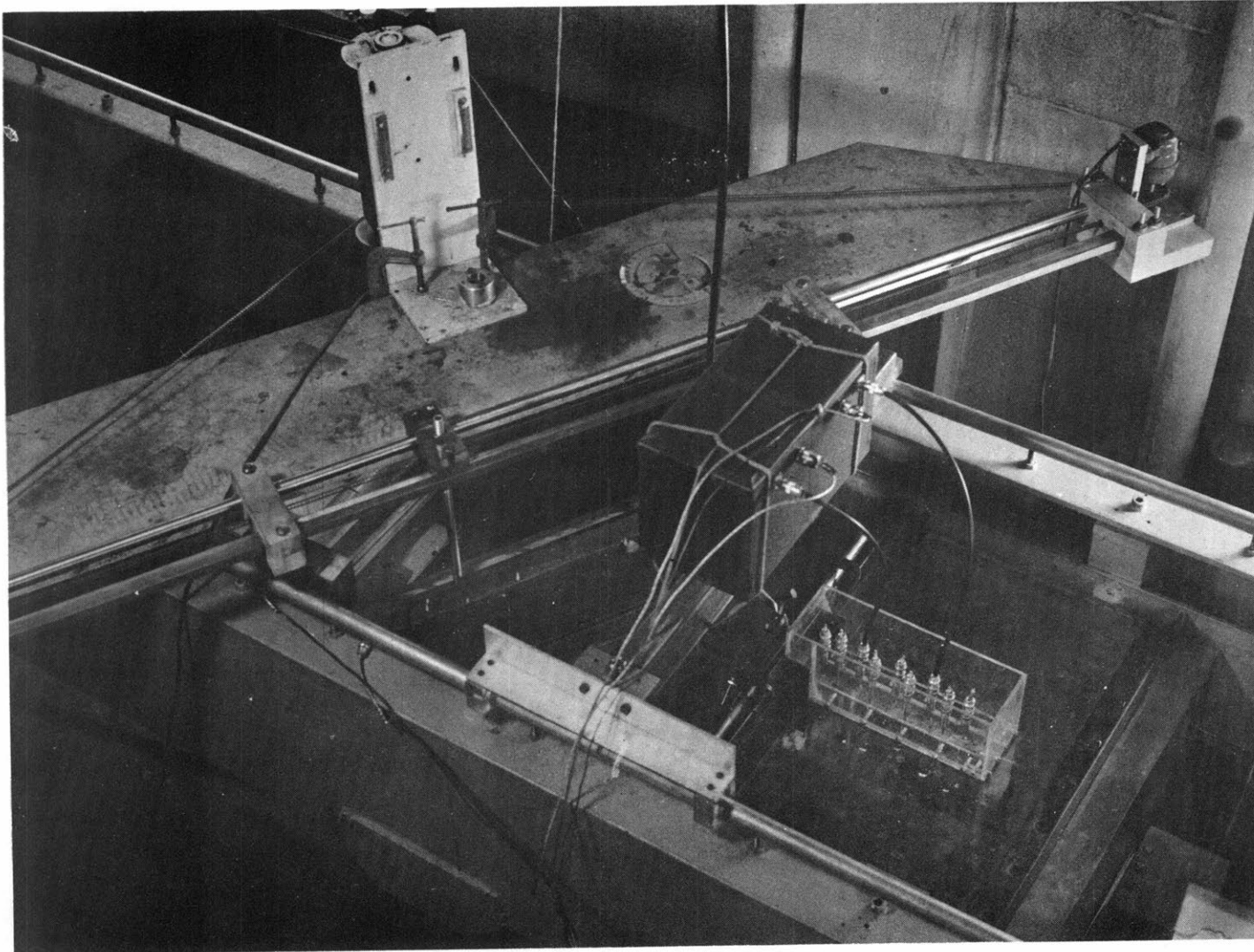
FIGURE 8.   VIEW OF TEST SECTION
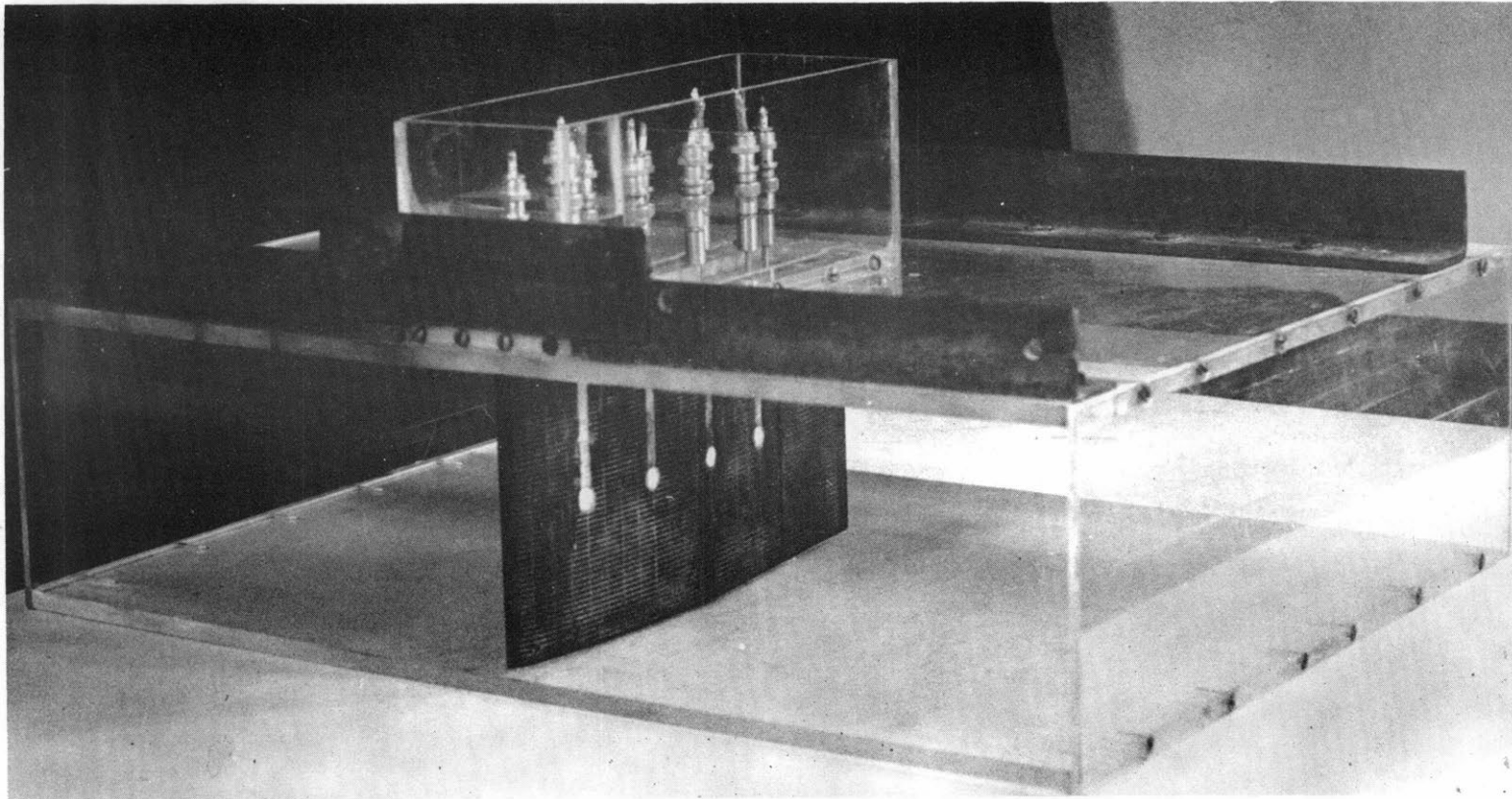
FIGURE 9.   BLADE BOX
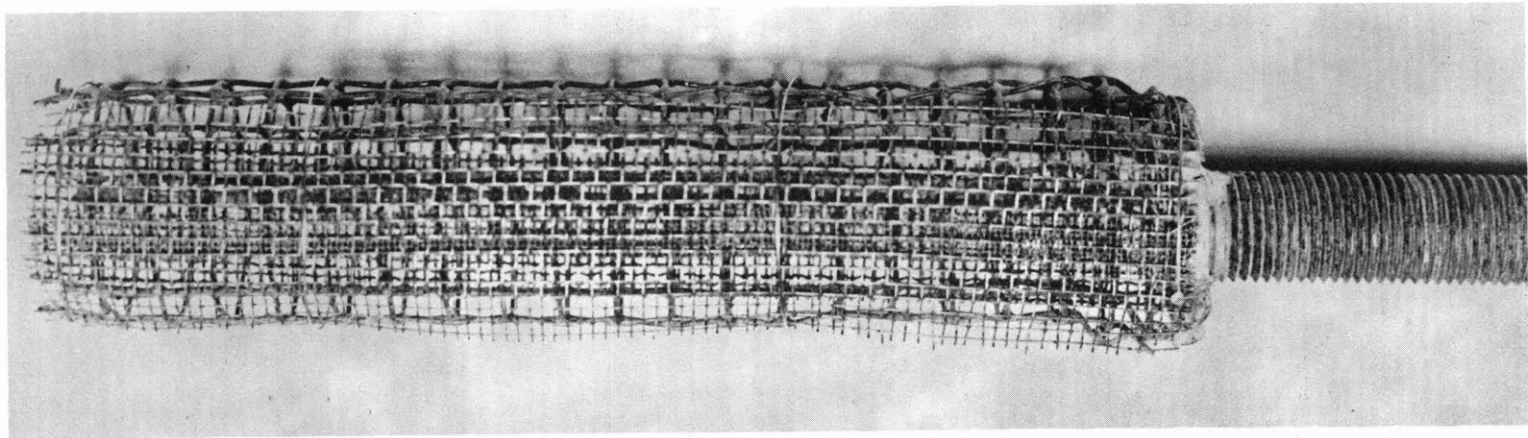
FIGURE 10. SCREEN CYLINDER

CERAMIC PRESSURE TRANSDUCER

+

0   .5   1.0

INCH
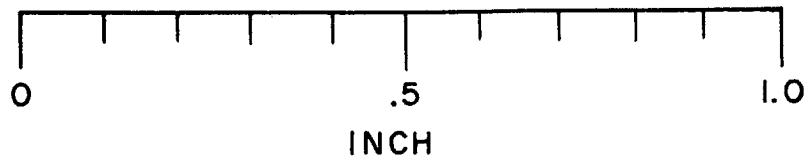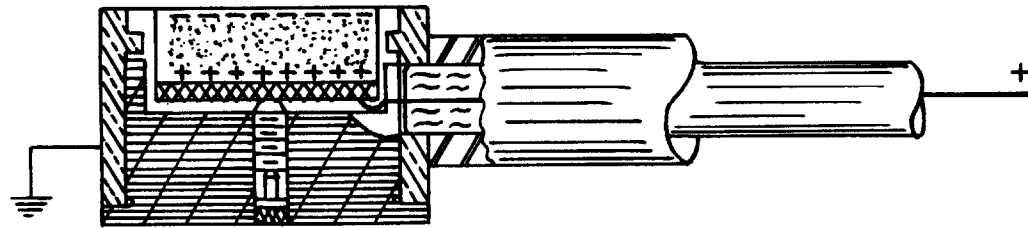
FIG. II
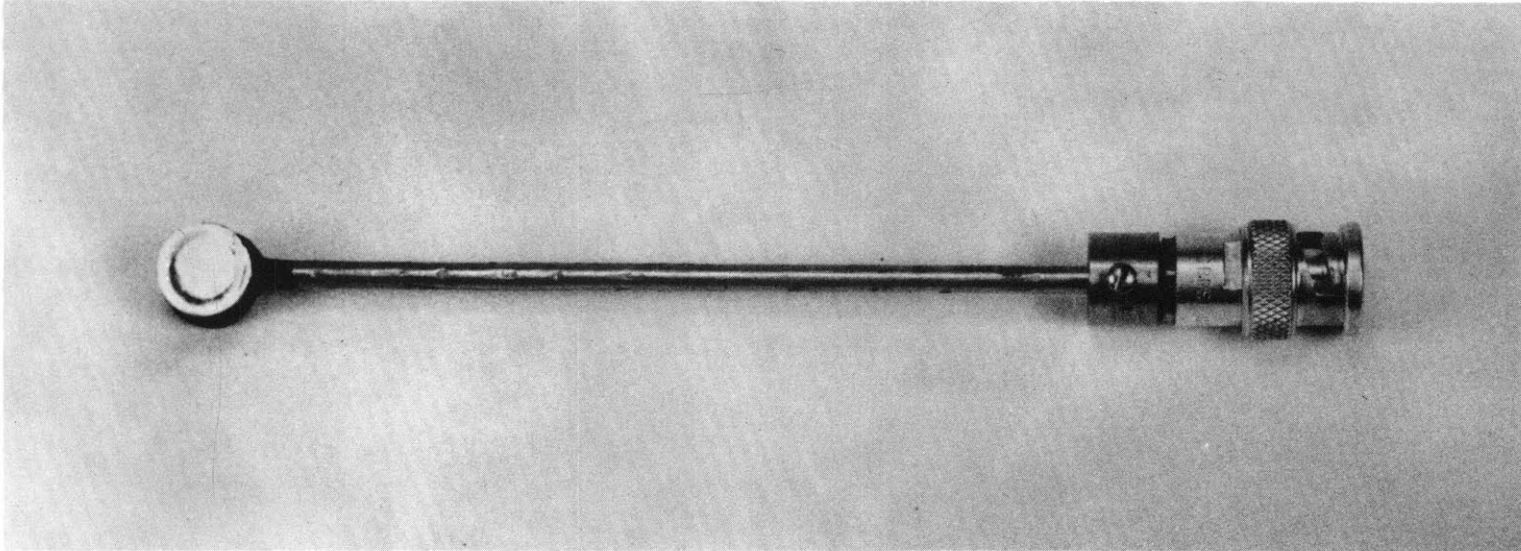
FIGURE 12.   PRESSURE TRANSDUCER
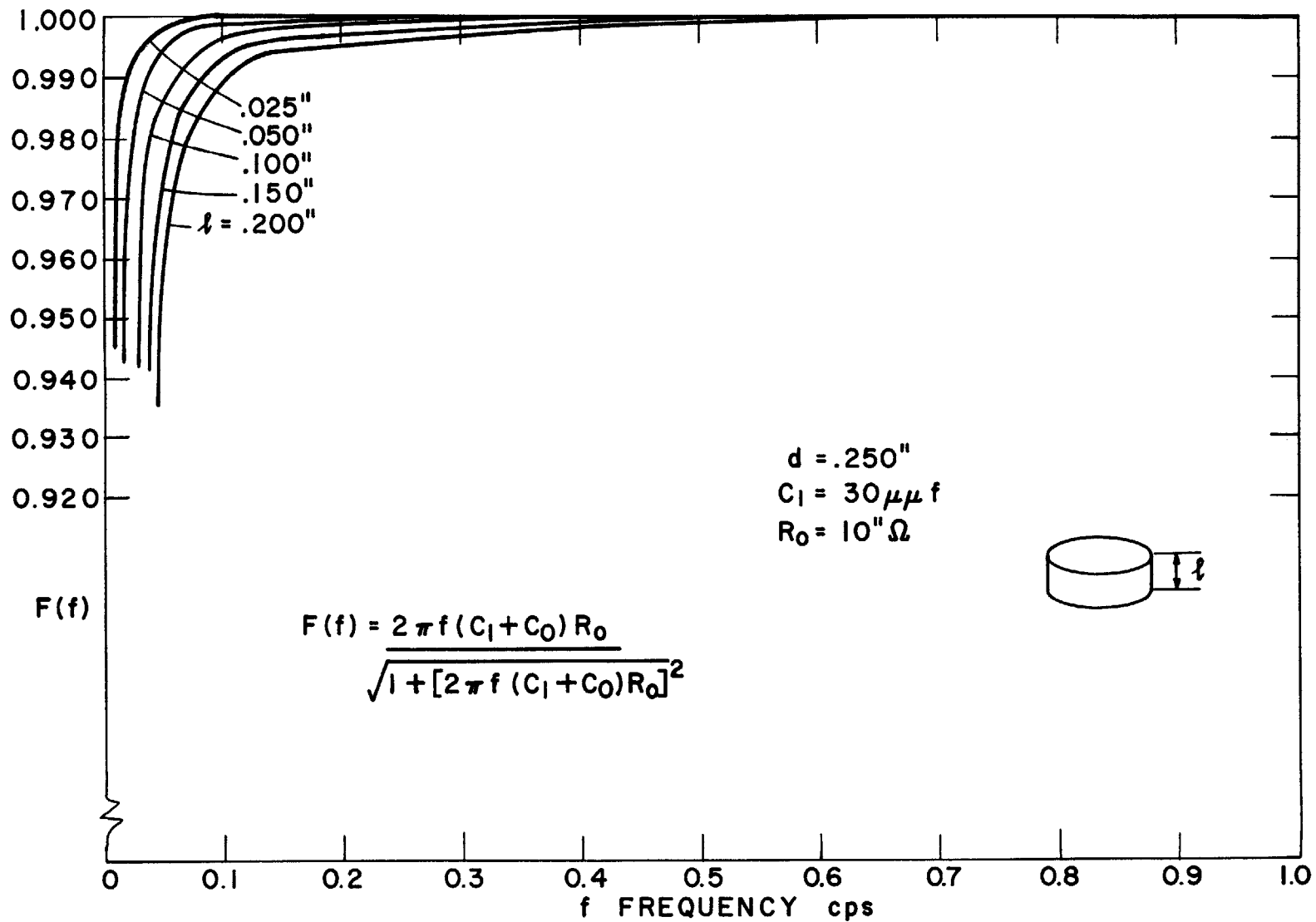
FIG. 13a F(f) VS FREQUENCY
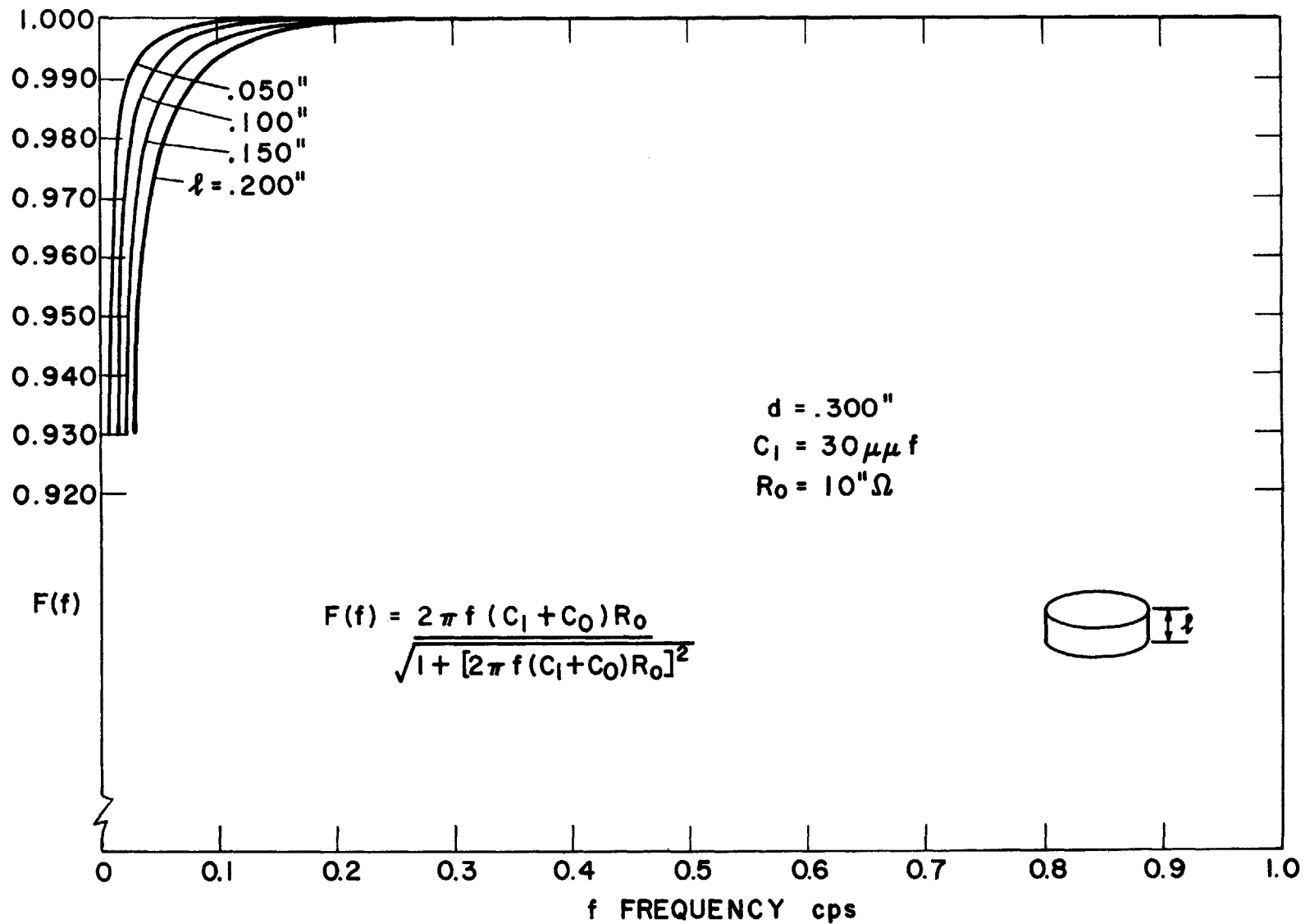
FIG. 13b F(f) VS FREQUENCY

$$\frac{E_0}{V} = \frac{C_0}{C_1 + C_0} \cdot F(f)$$

$d = .250"$

$R_0 = 10"\Omega$

$C_1 = 30\mu\mu f$

FIG. 14a

$$\frac{E_0}{V} = \frac{C_0}{C_I + C_O} \ F(f)$$

f > 1/4

1/10

1/20

f > 1/2

1/4

1/20

1/10

$\frac{E_0}{V}$

$E_0 \ mv/ " H_2O$

d = .300"

R_0 = 10" Ω

C_I = 30 μμf

DISC THICKNESS ℓ - INCHES

FIG. 14 b

CK 5886

50 K

+10.5 V

INPUT

OUTPUT

50 Ω

1.5 V

1 Meg

+7.5 V

150 K

100 K

1.3 Meg

-12 V
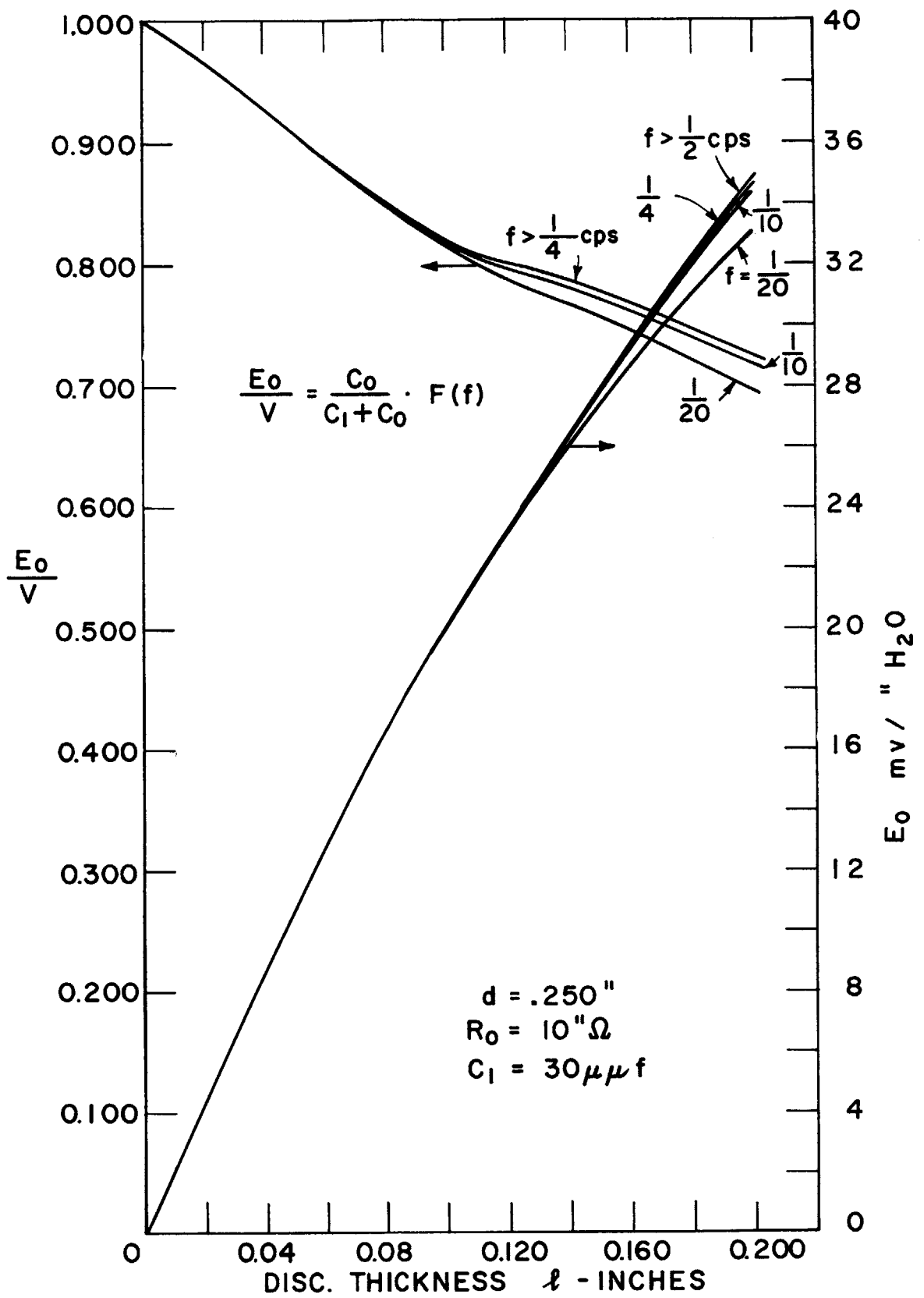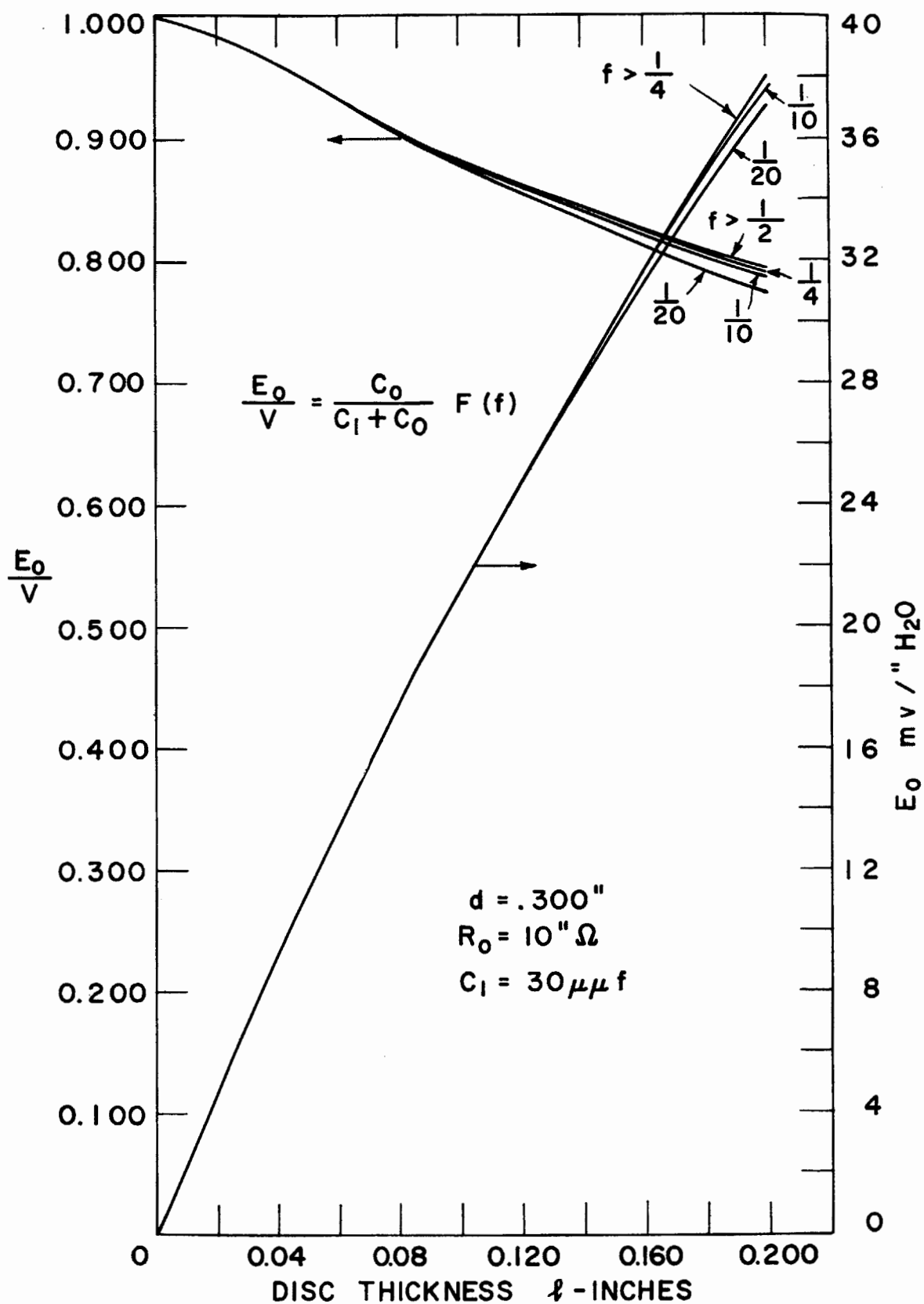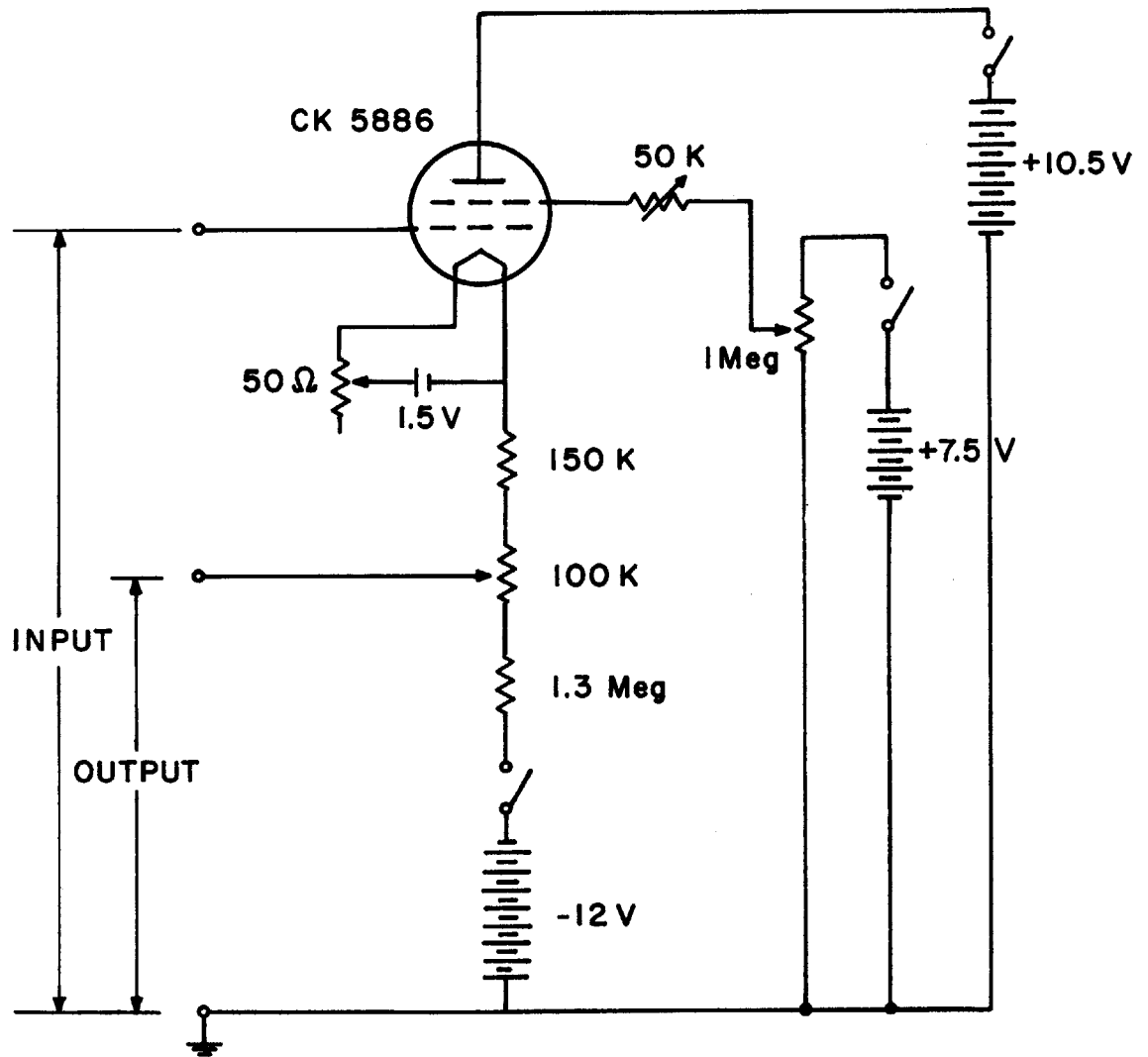
FIG. 15   ELECTROMETER   CIRCUIT   DIAGRAM
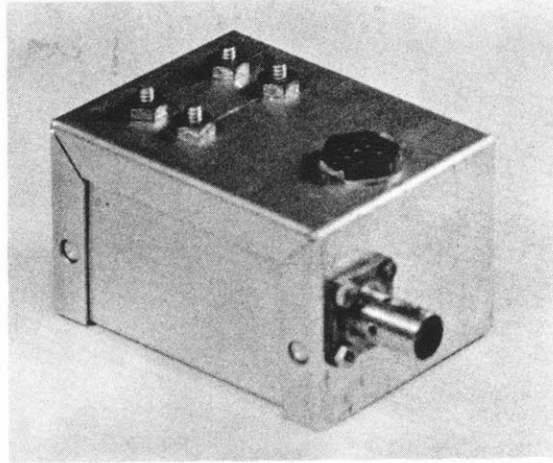
FIGURE 16.   ELECTROMETER BOX
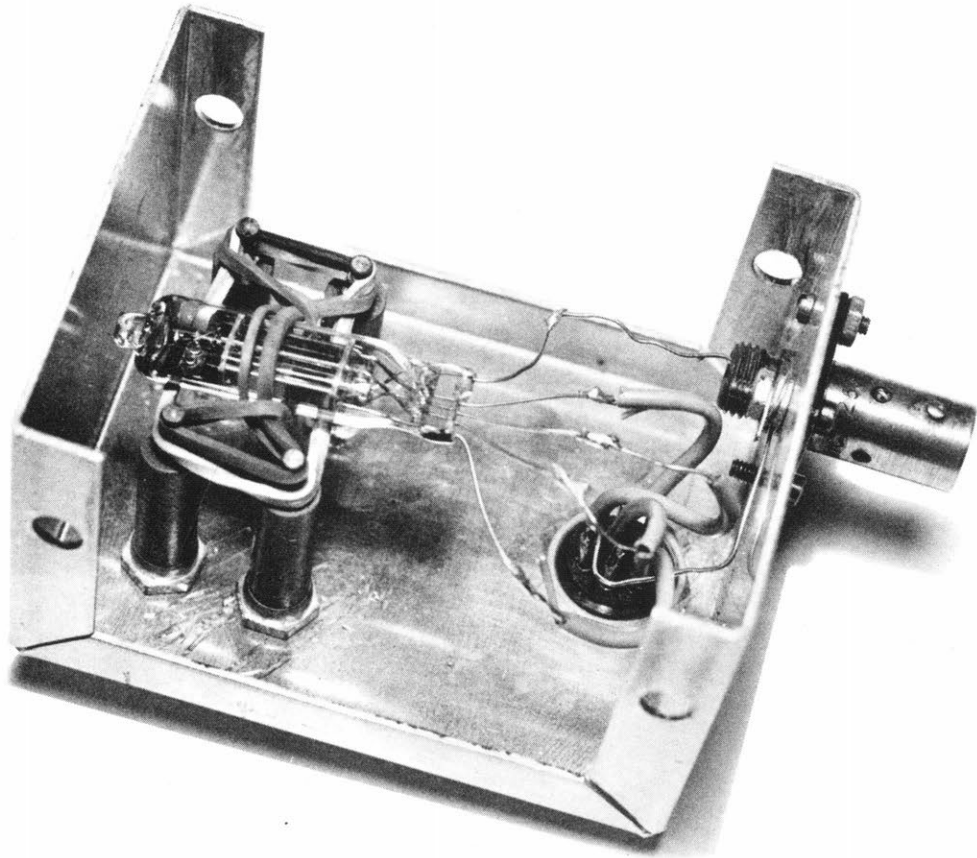
FIGURE 17.   ELECTROMETER TUBE

filament potentiometer

output potentiometer

screen grid potentiometer, coarse control

output jack

VTVM jack

screen grid potentiometer, fine control

connector to electrometer box

voltage selector
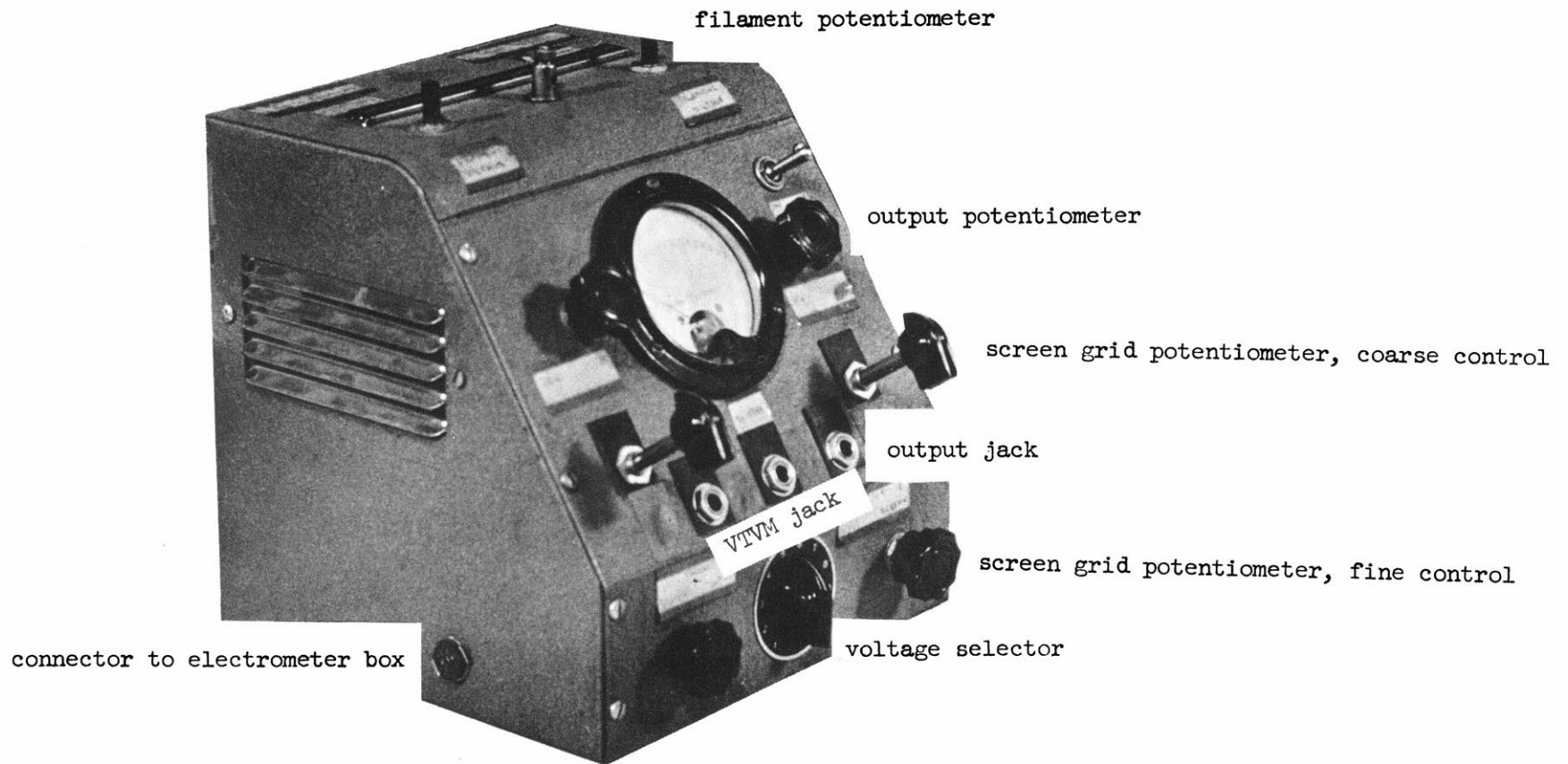
FIGURE 18. RESISTANCE BOX

FROM POWER SUPPLY   FROM POWER SUPPLY

+10.5V   +7.5V   -12V   0V   +1.5V   0 0   +1.5V   0 0   +10.5V   +7.5V   -12V   0V

CIRCUIT # 1   CIRCUIT # 2

50 Ω FILAMENT POT   50 Ω FILAMENT POT

TO ELECTROMETER   { D₁ A₁ E₁ H₁ B₁ }   150 KΩ   1.3 MΩ   150 KΩ   1.3 MΩ   { D₂ A₂ E₂ H₂ B₂ }   TO ELECTROMETER

50 K FINE CONTROL   1 MEG SCREEN POT   100 K OUTPUT POT   OUTPUT JACK   OUTPUT JACK   100 K OUTPUT POT   1 MEG SCREEN POT   50 K FINE CONTROL

ELECTROMETER LEADS

A : BLACK - TO +VE FILAMENT
B : BROWN - TO ELECTROMETER CASE
D : RED   - TO PLATE
E : ORANGE - TO -VE FILAMENT
H : YELLOW - TO SCREEN

TOP   BOTTOM   SELECTOR SWITCH

DC VOLT-METER   JACK TO V.T.V.M.

FIG. 19   SCHEMATIC OF RESISTANCE BOX
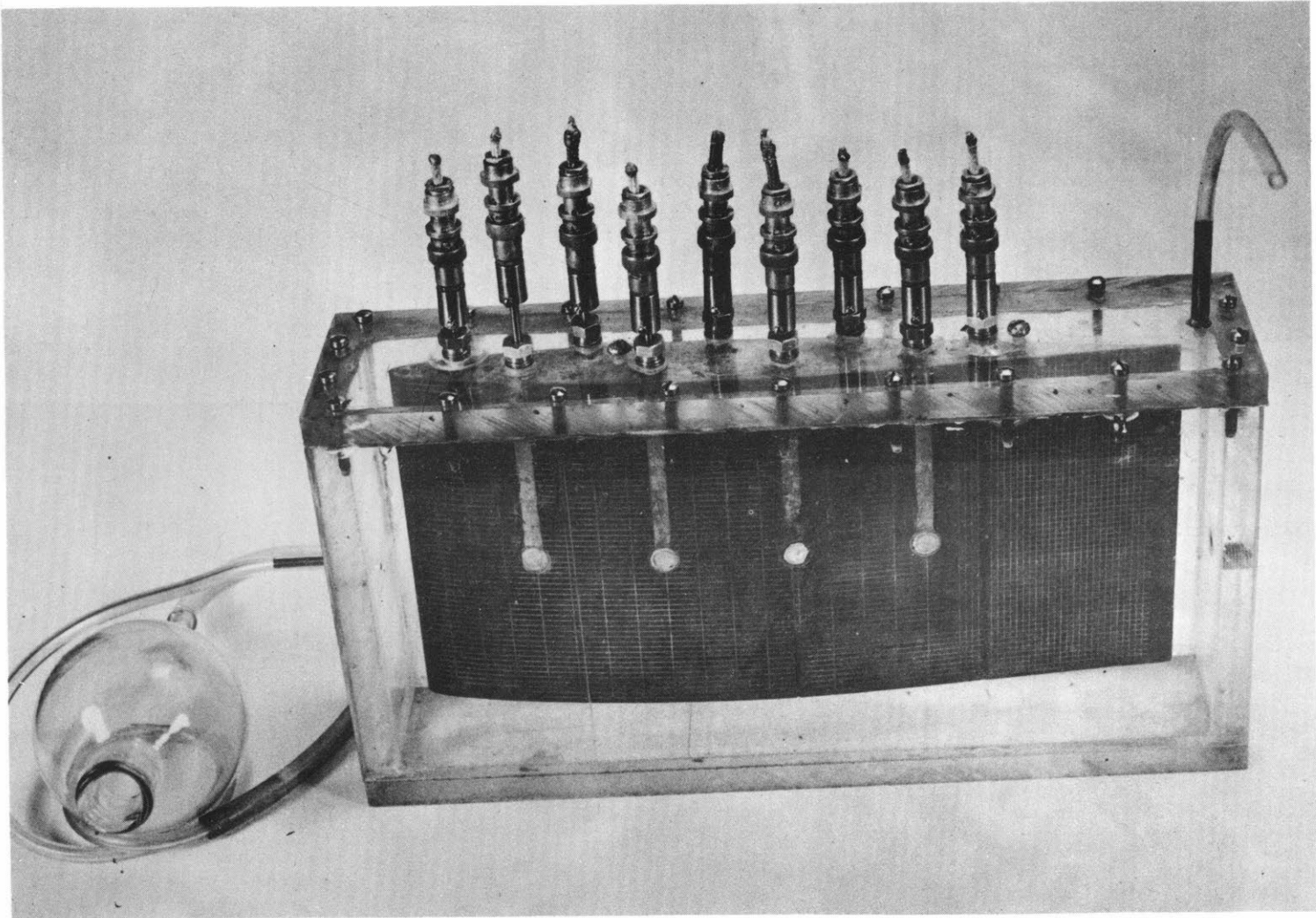
FIGURE 20. CALIBRATING BOX
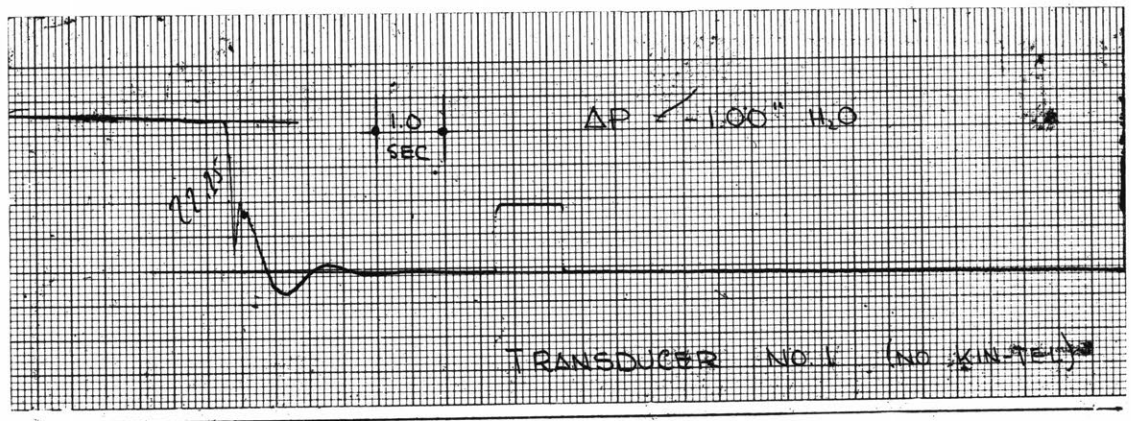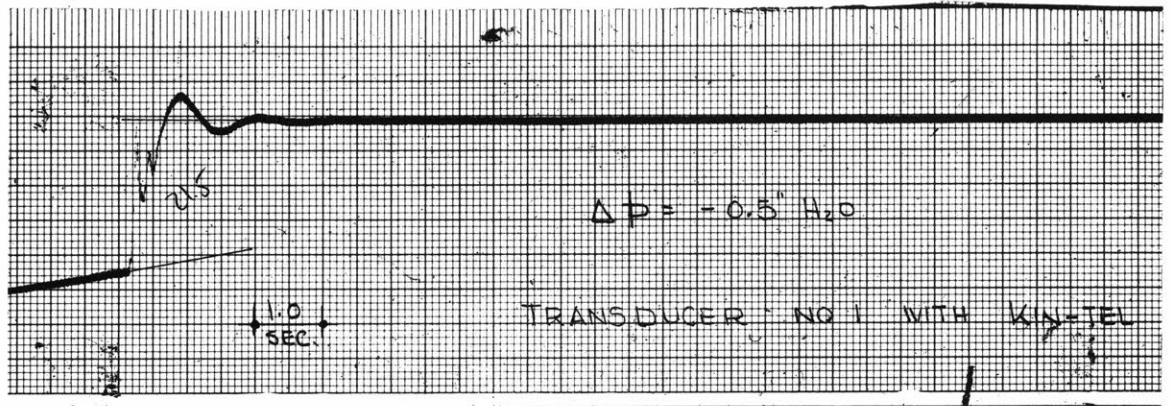
FIGURE 21. SAMPLE CALIBRATION TRACES

WAKE DATA

VELOCITY DEFECT (FT/SEC)

1.2
1.1
1.0 w
0.8
0.7
0.6
0.5 b$_0$
0.4
0.3
0.2
0.1

-.20   -.10   0   +.10   +.20

ξ -DISTANCE FROM WAKE $\math{C}$
(FT)
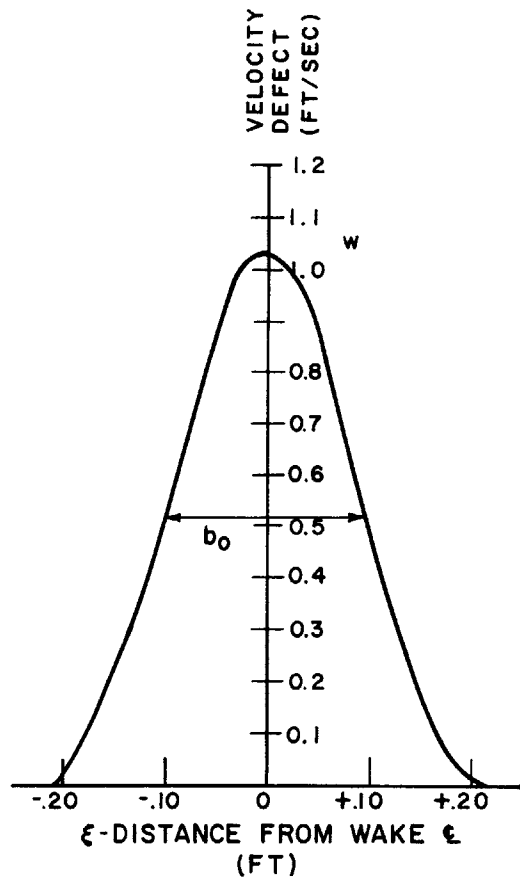
CYLINDER #1

w_{max}=1.03 FT/SEC

b_0 =.196 FT

$\overline{W} = \frac{1}{C} \int w(\xi) d\xi$ =.210 FT/SEC

(a)

VELOCITY DEFECT (FT/SEC)

1.2
1.1
1.0 w
0.8
0.7
0.6
0.5 b$_0$
0.4
0.3
0.2
0.1

-.20   -.10   0   +.10   +.20

ξ -DISTANCE FROM WAKE $\math{C}$
(FT)
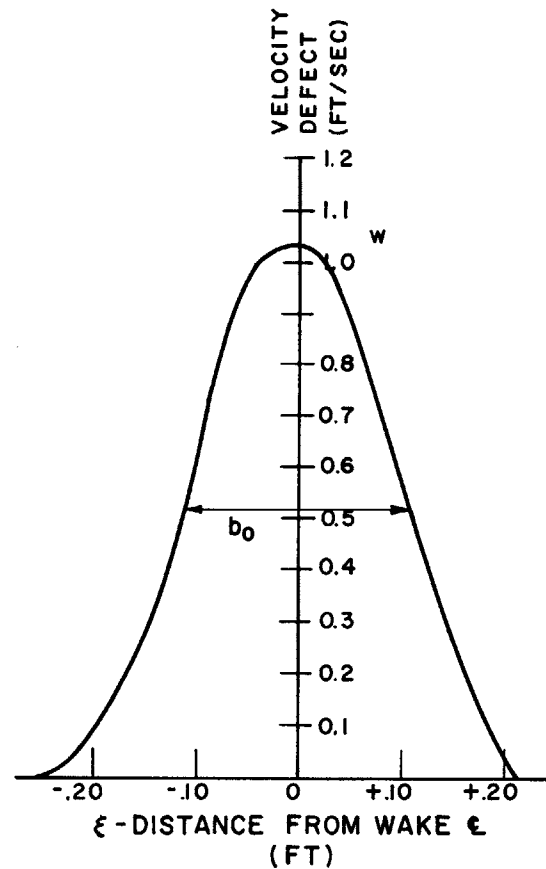
CYLINDER #5

w_{max}=1.03 FT/SEC

b_0 =.218 FT

$\overline{W} = \frac{1}{C} \int w(\xi) d\xi$ =.235 FT/SEC

(b)

FIG. 22
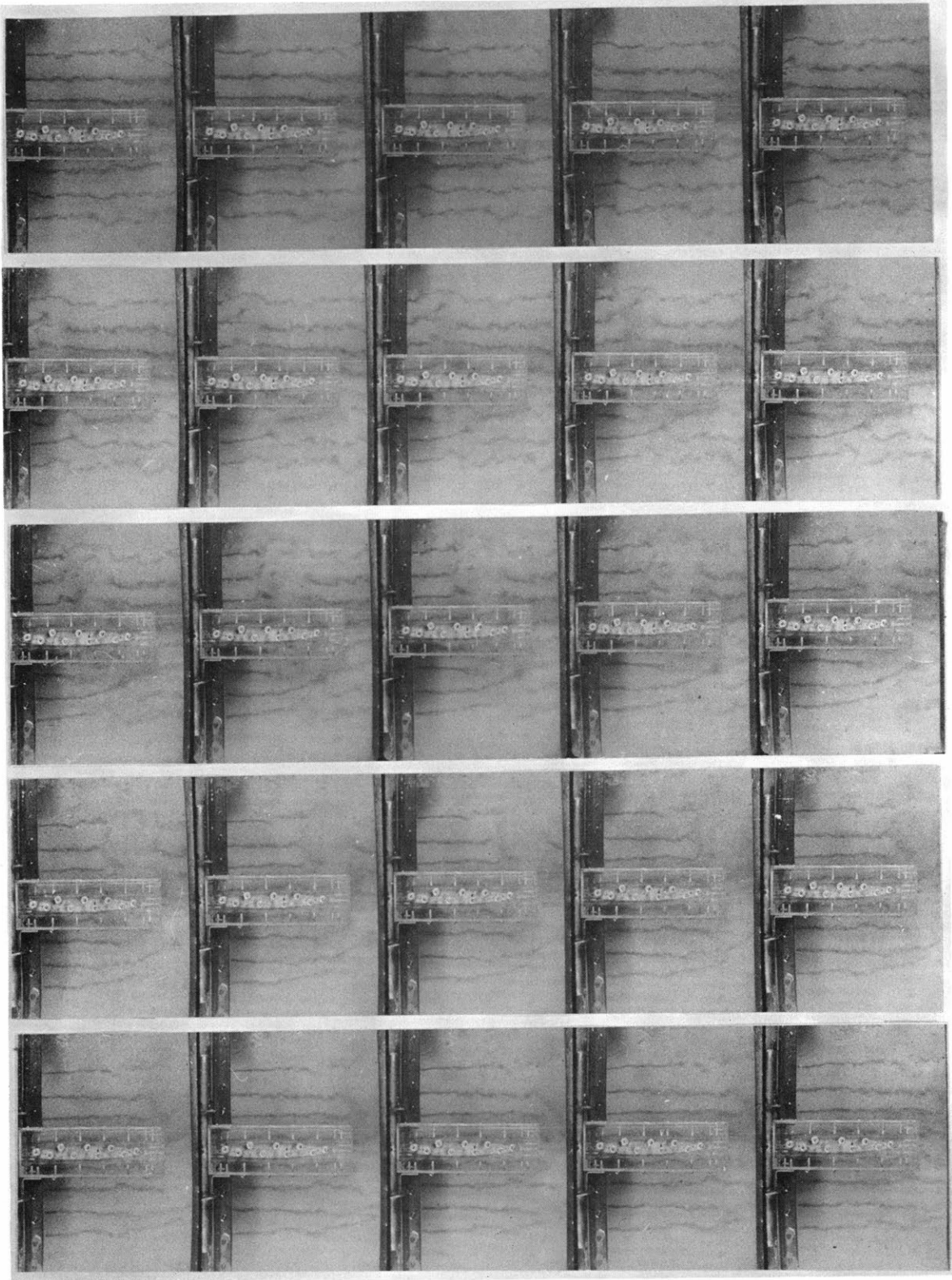
FIGURE 23a. SEQUENCE SHOWING WAKE GENERATED BY NO. 1 CYLINDER
PASSING OVER AIRFOIL. FREE STREAM VELOCITY = 2.77 ft/sec.
RELATIVE CYLINDER VELOCITY = 4.75 ft/sec. (SEQUENCE BEGINS
AT UPPER LEFT)
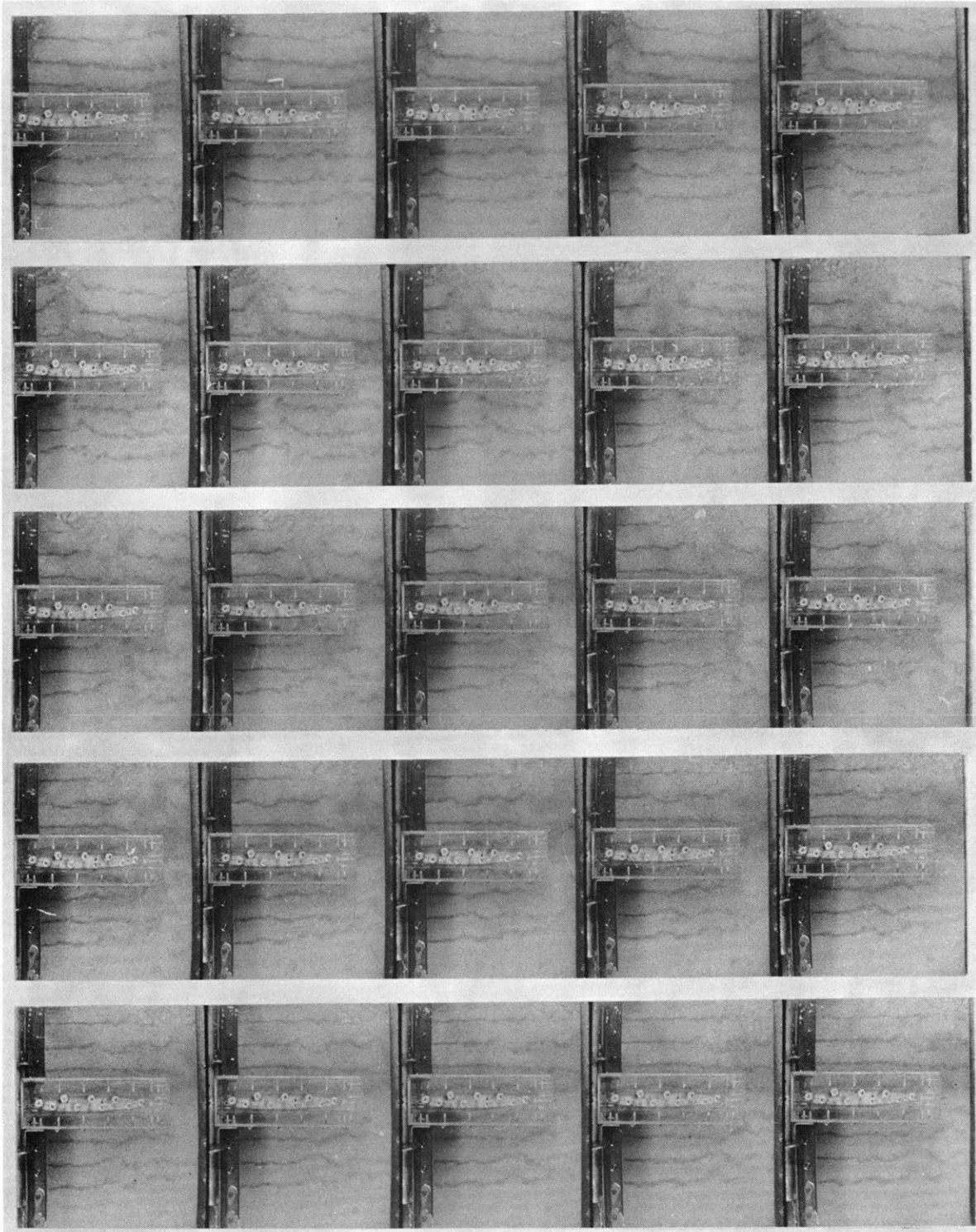
FIGURE 23b. SEQUENCE SHOWING WAKE GENERATED BY NO. 1 CYLINDER
PASSING OVER AIRFOIL. FREE STREAM VELOCITY = 2.77 ft/sec.
RELATIVE CYLINDER VELOCITY = 6.83 ft/sec. (SEQUENCE BEGINS
AT UPPER LEFT.)
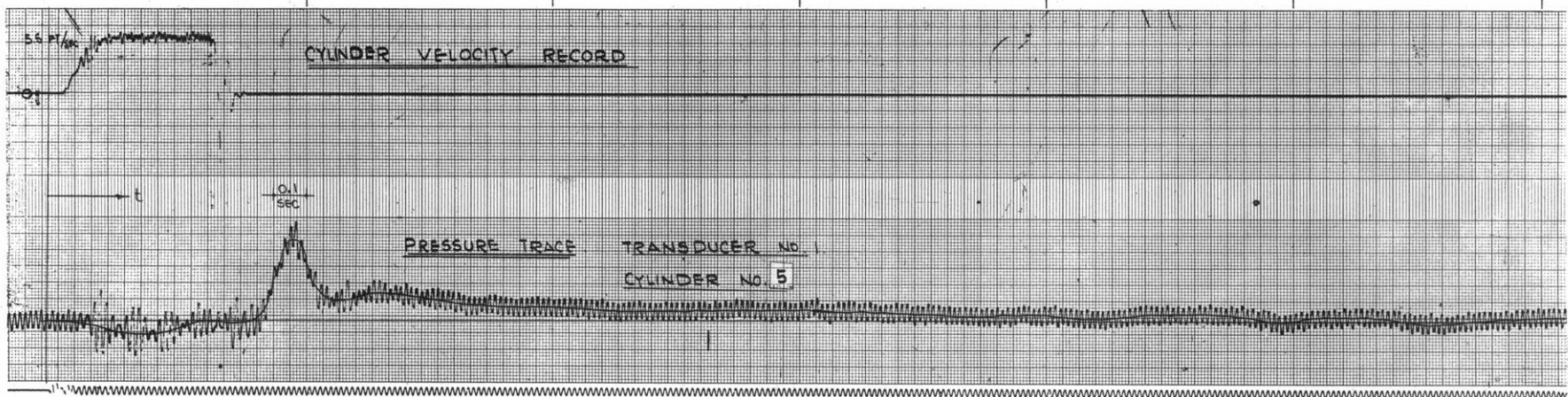
FIGURE 24. TYPICAL PRESSURE RECORD
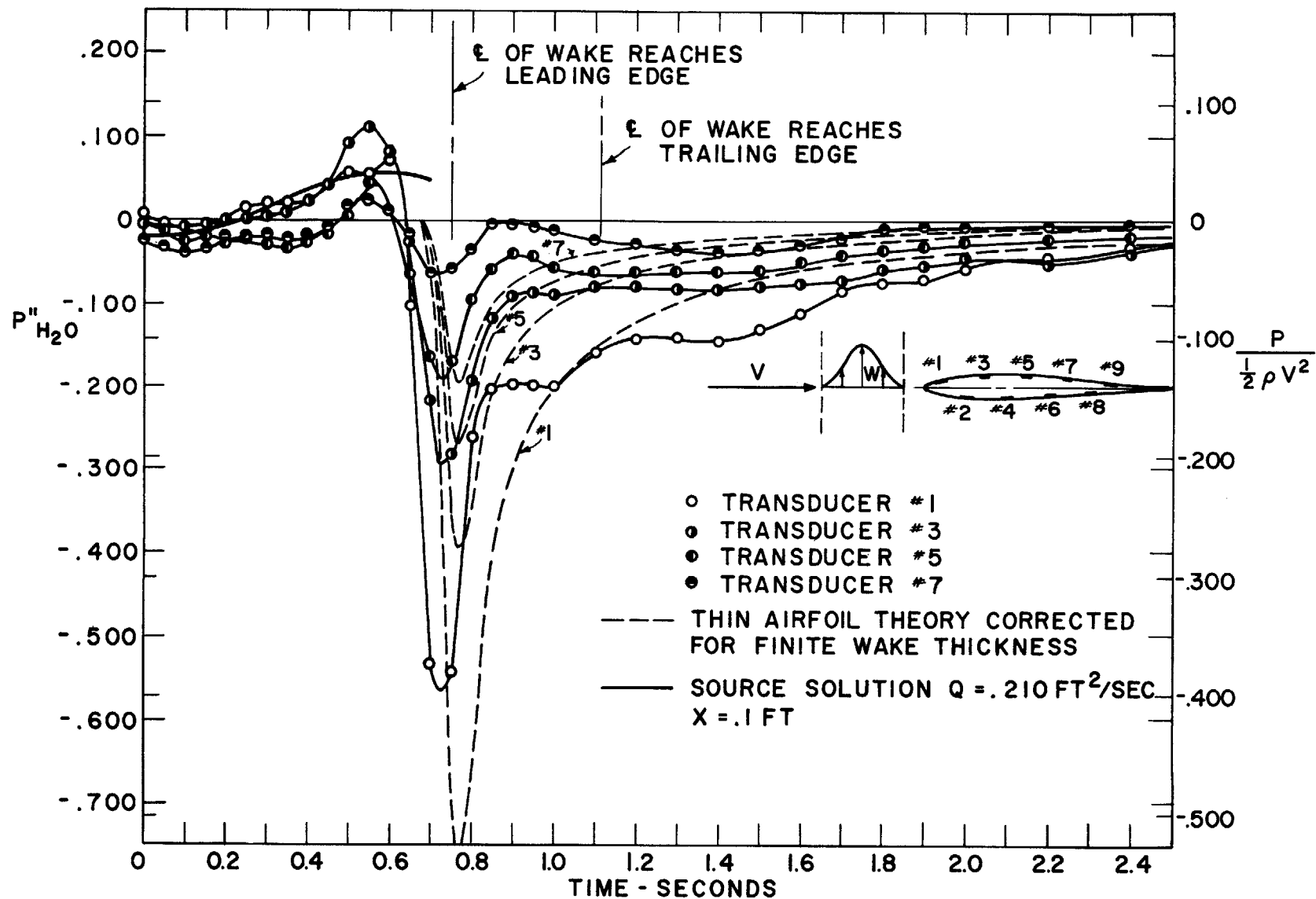
FIG. 25a PRESSURE TRACES FOR #1 CYLINDER $\overline{W}$=0.210 FT/SEC (SUCTION SIDE)
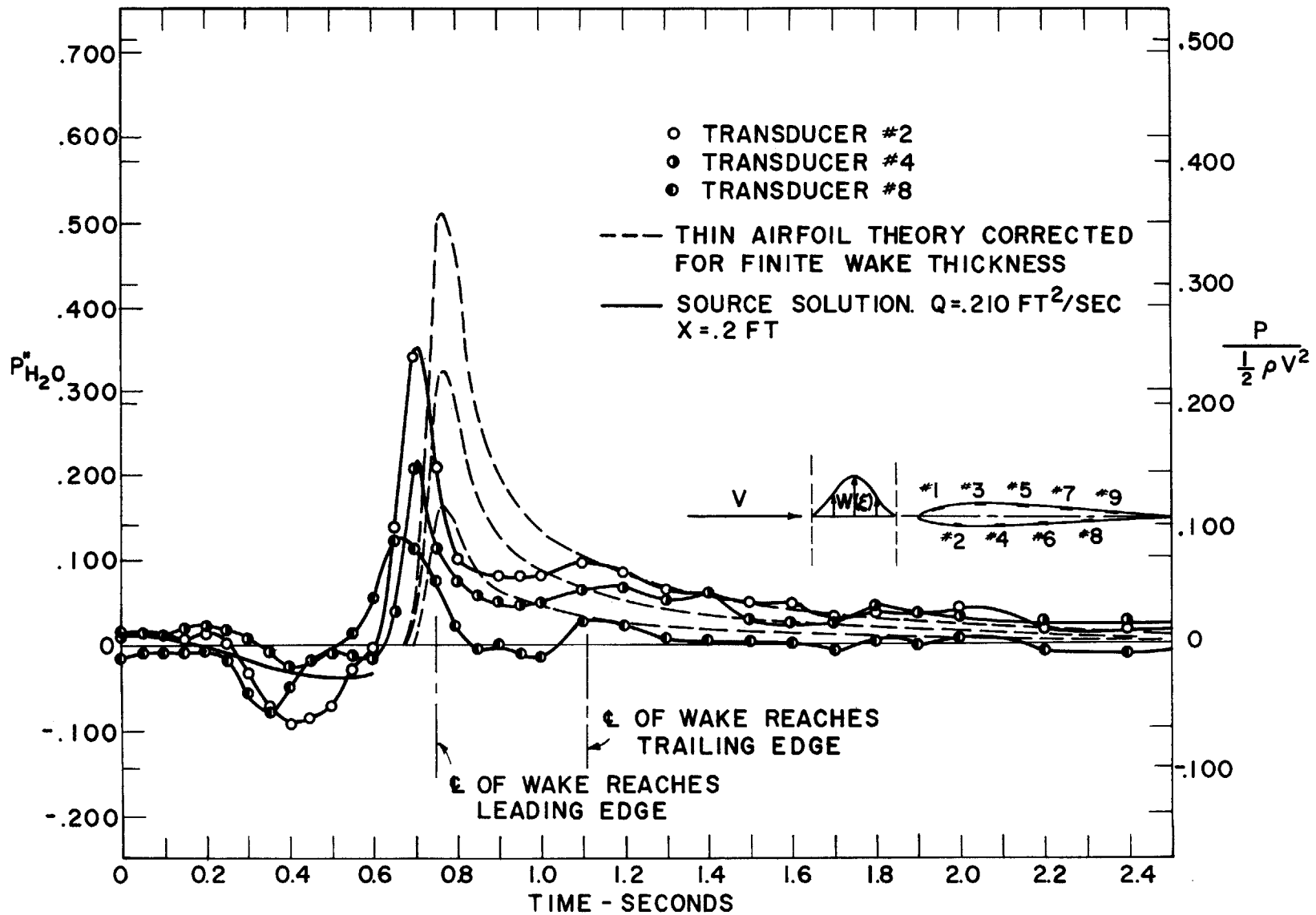
FIG. 25b PRESSURE TRACES FOR #1 CYLINDER $\overline{W}$=0.210 FT/SEC (PRESSURE SIDE)
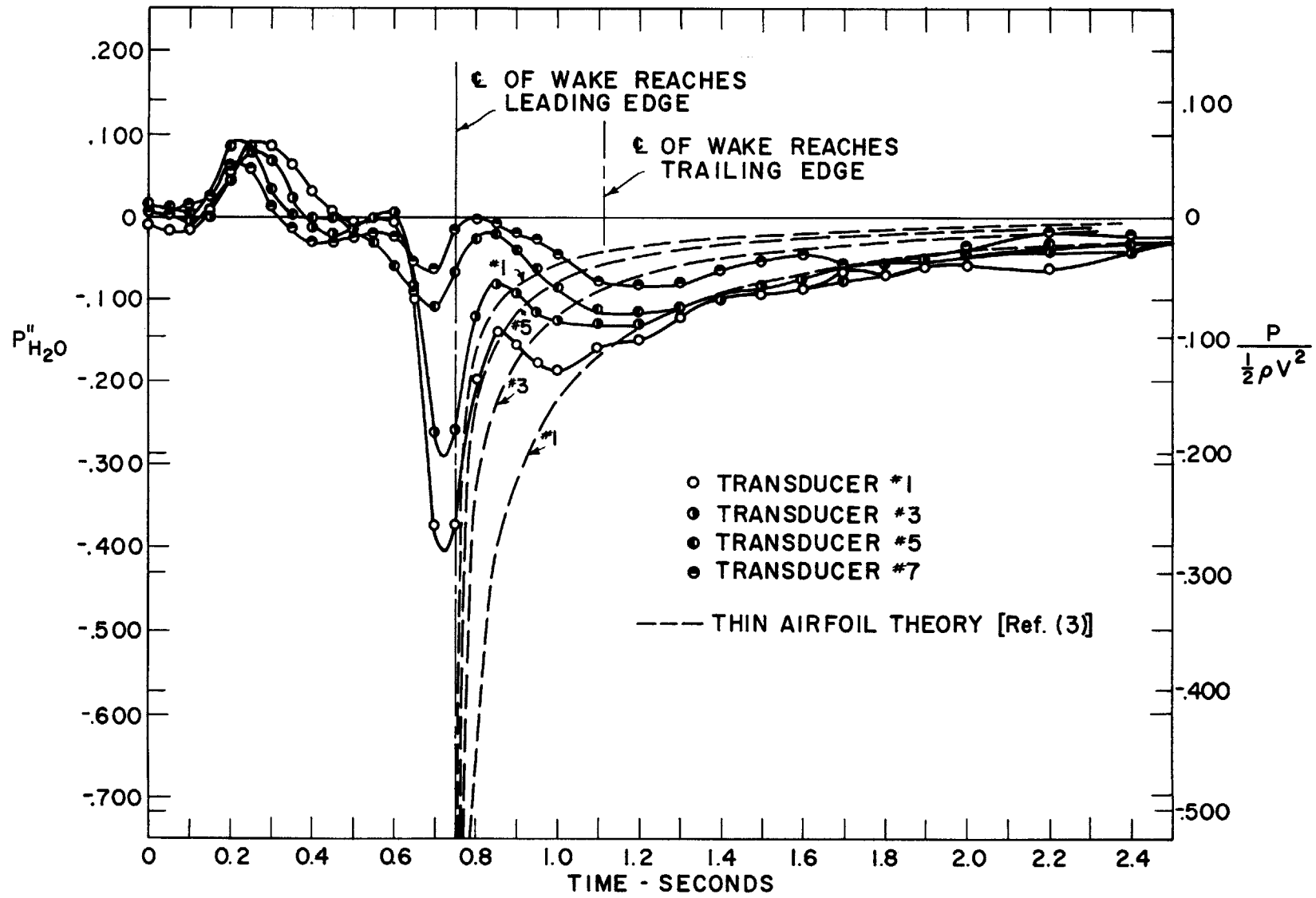
FIG. 26a   PRESSURE TRACES FOR #5 CYLINDER $\overline{W} = 0.235$ FT/SEC (SUCTION SIDE)
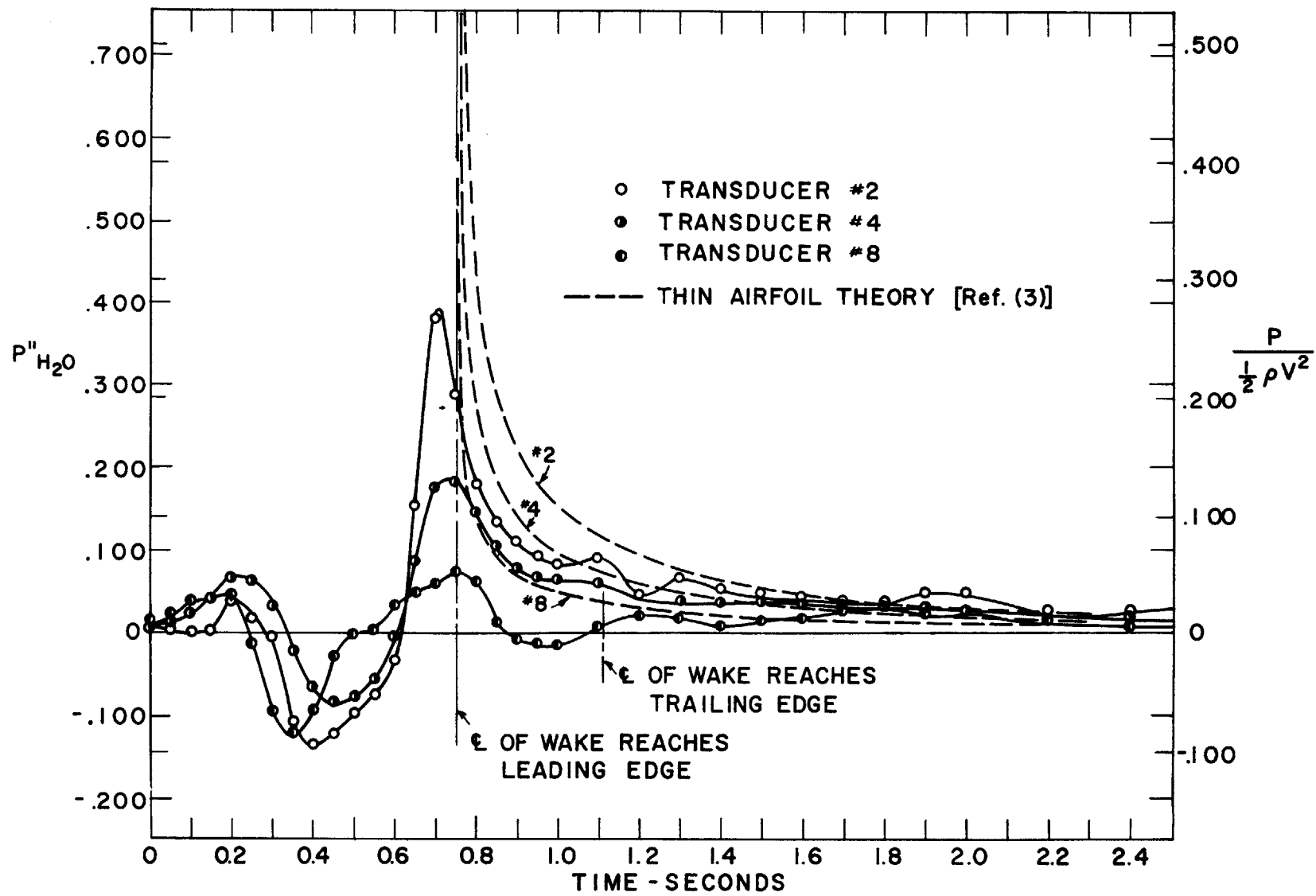
FIG. 26 b PRESSURE TRACES FOR #5 CYLINDER. $\overline{W}$ =0.235 FT/SEC (PRESSURE SIDE)
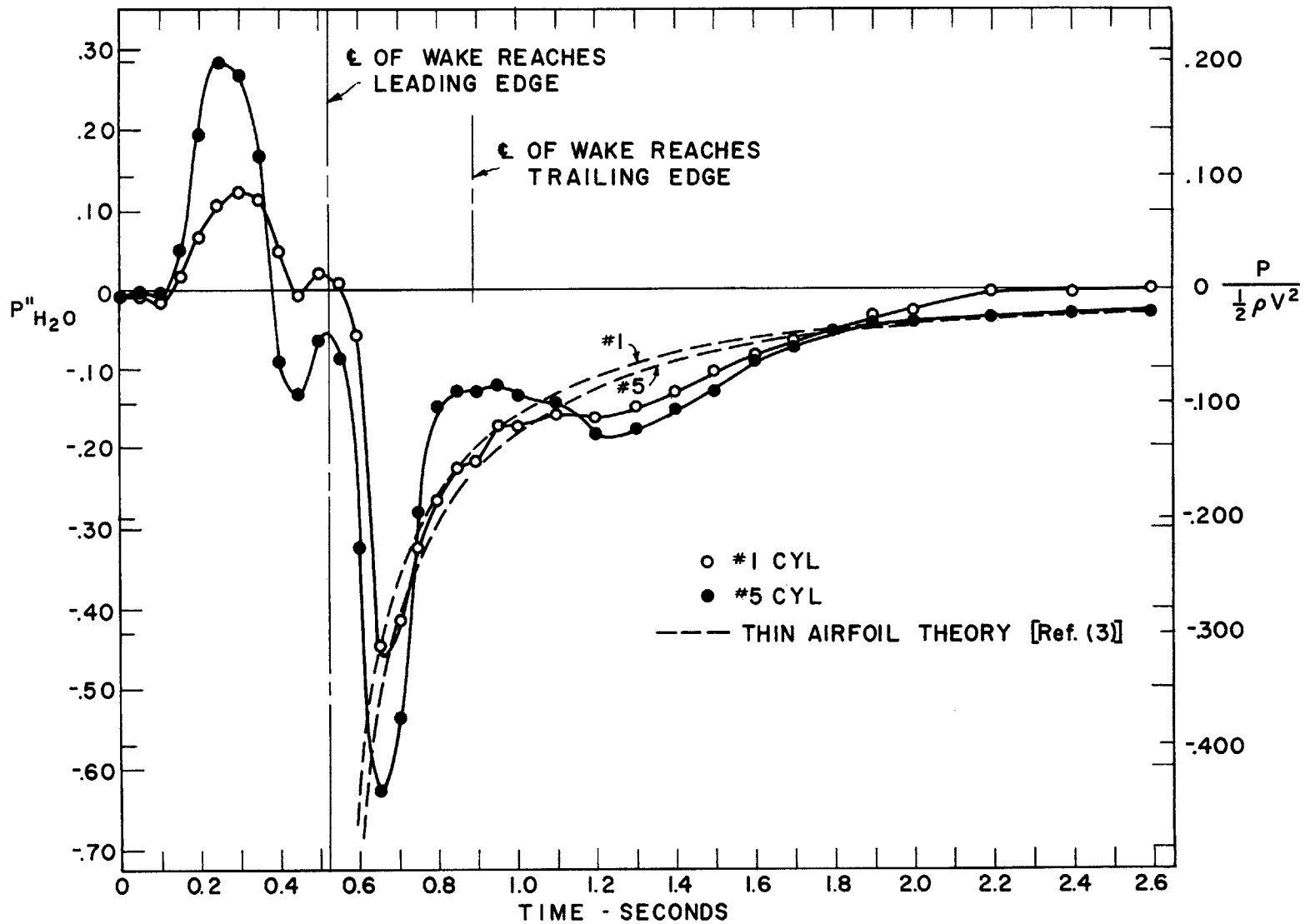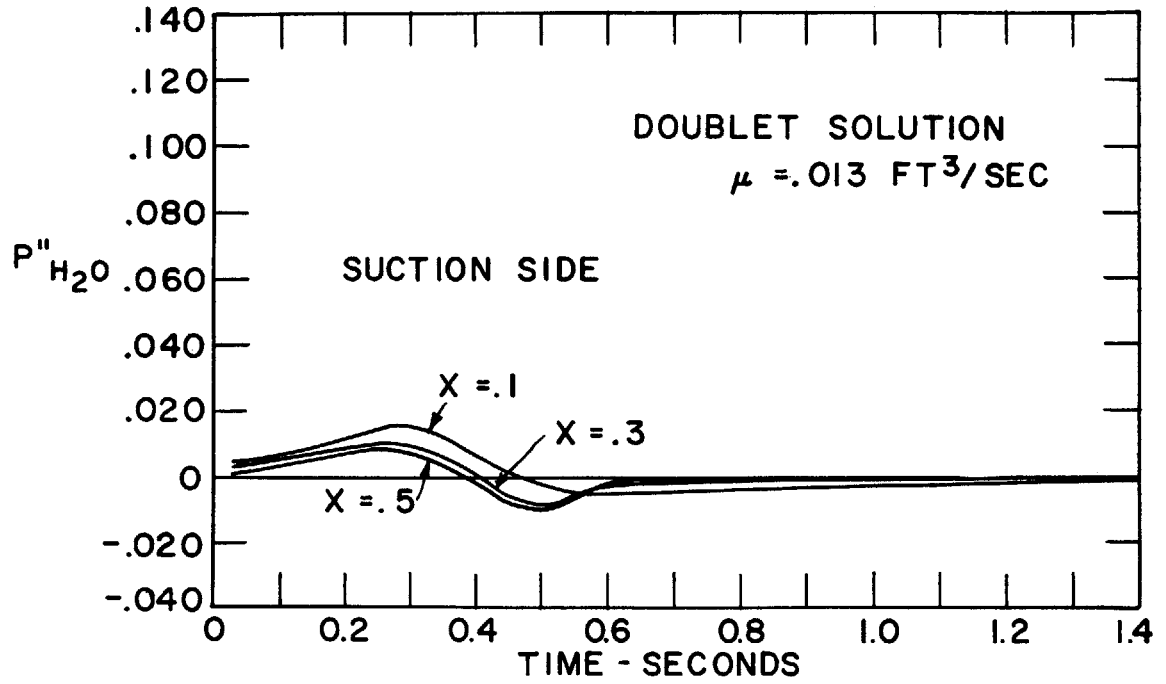
FIG. 27a CYLINDES ALL OUT PRESSURE TRACES TRANSDUCER #1
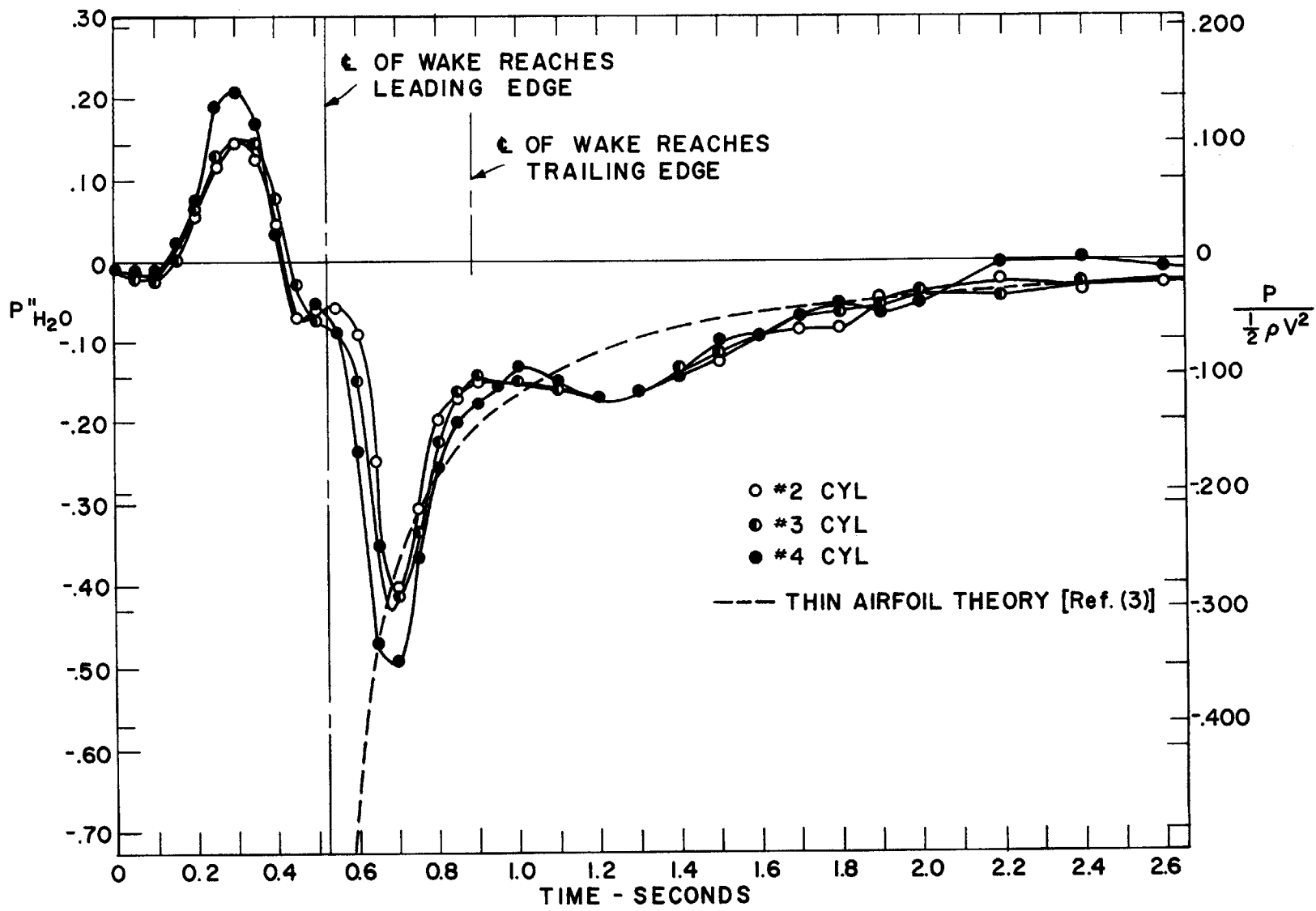
FIG. 27b CYLINDERS ALL OUT. PRESSURE TRACES TRANSDUCER #1
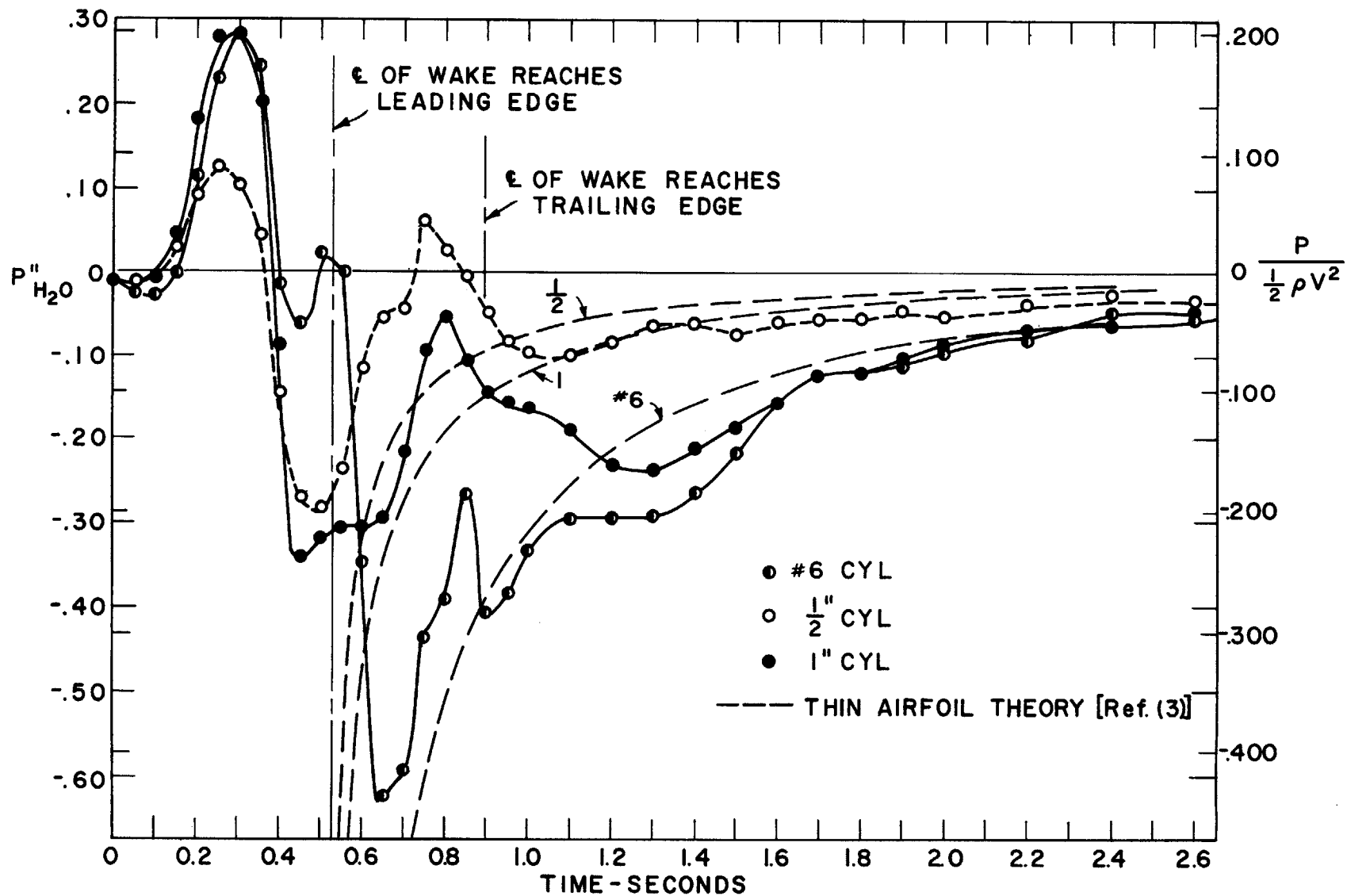
FIG. 27c CYLINDERS ALL OUT. PRESSURE TRACES TRANSDUCER #1
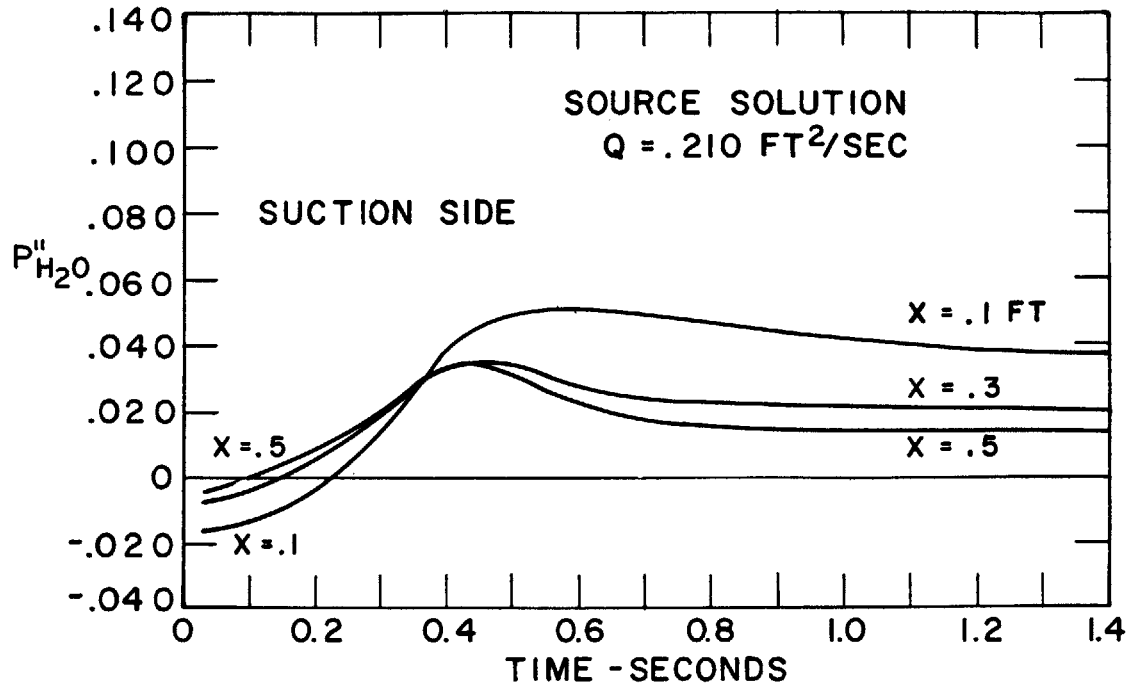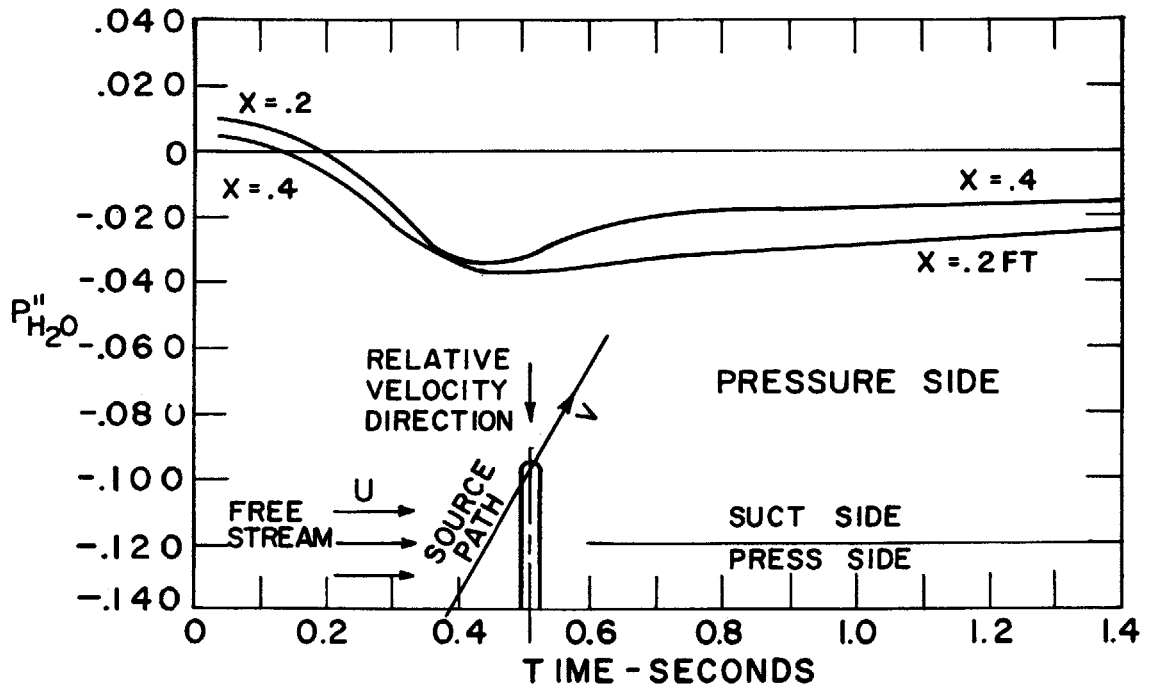
FIG. 28
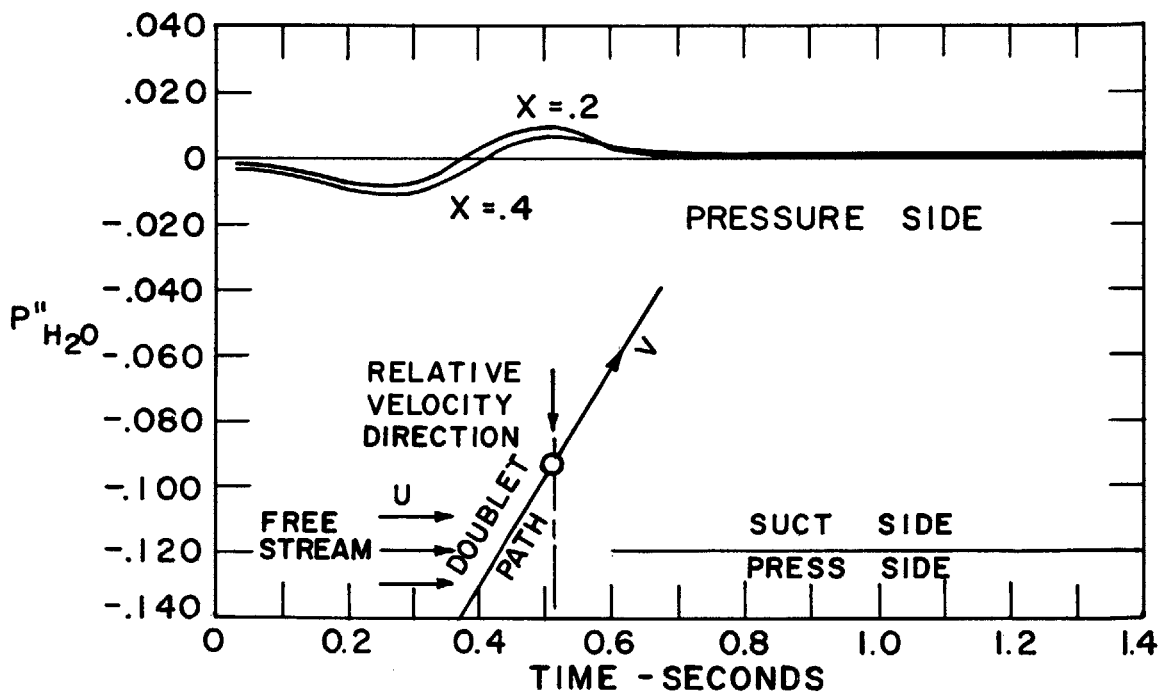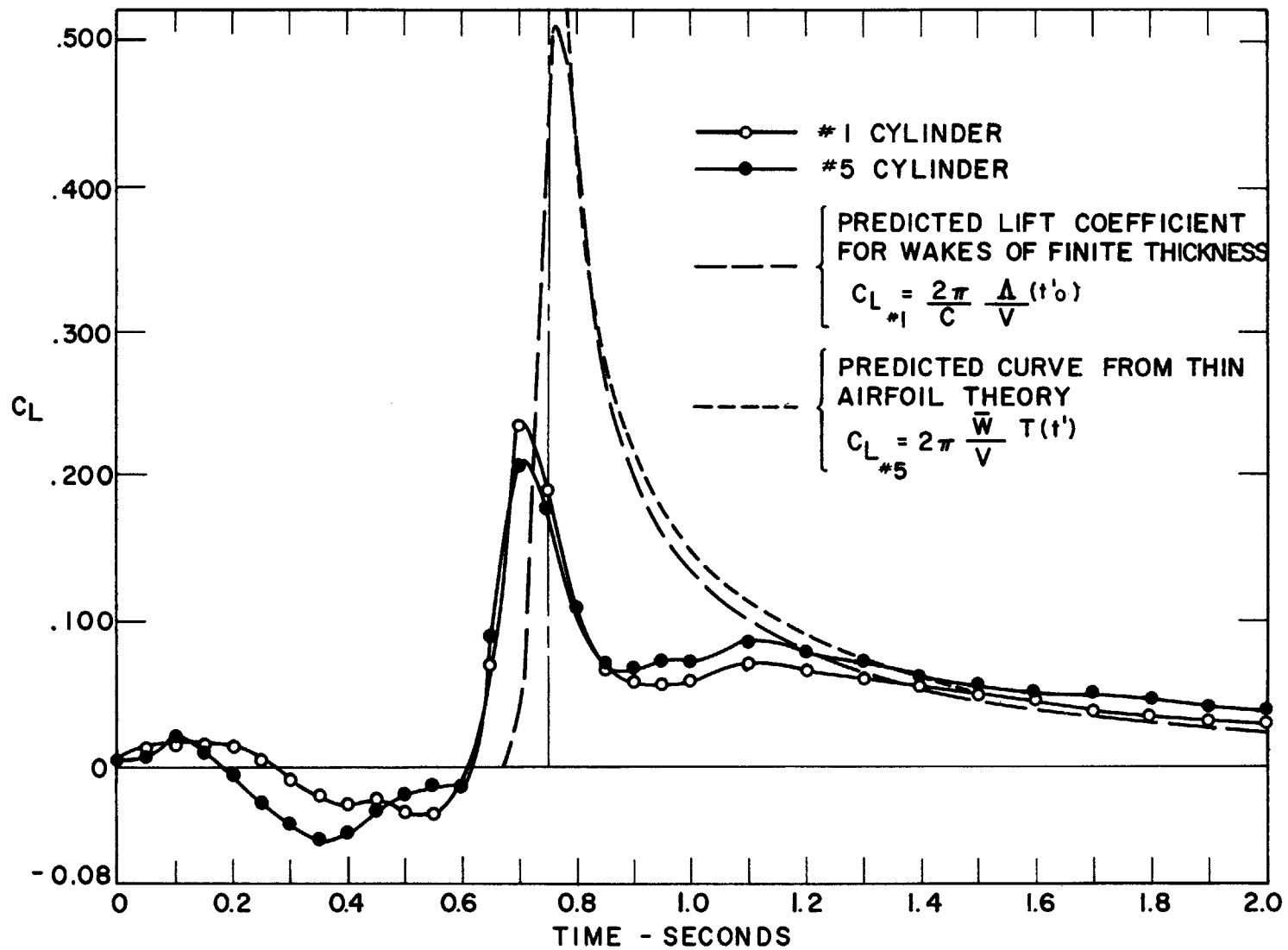
FIG. 29

FIG. 30 UNSTEADY FORCE LIFT COEFFICIENT VS TIME

$$C_W = \frac{L}{\rho V \overline{W} C}$$

#1 CYLINDER
#5 CYLINDER

TIME - SECONDS

FIG. 31 C_W VS TIME